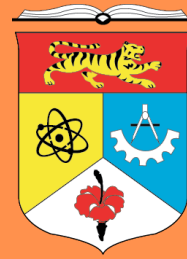


PROSIDING PENYELIDIKAN PRA SISWAZAH



UNIVERSITI
KEBANGSAAN
MALAYSIA
*The National University
of Malaysia*

Vol. 1, 2021

Undergraduate Research Project
Symposium, Dept. of Electrical,
Electronic and Systems

EDITOR:
Asma' Abu-Samah

Contents

Plant Disease Detection and Classification Using Camera and Convolutional Neural Network <i>Charis Teoh Yi En, Gan Kok Beng</i>	1
Optimize Neural Network Implementation on FPGA <i>Chia Tieng Tieng, Sawal Hamid Md Ali</i>	13
Colour Contrast Analyser for Colour Blind Assessment <i>Harhiviin a/l Ganesan, Kalaivani Chellapan</i>	20
Design of portable biosensor reader for Leptospira Detection <i>Kaliswaran a/l Ganesan, Noorfazila Kamal, Huda Abdullah</i>	28
The Development of Solar Charger Based on Sun Detector Using Arduino <i>Izzuan Ismail, Nor Azwan Mohamed Kamari</i>	40
High Performance Cuk Converter Controller <i>Muhammad Khairul Naim Saaey, Yushaizad Yusof, Radin Zaím Radin Umar</i>	47
Simulation of the Performance of Iron Pyrite Thin Film Solar Cell by SCAPS 1-D <i>Nik Khaliq Zailani Nik Iskandar, Badariah Bais, Puvaneswaran a/l Chelvanathan</i>	57
Stroke Monitoring System using The Microwave Imaging System <i>Nurrol Athirah Mohamad, Norbahiah Misran, Mohammad Shahidul Islam, Mohammad Tariqul Islam</i>	63
Underwater Data Logger Development: Bluetooth Wireless Communication Implementation for Monitoring <i>Nurul Izzati Saleh, Iskandar Yahya</i>	72
Design Optimization of Fuzzy-PID Controller for Path Tracking of an Autonomous Hovercraft <i>Nur Amaliea Izzatie Azmi, Asma Abu-Samah, Aqilah Baseri Huddin</i>	82

Index of Authors

Plant Disease Detection and Classification Using Camera and Convolutional Neural Network

(Pengesanan Dan Pengelasan Penyakit Tanaman Menggunakan Kamera Dan Jaringan Saraf Konvolusional)

Charis Teoh Yi En, Gan Kok Beng

Department of Electrical, Electronic and Systems Engineering,

Faculty of Engineering & Built Environment, Universiti Kebangsaan Malaysia, Malaysia

*Corresponding author: A165100@siswa.ukm.edu.my

ABSTRACT

Based on the data from the Food and Agricultural Organization (FAO), around 1.3 billion tonnes of plants are infected by plant disease. In the past, farmers use eye observation to detect and classify plant disease. However, due to the advanced technology nowadays, plant disease can be easily detected and classified by using image processing. Many researchers are concerned about deep learning technology which is used in image processing to detect and classify plant disease. Plant disease classification is difficult due to the large differences in size, shape, colour, layout, lighting and imaging illumination of plant diseases. CNN is a deep learning neural network designed for processing structured arrays of data such as images. Due to the strong feature extraction capability of convolutional neural networks (CNN), CNN is widely used in computer vision and image recognition among various network architectures used in deep learning. A convolutional neural network contains many convolutional layers stacked on top of each other, each one is capable to recognize more features. In this work, the CNN is able to recognize plant disease accurately with five convolutional layers. The main objective of this study is to develop a deployable model for plant disease classification using web application and desktop application with camera to form a real-time inference vision system. In this work, a CNN model was trained with a public dataset that consists of 19384 potato, pepper and tomato images collected under controlled condition. The selection of the images were due to the facts that they are the most common plants in Malaysia. Different parameters such as epochs, batch size, dropout are used to evaluate the performance of the model. A classification report and confusion matrix were used to evaluate its sensitivity and specificity. The developed desktop and web application was able to recognize three different plant diseases and 15 different categorical disease classes as well as healthy plant leaves. Based on the classification report, the trained model can achieve an accuracy of 97.2% and average F1-score of 97%. In conclusion, the trained CNN model can detect and classify plant disease accurately and can produce a useful information for farmers to apply pesticide more effectively to cure plant disease and benefit the agricultural sector.

Keywords: CNN, Plant Disease Classification, Image processing, Computer Vision, Web Application, Desktop Application, Deep Learning

ABSTRAK

Berdasarkan data dari Organisasi Makanan dan Pertanian (FAO), sekitar 1.3 bilion tan tanaman dijangkiti penyakit tanaman. Pada masa yang lalu, petani menggunakan pemerhatian mata untuk mengesan dan mengelaskan penyakit tanaman. Namun begitu, disebabkan teknologi yang canggih sekarang ini, penyakit tanaman dapat diklasifikasi dengan mudah melalui pemprosesan imej. Ramai penyelidik prihatin terhadap teknologi pembelajaran mendalam yang digunakan dalam pemprosesan imej untuk mengklasifikasi penyakit tanaman. Pengklasifikasi penyakit tanaman sukar dilakukan disebabkan perbezaan besar dalam ukuran, bentuk, warna, susun atur, pencahayaan dan pencahayaan pencitraan penyakit tanaman. CNN adalah rangkaian neural pembelajaran mendalam yang direka untuk memproses susunan data tersusun seperti gambar. Disebabkan oleh kemampuan rangkaian neural konvolusi (CNN), CNN banyak digunakan dalam visi komputer dan klasifikasi imej dalam di antara pelbagai seni bina rangkaian yang digunakan dalam pembelajaran mendalam. Jaringan neural konvolusi mengandungi banyak lapisan konvolusi yang saling bertumpuk, masing-masing mampu mengenali lebih banyak ciri. Dalam kajian ini, CNN dapat mengklasifikasi penyakit tanaman dengan tepat dengan adanya lima lapisan konvolusional. Objektif utama kajian ini adalah untuk membangunkan model yang boleh digunakan

di aplikasi web dan aplikasi desktop dengan kamera untuk mengklasifikasi penyakit tanaman supaya dapat membentuk sistem visi inferensi waktu nyata. Dalam kajian ini, model CNN dilatih dengan set data umum yang terdiri daripada 19384 gambar-gambar kentang, lada dan tomato dalam keadaan terkawal. Pemilihan gambar-gambar adalah disebabkan mereka adalah tanaman-tanaman yang paling biasa di Malaysia. Parameter yang berbeza seperti repetisi, saiz kumpulan. Keciciran adalah digunakan untuk menilai prestasi model. Laporan klasifikasi dan matriks kekeliruan digunakan untuk menilai kepekaan dan kekhususannya. Aplikasi desktop dan web yang dibangunkan dapat mengklasifikasi tiga jenis penyakit tanaman yang berbeza dan 15 kelas penyakit kategori yang berbeza serta daun tumbuh-tumbuhan yang sihat. Berdasarkan laporan klasifikasi, model yang terlatih dapat mencapai ketepatan 97.2% dan purata skor F1 97%. Kesimpulannya, model CNN yang terlatih dapat mengklasifikasi penyakit tanaman dengan tepat dan dapat menghasilkan maklumat yang berguna bagi petani untuk menggunakan racun perosak dengan lebih berkesan untuk menyembuhkan penyakit tanaman dan memanfaatkan sektor pertanian.

Kata Kunci: CNN, Pengesanan Penyakit Tanaman, Pemprosesan Imej, Visi Komputer, Aplikasi Web, Aplikasi Desktop, Pembelajaran Mendalam

INTRODUCTION

According to a report by UC Agriculture and Natural Resource Scientist, loss of crops increased from 10 percent to 40 percent due to plant disease. In developing countries, smallholder farmers generate more than 80% of the agricultural production. Therefore, the loss of crops have terrible consequences to them. Due to the sudden climate change, farmers lose almost all of the crops due to pests and plant diseases mostly caused by harmful viruses and bacteria. Plant diseases can damage crops, thus reducing the availability and access to food, increasing the cost of food. Advances in Computer Vision shows an opportunity to increase the usage of artificial intelligence in computer vision applications in agriculture sector (Bhise 2020). Early detection of plant disease can cure the plant disease more efficiently, thus increasing the crop production. Plant disease classification is difficult due to the unwell defined boundaries of the symptoms on the leaf. The analysis of plant disease images might be difficult due to the bad quality images which are affected by lighting, resolution, weather and more. Furthermore, different plant diseases might have similar symptoms. Therefore, it is very important to develop a model that can overcome some of the challenges and is able to detect and classify the plant diseases accurately.

CNN is specifically applied for Computer Vision applications that involves image detection and classification among various network architectures used in deep learning. The challenges for CNN to detect and classify plant disease is to create a deep network such that nodes, structure of the network and edge weights map the input (the image of a diseased plant) to the output (crop-disease pair) correctly. Object classification is mainly used by deep convolutional neural networks (DCNN) and their variations. DCNN has 5 types, which includes R-CNN, fast R-CNN, GoogleNet, VGGNet and Resnet. DCNN is built upon stacked convolutional neural networks (CNNs) which is a variant of feed-forward network (FFN).

Many research papers have been reviewed based on the general flow of the plant disease classification systems (Santhosh 2019) which consists of image acquisition, image pre-processing, image segmentation, feature extraction and image classification. The plant diseases are classified by extracting the features of plant images (Gajanan 2018) and classifying these features (Dhingra 2017).

According to Yang (2020), many efforts focused on deep learning, in which it is known as DCNN. However, the author stated that the CNN is good enough for image processing and is able to extract enough information. Author has proposed that the combination of shallow CNN and classic machine learning classification algorithm to detect and classify plant disease performs better with fewer parameters than other deep models in terms of precision, recall and F1-score. Srivastava (2021) has also conducted a research to detect and classify plant disease with CNN and has accuracy of 88%. Toda (2019) used CNN by applying a variety of neuron-wise and layer-wise visualization methods to detect and classify plant disease. Number of parameters decreased by 75% due to the removal of many layers that are not necessary. Sladojevic (2016) used deep CNN approach to detect and classify plant disease by using classification method and achieved an average accuracy of 96.3%.

According to Gogul (2017), the main difference between ANN and CNN is that only the last layer of a CNN is fully connected, but each neuron is connected to every other neurons in ANN. The neurons in a CNN layer are not connected to all other neurons, but only connected to a small region of neurons in the previous layer, as compared to ANN. CNN is most useful in image classification due to the unique technique of extracting from lower level features to higher level features in an image. The size of the images will cause ANN to over-fit easily. Larger images will need more powerful processor to process due to complex vector. To compare the performance of three different machine learning method, CNN, ANN and SVM have accuracy of 99%, 94% and 91% respectively during

image classification of vegetation species (Mehmood ul Hasan 2019).

An insufficient number of sample leaf images will lead to overfitting. Therefore, Arsenovic (2019) has conducted a study to use traditional augmentation methods and GAN to increase the dataset size. The trained model has 93.67% accuracy. Future work should be focused on detect and classifying different phase of plant disease in different locations. Author has also applied augmented process which includes transformation, rotations and more to increase dataset. The CNN model trained by Harte (2020) uses augmentation and transfer learning. The trained CNN model has an accuracy of 97.2% and F1 score of more than 96.5% and it is deployed as web application. Rishiikeshwer (2019) has trained a CNN model of 98% accuracy with 3600 augmented datasets but 95% accuracy with 400 leaf images.

Many deep learning models perform badly once the model is tested on independent data. Therefore, various studies on how segmented images can improve accuracy of the model are conducted. Chowdhury (2021) and Paul Sharma (2020) conducted the study to solve the problem by using segmented image data to train the CNN models. Sharma (2020) demonstrated that the S-CNN model trained using segmented images has accuracy of 98.6% when tested on independent data as compared to the F-CNN model that is trained using full images. Chowdhury (2021) shows accuracy, IoU and Dice score of 98.66%, 98.5%, and 98.73% for the modified U-net segmentation model. The six-class classification and binary classification of EfficientNet-B7 has achieved an accuracy of 99.12% and 99.95% respectively. Finally, EfficientNet-B4 that uses segmented images for ten-class classification achieved an accuracy of 99.89%. This work can improve the applicability of real-time monitoring in classification of plant disease. However, the limitation in this research is that the model is very sensitive to the quality of segmentation of images. Hassan (2021) has used InceptionV3, MobileNetV2, InceptionResnetV2 and EfficientNetB0 to detect and classify plant disease. By splitting the dataset into 80-20, which is 80% train images and 20% test images, the computation cost and number of parameters have reduced. EfficientNetB0 model has 99.6% accuracy. 565 and 545 s/ epoch were needed to train the images in the MobileNetV2 and EfficientNetB0 architectures respectively on coloured images. Thus, MobileNetV2 can be easily run on mobile devices due to the parameter number and operations that have been limited.

In CNN, the flow of information has no feedback from the output layer to the previous layers. Normal CNN has two or three layers but DCNN has more than 5 hidden layers. Therefore, DCNN can extract more features and its

implementation is better in terms of higher accuracy. CNN has input, hidden, and output layers. The hidden layers in CNN consist of pooling layers, convolutional layers and fully connected layers.

Convolutional layers in CNN are sets of image filters convoluted to pooling layer and feature maps or images. Feature maps are extracted through convolution and other processing layers repetitively in image classification (P.M. Jacob 2020). A label is then outputted by the network which indicates an estimated class. Features in train dataset that can solve the classification problem is generated by the optimization of weights and filter parameters by CNN in the hidden layer so that the time taken to achieve best learning in CNN can be lowered. Gradient descent and back-propagation approaches can optimize the parameters in the network by updating the weights in each image in the training set repetitively to minimize the classification error (Sagar 2020). Different models of neural networks may overfit differently, thus dropout layer is needed to reduce overfitting.

Various papers also presented mobile phone application and web application to detect and classify plant disease by using the trained model. Petrellis (2017) has developed a mobile phone application to monitor plant disease and has achieved accuracy of more than 90%. Rishiikeshwer (2019) has trained a CNN model to be deployed on IoT Web Application that is developed to capture, process and show the predicted plant disease name. A CNN model that has been trained by Ramcharan (2019) is deployed in a mobile app. F1-score is used to evaluate its performance on mobile images. Recall of the model decreases. Therefore, the performance of F1-score decreased by 32% for real world images and video. It is very important to provide enough images to train the CNN model so that the model can be used in real world applications.

There is a limited study to deploy the CNN model with real world applications for plant disease classification. Therefore, this work aims to develop a real-time inference vision system that can detect and classify plant disease accurately with web application, desktop application and Pixy2 camera. The plant diseases can be identified at early stage by using various image processing techniques. The CNN plant disease classification model was trained using OpenCV, python and 20638 healthy and diseased potato, pepper and tomato images. The model was able to detect and classify plant disease through the various coloured spots and patterns on the leaf of the affected plant. The integration of developed model with a camera formed a real-time inference vision system to help the amateurs and trained professionals to verify the diagnosis of plant disease.

METHODOLOGY

The Sequential model was used in this work. An application-based software integrated with Pixy2 camera to form a real-time inference of vision system is proposed. Various libraries like Tensor flow, numpy, matplotlib, os, sklearn, pandas, cv2, seaborn and more were imported. The Sequential model is built in python by using Tensor flow version 2.3.0 and Keras frameworks. The Sequential model behaves like a Functional API model, in which every layer has an input and output attribute to extract the outputs of all intermediate layers in a Sequential model. A CNN model is trained to detect and classify plant disease. Figure 1 shows the plant disease classification system overview using deep learning. The real inference vision system consists of two main parts, in which it consists of training and testing of the model and the real time inference vision system. The real time inference vision system consists of two main parts which is Pixy2 camera and web and desktop applications with CNN model to detect and classify plant disease.

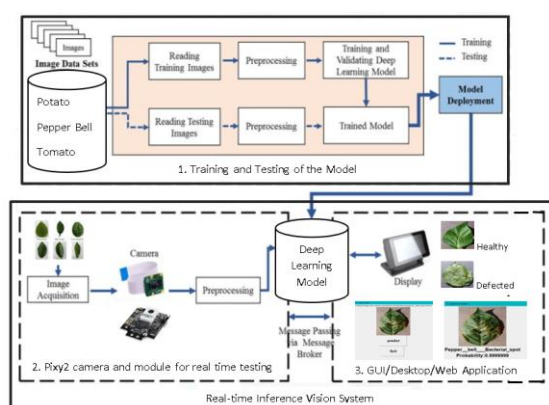


FIGURE 1. System overview

Dataset and model architecture

A publicly available dataset which consist of 20638 images of healthy and diseased potato, pepper and tomato images collected under controlled condition was downloaded from Kaggle. The training and test directories were created from the dataset. Since the model has been decided to be sequential model, validation set was not needed. The train dataset has 19384 images, and the test dataset has 1254 images belonging to 15 different categorical classes. The number of images available in each class of plant disease in the train set was quite balance as shown in Figure 3.



FIGURE 2. Sample images of plant disease

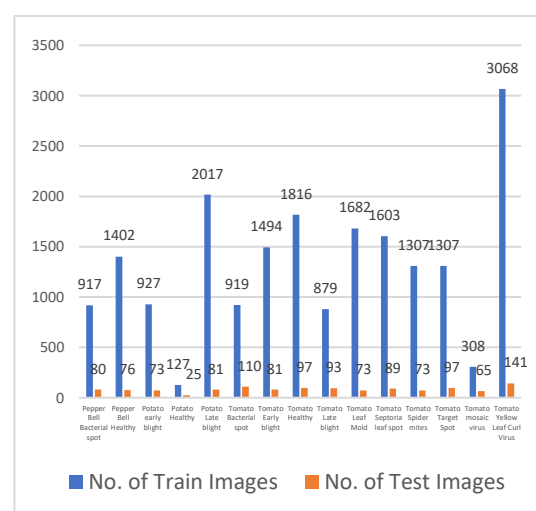


FIGURE 3. Number of train and test plant disease images

K-Fold cross validation was used in this model to split dataset. In 10-Fold cross validation, the data was divided into 10 subsets and was split randomly into 90-10, in which 10 partitions of data of same size was created randomly. 9 of them was used for training and 1 for testing at 10 instances of learning. During testing, every partition was used only once. To overcome the challenges of GPU memory boundaries and still use larger batch sizes which is 64 in this work, each of the images were resized to 48 X 48 and segmented for preprocessing. Augmentation process was applied to increase the dataset to reduce overfitting and to balance the distribution of the images. With the equal distribution of images in each class, it was possible to use all the data instead of choosing data randomly during training. The training accuracy will therefore be increased. Thus, random yet realistic transformations such as random horizontal flipping was applied to the training images to artificially introduce sample diversity. While slowing down overfitting, the model will also be exposed to different aspects of the training data. It was important to develop models that take raw data as

input, instead of models that take already preprocessed data. If the model expects preprocessed data, when the model is exported to be used in a web application or mobile application, the exact same preprocessing pipeline will need to be implemented. Therefore, it was necessary to do least possible amount of preprocessing before inputting the images into the model.

The preprocessed image was taken and converted into reduced variables. Figure 4 showed the architecture of CNN model used in this work. The top layer was trained and fine-tuning of the entire model was done.

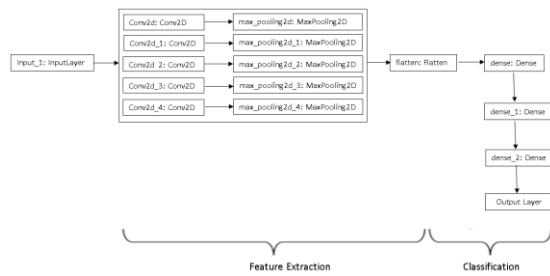


FIGURE 4. Block diagram of CNN model architecture

This CNN model has input, hidden, and output layers. The hidden layers in CNN consist of

convolutional layers, pooling layers and dense layers. The first five layers in the model were Conv2D layers. These 2D convolutional layers dealt with input images. There were 64 filters in the first layer, 128 filters in the second layer, 256 filters in the third layer, 512 filters in the fourth and fifth layer. Every layer of filters were there to capture patterns. The first layer of filters captured patterns like dots, edges, corners and more. The patterns became bigger as those patterns were combined by the subsequent layers. For example, edges were combined to make circles, squares and more. As the layers increased, the patterns will get more complex. Therefore, the filter size in subsequent layers was increased to capture as many combinations as possible. The amount of pixels added to an image when it was being processed by the kernel of a CNN is the same. The convolutional layer was then passed to Max pooling to help extract low-level features like edges, points and more for better accuracy. In this pooling operation, the maximum element was chosen from the region of the feature map covered by the filter. After max-pooling layer, feature map which contained the best features of the previous feature map was the output. Each convolutional layers were added with the ReLU activation function (Rectified Linear Unit) because CNN with ReLUs trained much more quickly and reliably, thus models can learn faster and perform better. The images were passed through the layers more than once for better feature extraction.

TABLE 1. Parameters used to train CNN model

Parameters	Value
Training epoch	25
Batch size	64
Dropout	0.25
Learning rate	0.005

Based on Table 1, the training epoch was set to be 25 to train the model. The entire train dataset will pass the algorithm 25 times. More epochs increased the accuracy and decreased the loss. Thus, the plant disease classification model can predict plant disease more accurately. The model was only run once. These unique features were then sent for further processes. In this model, batch normalization layers were used to track the mean and variance of the inputs. Batch size was set to be 64. Big batch size can speed up the training and has even better generalized performances. The required GPU memory will increase when the batch size increases. A dropout layer was added before the classification layer for regularization to prevent a model from overfitting. On passing a dropout of 0.25, 25% of the nodes were dropped out randomly

from the neural network. During training, each update to a layer during training has a different “view” of the configured layer. With dropout, the accuracy will slowly increase and loss will slowly decrease. The model was compiled by using three parameters such as loss, optimizer and metrics. ‘Categorical cross entropy’ was used as the loss function. The lower score indicates that the model is performing better. Adam Optimizer with 0.05 learning rate was chosen because it was more efficient and used less time to train the neural network. Metric was used to evaluate the accuracy of the model.

Classification was a fully connected classifiers which were formed using various learnings done by the model. Three dense layers were used in this CNN model to detect and classify

the features. In dense layer, all outputs from the previous layer are fed to all its neurons so that the layer will be fully connected. The activation used was the 'Softmax' which gave a probability for each predicted class. The added classes will be added up to 1. The prediction was based on the class with highest probability. Images were flattened to convert the pooled images into single dimension vectors. The images were easier to be classified when the images were converted to the vectors. Certain classes had certain numerical values. Classification took place between two numerical arrays. Based on the dataset, if the numerical arrays matched, then the healthy or diseased leaf was classified. The model will detect and classify by showing the name of the plant disease and the confidence of the plant disease. The CNN model is saved and is deployed with web application and desktop application.

System integration and model deployment

Camera was used to capture leaf images. The leaf images were being uploaded to Google drive. Besides that, Pixy2 camera was connected to the PC to capture leaf images on the computer screen because we do not have real leaves. Then, the images were processed by model via web application and desktop application. Web application was developed by using HTML and CSS in Pycharm Community while desktop application was developed by using Tkinter. Since the images were taken from different camera, thus the images obtained have different qualities. The images were preprocessed to improve the image quality so that the accuracy of the system will not be affected. The developed desktop and web application is shown in Figure 5 and 6.

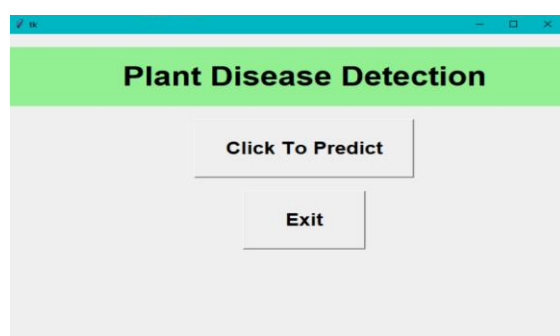


FIGURE 5. Desktop application

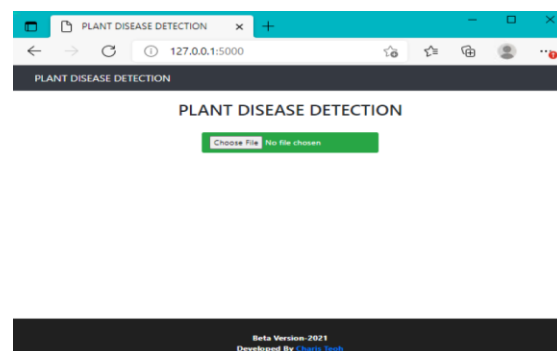


FIGURE 6. Web application

Evaluation metrics

To determine the performance of the trained CNN model, classification report and confusion matrix was shown. The training accuracy, test accuracy, training loss and test loss were shown. The graph of training accuracy and test accuracy versus epoch was plotted. The graph of training loss and test loss versus epoch was also plotted. This is to guide the fine-tuning process. Multi Class Log Loss evaluation was chosen to plot the two graphs.

$$L = -\frac{1}{N} \sum_i^N \sum_j^M y_{ij} * \ln(p_{ij}), \text{ where}$$

- N is the number of classes in the test data.
- M is the number of class labels which is 15 in this work.
- y_{ij} shows if the i-th object in the test data belongs to the j-th label which is given by a Boolean value.
- p_{ij} is the probability that the i-th object belongs to the j-th label.
- \ln is the natural logarithmic function.

A classification report and confusion matrix were used to evaluate its sensitivity and specificity. To predict the metrics of a classification report, the precision, recall and F1-score of the model were used.

Precision is the measure of accuracy in a classifier.

$$\text{Precision} = \frac{TP}{TP+FP}$$

Recall is the number of positive sample images that are classified correctly.

$$\text{Recall} = \frac{\text{TP}}{\text{TP} + \text{FN}}$$

In the F1-score, the best score is 1.0 and the worst is 0.0. It is a weighted harmonic mean of recall and precision. The weighted average of F1 is used to compare classifier models. Since F1-score takes both false positives and false negatives into their computation, it is lower but more useful than accuracy measures.

$$\text{F1-score} = \frac{2 * (\text{Recall} * \text{Precision})}{\text{Recall} + \text{Precision}}$$

RESULTS AND ANALYSIS

The training accuracy and test accuracy were very high, which is 97.2%, while the training loss was 8.5% and test loss was 11.9%. Overfitting has good performance in training data and poor generalization to test data, while under fitting has poor performance on training data and poor generalization to test data. It was seen that the model did not experience overfitting and under fitting because the performance of the training data and the test data were good. The classification report showed the

summary of prediction results on a classification problem and the number of test images in each class. The important predictive analytics such as precision, recall, accuracy, F1-score and support values were shown in Table 2 for 15 different categorical classes. The model performs the worst when 0 and the model performs the best when 1. F1-score is used for evaluation when both precision and recall are combined. F1-score takes both false positives and false negatives into account. F1-score is more useful than precision here. This is due to the fact that false negatives are a concern. For example, the leaf actually has tomato late blight but the model classified it as tomato healthy. This is false negative. It is very important to classify the healthy and unhealthy plant disease correctly so that the plant disease can be cured efficiently. Therefore, the model performs better when F1-score is higher. Precision states whether the model is suitable to detect and classify plant disease, while calculating recall shows its weakness. To detect and classify plant disease accurately, false negatives should be avoided because they will cause bad consequences. Therefore, recall is a better measure than precision. This shows that the model can perform well with 0.97 for both average accuracy and weighted class accuracy.

TABLE 2. Classification report

	Precision	Recall	F1-Score	Support
Pepper bell bacterial spot	1.00	0.94	0.97	80
Pepper bell healthy	0.97	0.93	0.95	76
Potato early blight	1.00	0.97	0.99	73
Potato late blight	0.95	1.00	0.98	81
Potato healthy	0.96	0.88	0.92	25
Tomato bacterial spot	1.00	0.98	0.99	110
Tomato early blight	0.96	0.90	0.93	81
Tomato late blight	1.00	0.98	0.99	93
Tomato leaf mold	1.00	0.99	0.99	73
Tomato septoria leaf spot	0.92	1.00	0.96	89
Tomato spider mites	0.94	1.00	0.97	73
Tomato target spot	0.90	0.95	0.92	97
Tomato yellow leaf curl virus	0.99	1.00	1.00	141
Tomato mosaic virus	1.00	0.98	0.99	65
Tomato healthy	1.00	1.00	1.00	97
Accuracy			0.97	1254
Macro average	0.97	0.97	0.97	1254
Weighted average	0.97	0.97	0.97	1254

A confusion matrix was plotted as in Figure 7 to analyze the misclassification between 15 different categorical plant disease classes. Each row of matrix represents 15 different predicted categorical classes while each column of matrix represents the original categorical class of plant disease. Confusion matrix in this work showed the overall classification accuracy, true positive and false rate and error rate of classification for 15 different original categorical classes. It also showed predicted plant diseases which were not classified correctly and the original plant diseases that they were mismatched with. Based on the confusion matrix, the diagonals showed that all the plant disease classes had been classified correctly, the performance of the CNN model is quite good and can extract the features well for plant disease classification.

Predicted Class	Healthy	Tomato_early_blight	Tomato_late_blight	Tomato_spider_mites	Tomato_spider_mites_Two_spotted_spider_mite	Tomato_spider_mites_Three_spotted_spider_mite	Tomato_spider_mites_Four_spotted_spider_mite	Tomato_spider_mites_Five_spotted_spider_mite	Tomato_spider_mites_Six_spotted_spider_mite	Tomato_spider_mites_Seven_spotted_spider_mite	Tomato_spider_mites_Eight_spotted_spider_mite	Tomato_spider_mites_Nine_spotted_spider_mite	Tomato_spider_mites_Ten_spotted_spider_mite	Tomato_spider_mites_Eleven_spotted_spider_mite	Tomato_spider_mites_Twelve_spotted_spider_mite	Tomato_spider_mites_Thirteen_spotted_spider_mite	Tomato_spider_mites_Fourteen_spotted_spider_mite	Tomato_spider_mites_Fifteen_spotted_spider_mite
Healthy	1.00	0.00	0.00	0.00	0.00	0.00	0.00	0.00	0.00	0.00	0.00	0.00	0.00	0.00	0.00	0.00	0.00	0.00
Tomato_early_blight	0.00	0.97	0.00	0.00	0.00	0.00	0.00	0.00	0.00	0.00	0.00	0.00	0.00	0.00	0.00	0.00	0.00	0.00
Tomato_late_blight	0.00	0.00	1.00	0.00	0.00	0.00	0.00	0.00	0.00	0.00	0.00	0.00	0.00	0.00	0.00	0.00	0.00	0.00
Tomato_spider_mites	0.00	0.01	0.00	0.95	0.00	0.00	0.01	0.00	0.00	0.00	0.00	0.00	0.00	0.00	0.00	0.00	0.00	0.00
Tomato_spider_mites_Two_spotted_spider_mite	0.00	0.00	0.00	0.02	0.96	0.00	0.00	0.00	0.00	0.00	0.00	0.00	0.00	0.00	0.00	0.00	0.00	0.00
Tomato_spider_mites_Three_spotted_spider_mite	0.00	0.00	0.00	0.00	0.00	1.00	0.00	0.00	0.00	0.00	0.00	0.00	0.00	0.00	0.00	0.00	0.00	0.00
Tomato_spider_mites_Four_spotted_spider_mite	0.00	0.00	0.00	0.00	0.00	0.00	0.96	0.00	0.00	0.00	0.00	0.00	0.00	0.00	0.00	0.00	0.00	0.00
Tomato_spider_mites_Five_spotted_spider_mite	0.00	0.00	0.00	0.00	0.00	0.00	0.00	1.00	0.00	0.00	0.00	0.00	0.00	0.00	0.00	0.00	0.00	0.00
Tomato_spider_mites_Six_spotted_spider_mite	0.00	0.00	0.00	0.00	0.00	0.00	0.00	0.00	1.00	0.00	0.00	0.00	0.00	0.00	0.00	0.00	0.00	0.00
Tomato_spider_mites_Seven_spotted_spider_mite	0.00	0.02	0.00	0.00	0.02	0.00	0.01	0.00	0.00	0.92	0.00	0.03	0.00	0.00	0.00	0.00	0.00	0.00
Tomato_spider_mites_Eight_spotted_spider_mite	0.00	0.00	0.00	0.03	0.00	0.00	0.00	0.00	0.00	0.00	0.94	0.03	0.00	0.00	0.00	0.00	0.00	0.00
Tomato_spider_mites_Nine_spotted_spider_mite	0.00	0.00	0.00	0.00	0.02	0.00	0.02	0.00	0.00	0.00	0.01	0.04	0.90	0.01	0.00	0.00	0.00	0.00
Tomato_spider_mites_Ten_spotted_spider_mite	0.00	0.00	0.00	0.00	0.00	0.00	0.00	0.00	0.00	0.00	0.00	0.00	0.00	0.98	0.00	0.00	0.00	0.00
Tomato_spider_mites_Eleven_spotted_spider_mite	0.00	0.00	0.00	0.00	0.00	0.00	0.00	0.00	0.00	0.00	0.00	0.00	0.00	0.00	1.00	0.00	0.00	0.00
Tomato_spider_mites_Twelve_spotted_spider_mite	0.00	0.00	0.00	0.00	0.00	0.00	0.00	0.00	0.00	0.00	0.00	0.00	0.00	0.00	0.00	1.00	0.00	0.00
Tomato_spider_mites_Thirteen_spotted_spider_mite	0.00	0.00	0.00	0.00	0.00	0.00	0.00	0.00	0.00	0.00	0.00	0.00	0.00	0.00	0.00	0.00	1.00	0.00
Tomato_spider_mites_Fourteen_spotted_spider_mite	0.00	0.00	0.00	0.00	0.00	0.00	0.00	0.00	0.00	0.00	0.00	0.00	0.00	0.00	0.00	0.00	0.00	1.00
Tomato_spider_mites_Fifteen_spotted_spider_mite	0.00	0.00	0.00	0.00	0.00	0.00	0.00	0.00	0.00	0.00	0.00	0.00	0.00	0.00	0.00	0.00	0.00	0.00

FIGURE 7. Confusion Matrix

The graph of training accuracy with respect to the epoch is plotted as in Figure 8 while the graph of training loss with respect to the epoch is also plotted as in Figure 9. The training loss and training accuracy have a good fit. The test accuracy was 97.2% while the test loss was 11.9%.

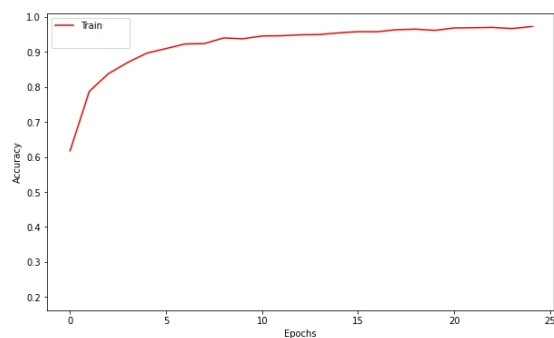


FIGURE 8. Model accuracy

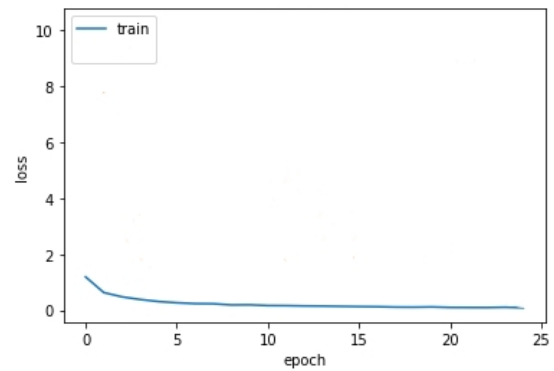


FIGURE 9. Model loss

Figure 10-12 shows results of the correctly classified predicted class from the test image dataset which are returned with the probability of the predicted class.

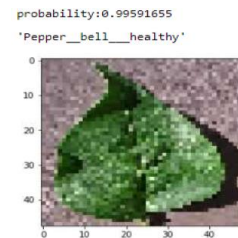


FIGURE 10. Classification of healthy pepper bell leaf

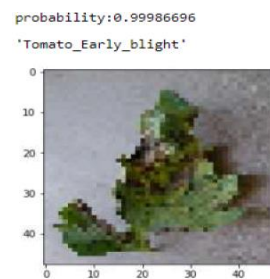


FIGURE 11. Classification of early blight tomato leaf

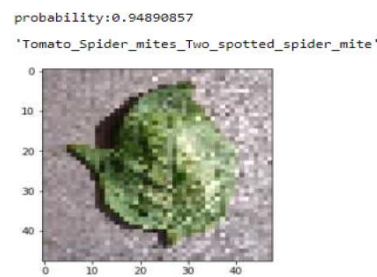


FIGURE 12. Classification of two spotted spider mite leaf

System Integration and model deployment

The leaf images are captured by using real camera and process by model via apps to form a real-time inference vision system. The developed model has been implemented in two applications, namely desktop application which was developed by using Tkinter on python (Figure 13) with high classification accuracy (Figure 14). and web application which was developed by using HTML and CSS (Figure 15) with high classification accuracy (Figure 16). It takes less than 1 second to detect and classify plant disease in web and desktop applications.

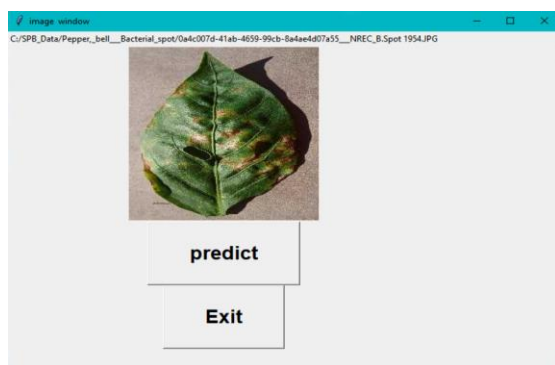


FIGURE 13. Desktop application load image



FIGURE 14. Desktop app classification

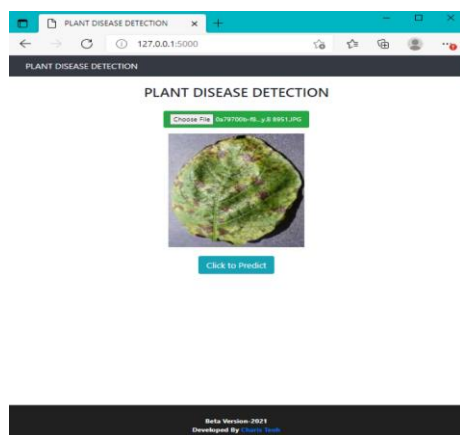


FIGURE 15. Web application load image

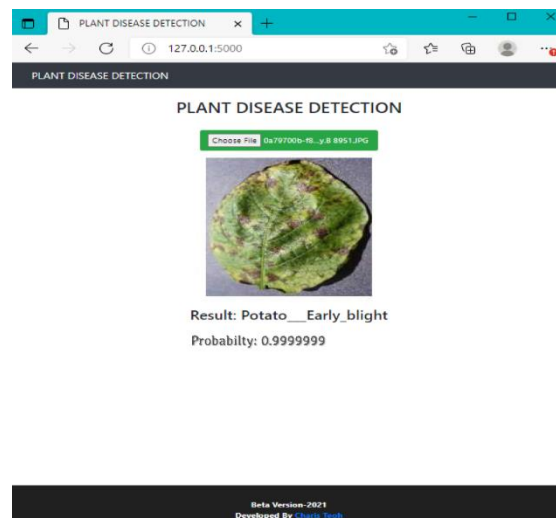


FIGURE 16. Web application classification

In Figure 17, pixy2 camera was used to integrate with web or desktop applications to form a real-time inference vision system for plant disease detection and classification. In this work, the images on computer screen that displays leave obtained from internet are captured by using the camera, which leads to poor quality images due to changes in lighting and exposure. Accuracy can be affected.



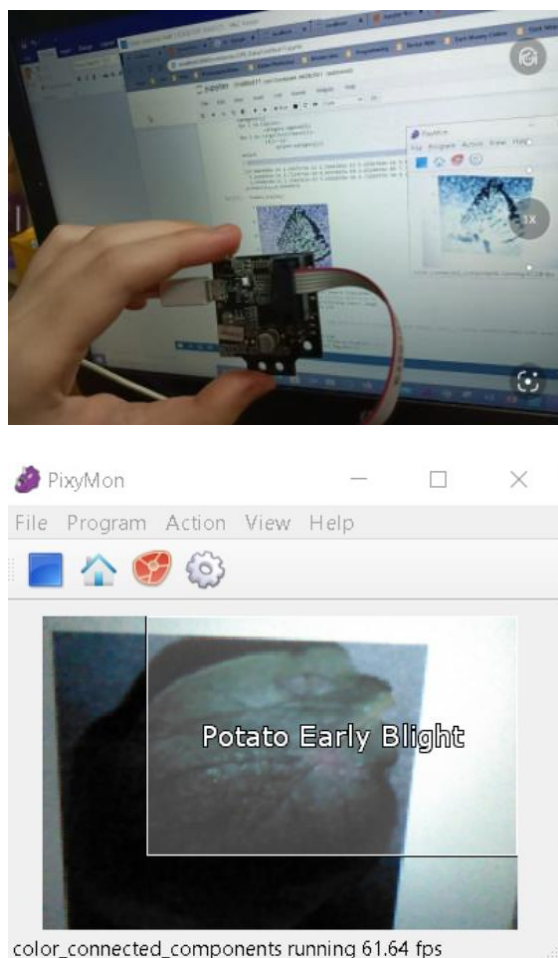


FIGURE 17. Real time inference vision system for plant disease detection and classification with CNN model.

CONCLUSION

In this work, the trained CNN model shows an accuracy of 97.2% and average F1 score of 97%. In conclusion, the trained CNN model can detect and classify plant disease accurately. The trained CNN model is deployed on web application and desktop application by connecting with camera to form a real-time inference vision system. It is able to produce a useful information for farmers to apply pesticide more effectively to cure plant disease. Thus, agricultural sector can be benefited. The accuracy of the model is seek to be improved in the future.

GPU has memory issue, therefore cannot do higher level deep processing. More power GPU with more memory is needed to realize deep CNN to extract more features of plant diseases. It is also suggested to capture the real leaf images with the camera to ensure higher accuracy in the future when the Covid-19 situation gets better. Besides that, due to the situation now, VNC Viewer is used to access the GPU. In the future, when GPU lab can be entered, the CNN model that is trained can be

deployed with Pixy2 camera which is connected to the GPU to show the real-time inference vision system. The name of the plant disease will be shown directly on the AI camera when the leaf appeared on the AI camera. Since the system is trained with only 3 classes and 15 types of plant diseases, the system is proposed to be trained with many other plants and diseases to further increase the scope of the system. Extraction of many more features of the plants can be done by adding many more images of other plants to improve the accuracy of the system. By capturing many different types of plant images to add to the dataset, this dataset can be further used to build better models. Improvement of accuracy by using better algorithms in the future is proposed. An efficient bulk or spot spraying system by using the plant disease classification system is also proposed to be done in the future.

ACKNOWLEDGEMENT

Thank you to Universiti Kebangsaan Malaysia for the grant. Also thank you to supervisor Dr. Gan Kok Beng who provided unconditional support throughout this project.

REFERENCES

- Albawi, S., Mohammed, T. A., & Al-Zawi, S. 2017. Understanding of a Convolutional Neural Network. 2017. *2017 International Conference on Engineering and Technology (ICET)*. DOI: 10.1109/icengtechnol.2017.8308186.
- Arsenovic, M., Karanovic, M., Sladojevic, S., Anderla, A. & Stefanovic, D. 2019. Solving Current Limitations of Deep Learning Based Approaches for Plant Disease Classification. *Symmetry* 11(7):1-21. DOI:10.3390/sym11070939.
- Asfarian, A., Herdiyani, Y., Rauf, A., & Mutaqin, K. H. 2013. Paddy Diseases Identification with Texture Analysis using Fractal Descriptors Based on Fourier Spectrum. Jakarta. *2013 International Conference on Computer, Control, Informatics and Its Applications (IC3INA)*: 77-81.
- Badgujar, V. R., Ner, A. R., Jadhav, H. S. & Magare, R. S. 2021. Mobile Application for Plant Disease Recognition Using Transfer Learning. *International Research Journal of Engineering and Technology (IRJET)* 8(5): 3462-3465.
- Barbedo, J. G. A. 2016. A Review on The Main Challenges in Automatic Plant Disease Identification Based on Visible Range Images. *Biosystems Engineering* 144: 52-60. DOI:10.1016/j.biosystemseng.2016.01.017.
- Bedi, P. & Gole, P. 2021. Plant disease classification

- using hybrid model based on convolutional autoencoder and convolutional neural network. *Artificial Intelligence in Agriculture* 5: 90-101. DOI: 10.1016/j.aiia.2021.05.002.
- Bhangea, M. & Hingoliwala, H. A. 2015. Smart Farming: Pomegranate Disease Detection Using Image Processing. *Procedia Computer Science* 58: 280-288.
- Bhise, N., Kathet, S., Jaiswar, S. & Adgaonkar, A. 2020. Plant Disease Classification using Machine Learning. *International Research Journal of Engineering and Technology* 7(7): 2924-2929.
- Chapaneri, R., Desai, M., Goyal, A., Ghose, S. & Das, S. V. 2020. Plant Disease Detection: A Comprehensive Survey. India. 2020 3rd *International Conference on Communication System, Computing and IT Applications (CSCITA)*: 220-225.
- Chowdhury, M. E. H., Rahman, T., Khandakar, A., Ayari, M. A., Khan, A. U., Khan, M. S., Al-Emadi, N., Reaz, M. B. I., Islam, M. T. & Ali, S. H. M. 2021. Automatic and Reliable Leaf Disease Classification Using Deep Learning Techniques. *AgriEngineering* 3:294-312. DOI:10.3390/agriengineering3020020.
- Dhingra, G., Kumar, V., & Joshi, H. D. 2017. Study of Digital Image Processing Techniques for Leaf Disease Detection and Classification. *Multimedia Tools and Applications* 77(2): 1-50. DOI: 10.1007/s11042-017-5445-8.
- Gajanan, D. E., Shankar, G. G., & Keshav, G. V. 2018. Detection of Leaf using Feature Extraction for Android Based System. *International Journal of Scientific Research in Science and Technology (IJSRST)* 4(2): 450-456.
- Gogul, I. & Kumar, V. S. 2017. Flower Species Recognition System using Convolutional Neural Networks and Transfer Learning. 2017 4th *International Conference on Signal Processing, Communications and Networking (ICSCN-2017)*: 1-6. DOI: 10.1109/ICSCN.2017.8085675.
- Gupta, L., Intwala, K., Khetwani, K., Hanamshet, T. & Somkunwar, R. 2017. Smart Irrigation System and Plant Disease Classification. *International Research Journal of Engineering and Technology* 4(3): 80-83.
- Harte, E. 2020. Plant Disease Classification using CNN. National College of Ireland. *IEEE*. DOI: 10.13140/RG.2.2.36485.99048.
- Hassan, S. M., Maji, A. K., Jasiński, M., Leonowicz, Z. & Jasińska, E. 2021. Identification of Plant-Leaf Diseases Using CNN and Transfer-Learning Approach. 2021. *Electronics* 10(1388). DOI: 10.3390/electronics10121388.
- Jacob, P. M., Suresh, S., John, J. M., Nath, P., Nandakumar, P. & Simon, S. 2020. An Intelligent Agricultural Field Monitoring and Management System using Internet of Things and Machine Learning. 2020 *International Conference on Data Analytics for Business and Industry: Way Towards a Sustainable Economy (ICDABI)*: 1-5. DOI:10.1109/ICDABI51230.2020.9325612.
- Justine, B., Samuel, F., Jérôme, T. & St-Charles Pierre-Luc. 2019. Convolutional Neural Networks for the Automatic Identification of Plant Diseases. *Frontiers in Plant Science* 10:941. DOI: 10.3389/fpls.2019.00941.
- Kaur, G., Kaur, S. & Kaur, A. 2018. Plant Disease Detection: a Review of Current Trends. *International Journal of Engineering & Technology (IJET)* 7(3.34): 874-881.
- Keerthi, J., Maloji, S. & Krishna, P. G. 2019. An Approach of Tomato Leaf Disease Detection Based on SVM Classifier. *International Journal of Recent Technology and Engineering (IJRTE)* 7(6): 697-704.
- Khirade, S. D. & Patil, A. B. 2015. Plant Disease Detection Using Image Processing. *International Conference on Computing Communication Control and Automation*: 768-771.
- Khurana, J., Sharma, A., Chhabra, H. S. & Nijhawan, R. 2019. An Integrated Deep Learning Framework of Tomato Leaf Disease Detection. *International Journal of Innovative Technology and Exploring Engineering (IJITEE)* 8(11S): 46-50.
- King, A. 2017. Technology: The Future of Agriculture. *Nature* 544 (7651):21-23. DOI: 10.1038/544S21a.
- Kulinavar, P. & Hadimani, V. I. 2017. Classification of leaf diseases based on multiclass SVM classifier. *International Journal of Advance Research, Ideas and Innovations in Technology (IJARIIT)* 3(4): 321-325.
- Kumar, S. S. & Raghavendra, B. K. 2019. Diseases Detection of Various Plant Leaf Using Image Processing Techniques: A Review. India. *International Conference on Advanced Computing & Communication Systems (ICACCS)*: 313-316. DOI: 10.1145/3371158.3371196.
- Liu, J., Wang, X. 2021. Plant diseases and pests detection based on deep learning: a review. *Plant Methods* 17 (22). DOI: 10.1186/s13007-021-00722-9 [20 July 2021]
- Mehmood ul Hasan, Ullah, S., Muhammad Jaleed Khan & Khurshid, K. 2019. Comparative Analysis of SVM, ANN and CNN for Classifying Vegetation Species using Hyperspectral Thermal Infrared Data. 2017 *The International Archives of the Photogrammetry, Remote Sensing and Spatial Information Sciences, Volume XLII-2/W13, 2019 ISPRS Geospatial Week 2019*:

- 1861-1868. DOI: 10.5194/isprs-archives-XLII-2-W13-1861-2019.
- Mesterházy, Á., Oláh, J. & Popp, J. 2020. *Topology: Losses in the Grain Supply Chain: Causes and Solutions*. Hungary. *MDPI* 12(6): 2342.
- Mohammad Aminul Islam, Md. Sayeed Iftekhhar Yousuf & Billah, M. M. 2019. Automatic Plant Detection Using HOG and LBP Features with SVM. Bangladesh. *International Journal of Computer (IJC)* 33(1): 26-38.
- Mohanty, S. P., Hughes, D. P. & Salathé, M. 2016. Using Deep Learning for Image-Based Plant Disease Classification. *Frontiers in Plant Science*. DOI: 10.3389/fpls.2016.01419.
- Petrellis, N. 2019. Plant Disease Diagnosis for Smart Phone Applications with Extensible Set of Diseases. *Applied Sciences* 9: 1-22. DOI: 10.3390/app9091952.
- Ramcharan, A., McCloskey, P., Baranowski, K., Mbilinyi, N., Mrisho, L., Ndalawha, M., Legg, J. & Hughes, D. P. 2019. A Mobile-Based Deep Learning Model for Cassava Disease Diagnosis. *Frontiers in Plant Science* 10: 272. DOI=10.3389/fpls.2019.00272.
- Rani, S. J., Akshayaa, P., Anushree., P. & Asmitha., S. 2019. An Open CV Based Automatic Leaf Disease Identification and Fertilized Agrobot Using IOT. India. *IJCESR* 6(3).
- Rishiikeshwer, B. S., Shriram, T. A., Raju, J. S., Hari, M. B. S & Brindha, G. R. 2019. Farmer-Friendly Mobile Application for Automated Leaf Disease Classification of Real-Time Augmented Data Set using Convolution Neural Networks. *Journal of Computer Science* 16(2): 158-166.
- Sagar, A. & Dheeba, J. 2020. On Using Transfer Learning For Plant Disease Classification. *bioRxiv*. DOI: 10.1101/2020.05.22.110957.
- Santhosh, K. S. & Raghavendra, B. K. 2019. Diseases Classification of Various Plant Leaf Using Image Processing Techniques: A Review. India. *International Conference on Advanced Computing & Communication Systems (ICACCS)*: 313-316. DOI: 10.1109/ICACCS.2019.8728325.
- Shao, Y., Xuan, G., Zhu, Y., Zhang, Y. & Peng H. 2017. Research on Automatic Identification System of Tobacco Diseases. *The Imaging Science Journal* 65 (4): 252-259. DOI:10.1080/13682199.2017.1319609.
- Sharma, P., Berwal, Y. P. S & Ghai, W. 2019. Performance Analysis of Deep Learning CNN Models for Disease Classification in Plants using Image Segmentation. *Image Processing in Agriculture* 7(4): 566-574. DOI: 10.1016/j.inpa.2019.11.001.
- Sharma, P., Berwal, Y. P. S. & Krishimtr, W. G. 2018. Using Machine Learning to Identify Diseases in Plants. *IEEE International Conference on Internet of Things and Intelligence System (IOTAIS)*: 29-34.
- Sheikh Mohammad Fakhrul Islam & Karim, Z. 2019. World's Demand for Food and Water: The Consequences of Climate Change. DOI: 10.5772/intechopen.85919.
- Singh, D., Jain, N., Jain, P., Kayal, P., Kumawat, S. & Batra, N. 2020. PlantDoc: A Dataset for Visual Plant Disease Detection. India. *CoDS COMAD 2020: 7th ACM IKDD CoDS and 25th COMAD*: 249-253. DOI: 10.1145/3371158.3371196.
- Singh, V. P. & Misra, A. K. 2017. Detection of Plant Leaf Diseases using Image Segmentation and Soft Computing Techniques. *Information Processing in Agriculture* 4(1): 41-49.
- Sladojevic, S., Arsenovic, M., Anderla, A., Culibrk, D. & Stefanovic, D. 2016. Deep Neural Networks Based Recognition of Plant Diseases by Leaf Image Classification. *Computational Intelligence and Neuroscience* 2016(6): 1-11. DOI: 10.1007/s11042-017-5445-8.
- Srivastava, P., Mishra, K., Awasthi, V., Sahu, V. & Pal, P. K. 2021. Plant Disease Classification Using Convolutional Neural Network. *International Journal of Advanced Research* 9(1): 691-698. DOI:10.21474/IJAR01/12346.
- Toda, Y. & Okura, F. 2019. How Convolutional Neural Networks Diagnose Plant Disease. *Plant Phenomics* 2019:1-14. DOI: 10.34133/2019/9237136.
- Wen, P. & Berry, E. M. 2018. The Concept of Food Security. *Encyclopedia of Food Security and Sustainability* 2: 1-7. DOI: 10.1016/B978-0-08-100596-5.22314-7.
- Yang, L., Jing, N. & Chao, X. 2020. Do We Really Need Deep CNN for Plant Diseases Identification? *Computers and Electronics in Agriculture* 178. DOI: 10.1016/j.compag.2020.105803.
- Yang, M., Li, D., Chen, M., Bouras, A., Tang, Y. & Yu, X. 2020. The Implementation of A Crop Diseases APP Based on Deep Transfer Learning. *3rd International Conference on Artificial Intelligence and Big Data (ICAIBD)*: 22-28. DOI: 10.1109/ICAIBD49809.2020.9137469.
- Zhang, S., Wuc, X., You, Z. & Zhang, L. 2017. Leaf Image Based Cucumber Disease Recognition using Sparse Representation Classification. *Computers and Electronics in Agriculture* 134: 135-141.

Optimize Neural Network Implementation on FPGA

(Mengoptimumkan Pelaksanaan Rangkaian Neural Pada FPGA)

Chia Tieng Tieng, Sawal Hamid Md Ali

Department of Electrical, Electronic and Systems,

Faculty of Engineering & Built Environment, Universiti Kebangsaan Malaysia, Malaysia

*Corresponding author: A165589@siswa.ukm.edu.my

ABSTRACT

The use of Field Programmable Gate Arrays (FPGA) is growing rapidly in various field. Due to its reconfigurable ability, FPGA have become one of the essential components in data processing and communication systems such as implementing artificial neural network into FPGA. Recent developments in computing technology not only influenced software filed but also helped the use of custom logic design in hardware platform, namely Hardware/Software (HW/SW) Co-design System. In general, Convolutional Neural Network (CNN) are highly-efficient and accurate for classifying the objects. One type of CNN is called Region-based Convolutional Neural Network (RCNN). In this study, RCNN is the network selected to implement the HW/SW system. The Viola-Jones algorithm is also very useful for object detection and this algorithm can be achieved and implemented in Matlab software. In addition, the HW/SW system runs in Zynq-7000 SoC hardware with AXI DMA and ARM processor. The hardware system design has been achieved for data transfer from PL to PS and save the data to BRAM memory. In addition, CNN IP core which represents the CNN architecture as well as weight and bias of network layers, especially convolutional layer and fully connected layer also been planned. Face recognition application for embedded software system will also be designed for face classification and prediction. In this study, RCNN has been successfully designed and trained. Subsequently, it is implemented in hardware for use in the embedded software application. Hardware implementation was achieved with a maximum FPGA usage of 67 18k BRAM, 115 DSP48E, 10779 FF and 17102 LUT with an on-chip power consumption of 1.879 Watts. This meets the resource requirements of the FPGA. The results show that the artificial neural network can be implemented in FPGA to achieve hardware implementation of face recognition system.

Keywords: FPFA; CNN; Face recognition; HW/SW co-design

ABSTRAK

Penggunaan Field Programmable Gate Arrays (FPGA) berkembang pesat dalam pelbagai bidang. Oleh sebab kemampuan untuk dikonfigurasi semula, FPGA telah menjadi salah satu komponen yang penting dalam sistem pemprosesan data dan komunikasi seperti melaksanakan rangkaian neural pada FPGA. Perkembangan teknologi pengkomputeran baru-baru ini tidak hanya mempengaruhi perisian tetapi juga membantu penggunaan reka bentuk logik tersesuai pada platform perkakasan, iaitu reka bentuk sistem perkakasan dan perisian (HW/SW). Secara umum, rangkaian neural konvolusi (CNN) adalah sangat cekap dan tepat untuk mengklasifikasikan objek. Salah satu jenis CNN ialah Region-based Convolutional Neural Network (RCNN). RCNN dipilih untuk melaksanakan sistem HW/SW dalam kajian ini. Algoritma Viola Jones juga sangat berguna untuk mengesan objek dan boleh dilaksanakan dalam perisian Matlab. Sistem HW/SW dijalankan dalam perkakasan Zynq-7000 SoC dengan AXI DMA dan ARM pemproses. Reka bentuk sistem perkakasan telah dirancang untuk pemindahan data dari PL ke PS dan simpan data ke memori BRAM. Selain itu, blok IP CNN yang mewakili seni bina CNN dan juga data berat dan bias juga telah dirancang. Algoritma pengesanan wajah untuk sistem perisian terbenam dalam FPGA juga akan dirancang untuk klasifikasi dan ramalan wajah. Dalam kajian ini, RCNN telah berjaya direka bentuk dan dilatih dan seterusnya melaksanakannya dalam perkakasan untuk digunakan dalam aplikasi perisian terbenam. Pelaksanaan perkakasan telah dicapai dengan penggunaan maksimum FPGA sebanyak 67 18k BRAM, 115 DSP48E, 10779 FF dan 17102 LUT dengan penggunaan kuasa cip 1.879 Watts. Ini memenuhi keperluan sumber FPGA. Hasilnya menunjukkan rangkaian neural dapat dilaksanakan dan dicapai dalam FPGA untuk melaksanakan sistem pengesanan wajah

Kata Kunci: Pemandu; FPGA; CNN; Pengesanan wajah; Reka bentuk Bersama HW/SW

INTRODUCTION

A security recognition system that will use physical features such as a person's face, fingerprints and iris have been considered primarily for the security system called 'Biometric system'. In facial recognition algorithm, artificial neural network is used in this study because it is useful and popular for classifying complex data such as face data. Neural network classifiers can be used in a variety of applications such as facial recognition. It requires huge works to develop an algorithm that able to process and classify the images efficiently.

ANN are very useful because they have strengths and numerical values which can perform more than one task or job at the same time. However, due to lack of tools to port CNN on the FPGA, the purpose of this thesis is to outline the overall resources and tools available to implement CNN facial recognition into the FPGA.

Viola-Jones algorithm which detects the predefined features that can be found in the images. This algorithm consists of Haar features, integral images, Adaboost training and classifier cascading to achieve face detection. Defining the key features and using them in optimal way is the hardest part in this algorithm (Smriti Tikoo & Nitin Malik 2016). In contrast to defining features, CNN algorithm is used to learn the features from the huge image dataset. To detect and recognize the objects precisely, CNN had to perform an intensive computing operation with floating point numbers.

Artificial Neural Network (ANN) are an information processing paradigm, which is inspired by the way biological nervous systems, such as brain, to process the information. CNN had become increasingly popular for being able to run the tracking and object recognition on specific tasks and easy to build compared to other algorithms.

Modern computer science creates connection-based systems that used to model the biological neurons as nodes and perform various interactions between network components. It is performed by the use of weight, bias and activation function. Neural network can perform tasks without being programmed precisely and performance can be improved by data learning. The neural network consists of nodes (such as brain neurons) and are interconnected in the input layer, hidden layer and output layer. Nodes are determined by weight and bias while function activation is specified to activate the output.

The implementation of CNN model on FPGA is due to they offer a flexible and energy efficient solution. FPGA based computing architecture can be reconfigured with parallel capabilities are very useful for implementing neural networks. In this study, the design for data transfer from Programmable Logics (PL) and Processing Systems (PS) to DDR memory had been discussed. The entire Hardware/Software Co-design of FPGA with block IP CNN and processor ARM will be implemented in the platform Vivado.

METHODOLOGY

The methodology of this study is divided into two levels. The first stage is Matlab-based facial recognition system using the Viola-Jones algorithm and RCNN. The second stage is Hardware/Software (HW/SW) implementation.

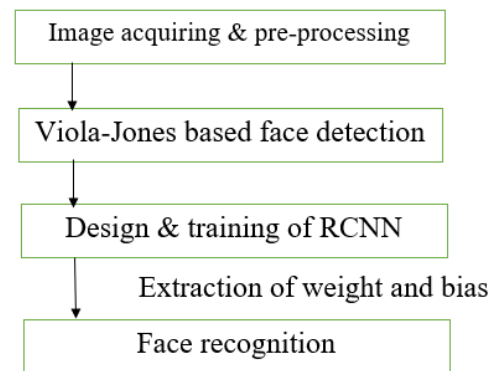


Figure 1 : Flow of Matlab-based face recognition

First, collect faces from 2 different individuals as dataset. Each database consists of 400 cropped face images of 300×300 pixels. The total dataset will be divided by 2, which are 640 training dataset and 160 testing datasets. Second, detect the face in the image by using the Cascade Object Detector which is based on Viola-Jones algorithm in the Matlab. Next, design and train the RCNN. Figure 2 shows the architecture of RCNN which is built of 15 network layers in total which are input layer, convolutional layer, ReLU layer, Max Pooling layer, Fully Connected layer, softmax layer and output layer.

No	Layer type	Activation function
1	Input image	96×96×3
2	Convolutional	23×23×6
3	ReLU	23×23×6
4	Max Pooling	11×11×6
5	Convolutional	11×11×16
6	ReLU	11×11×16

7	Max Pooling	4×4×16
8	Convolutional	4×4×16
9	ReLU	4×4×16
10	Max Pooling	2×2×16
11	Fully Connected	1×1×100
12	ReLU	1×1×100
13	Fully Connected	1×1×2
14	Softmax	1×1×2
15	Classification output	-

Table 1 : Architecture of RCNN

After the design of RCNN, train the network to classify the faces from the dataset by following the training parameter which is showed as Table 2. The training parameter includes training type, minimum batch size, initial training rate and maximum epoch.

Training type	sgdm
Minimum batch size	128
Initial training rate	0.00001
Maximum epoch	5

Table 2 : Training Parameter

After the training of RCNN, start extracting the weight and bias from each network layers, especially Convolutional layers and Fully Connected layers in the form of matrices which is showed as Table 3. A parameter file which includes the weight and bias in the form of matrices is created for the use of C-based hardware design of the CNN module.

No	Layer type	Weight	Bias
1	Input Image	-	-
2	Convolutional	5×5×3×6	1×1×6
3	ReLU	-	-
4	Max Pooling	-	-
5	Convolutional	5×5×6×16	1×1×16
6	ReLU	-	-
7	Max Pooling	-	-
8	Konvolusi	5×5×16×16	1×1×16
9	ReLU	-	-
10	Max Pooling	-	-
11	Fully Connected	100×64	100×1
12	ReLU	-	-
13	Fully Connected	2×100	2×1
14	Softmax	-	-
15	Classification Output	-	-

Table 3 : Weight and Bias of RCNN

For Hardware/Software co-design, Zedboard Development Kit is chosen as the hardware platform which is showed as Figure 2. This board includes Xilinx Z-7020 chip and its specification are showed as Table 4. It consists of Programmable Logics (PL), Look Up Tables (LUT), Flip Flop (FF), Block Random Access Memory (BRAM) and Digital Signal Processing (DSP) slices. For the CNN IP core design, the available RAM usage is 4.9 Mb.



Figure 2 : Zedboard Development Kit

Device Name	Z-7020
Body Part	XC7Z020
Xilinx 7 Series Programmable Logic (PL)	Artix-7 FPGA
PL cells	85K
LUT	53200
FF	106400
BRAM	4.9 Mb
DSP Slices	220

Table 4 : Zynq-7000 SoC Specification

For the C-based hardware design of CNN IP core, the platform used is Vivado HLS. The module designed can be used to classify the class of objects from the input image by using deep learning algorithm. A neural network code is written and created for the use of synthesis of CNN IP core in C programming language and HLS script. In this study, AXI4 stream interface is chosen for communication system in the CNN IP core. The AXI4 stream includes TDATA, TSTRB, TKEEP, TLAST, TID, TDEST and TUSER. Table 5 shows the bandwidth of signal required for the design of CNN IP core.

AXI4 Stream Signal	Bandwidth
TDATA	32
TSTRB	4
TKEEP	4
TLAST	0
TID	0
TDEST	0
TUSER	0

Table 5 : AXI4 Stream Signal Bandwidth

Once the CNN IP core is successfully generated, it is imported to the Vivado Design Suite for hardware block diagram design. Figure 3 shows the top-level functional diagram of hardware system.

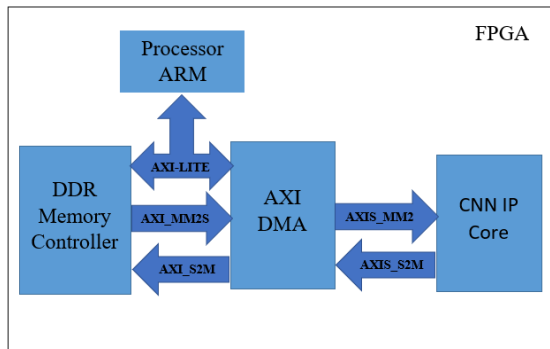


Figure 3 : Hardware System Diagram

From Figure 3, DMA is used to transfer the data from memory to CNN IP core and then back to the memory. Processor ARM and DDR memory controller behaves within Zynq PS while CNN IP core and AXI behaves within Zynq PL. AXI-lite bus allows processor interacts with AXI DMA to control, start and monitor the data transfer. AXI_MM2S and AXI_S2MM are memory-mapped AXI4 bus which provide accessibility of DMA to DDR memory. AXIS_MM2S and AXIS_S2MM are AXI4 stream bus which allow dataflow without memory address.

After the hardware block diagram is successfully validated, start generation of bitstream and export the bitstream to the Vivado SDK. For the HW/SW implementation, an embedded HW/SW system design is required for face recognition by using CNN and it is written in C programming language.

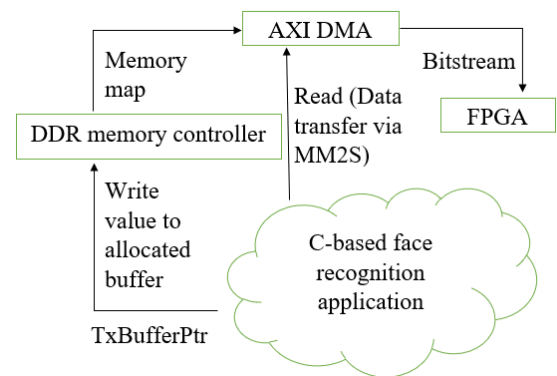


Figure 4 : HW/SW Embedded System for DMA Read Transaction

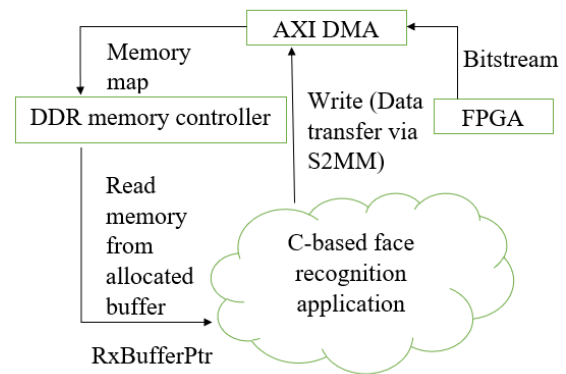


Figure 5 : HW/SW Embedded System for DMA Write Transaction

DMA transaction is a completed I/O operation such as single read and write request from the application. Allocated buffer within the DMA can be divided within the memory without continuous allocation from the DDR memory controller. For the DMA, MM2S is used for data transfer from DDR memory to FPGA while the S2MM is used to transfer the data to DDR memory. In this study, DMA read and write transaction for the HW/SW embedded system are showed as Figure 4 and Figure 5.

Figure 6 shows the flow chart for C-based face recognition application used in this study. Before the embedded software implemented into the FPGA, the system already includes the hardware system design with CNN IP core. First, choose an input image in the form of hexadecimal into the C application. After that, read the image bytes and label. If the system fails to read them, it will back to the start. Otherwise the system starts the face recognition with label to predict the class of the given image.

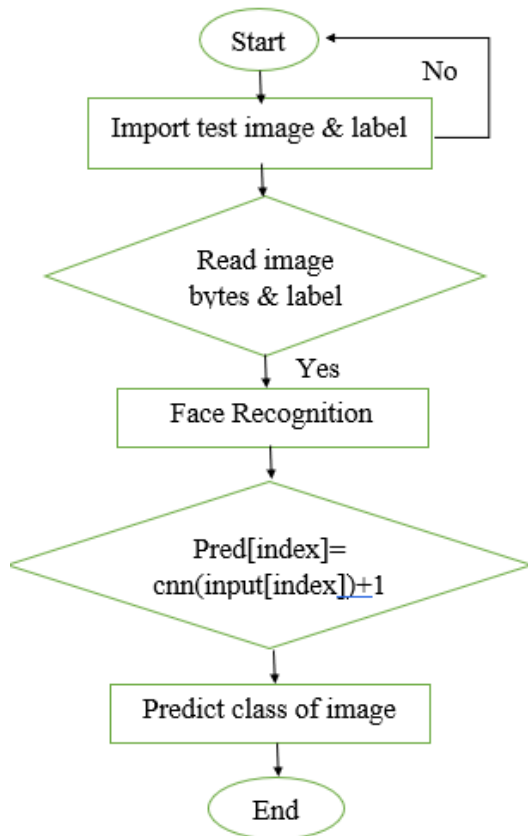


Figure 6 : Flow Chart of Face Recognition Application

RESULTS AND DISCUSSION

In this study, the results are obtained after 2 stages. First stage is Matlab-based face recognition and the second stage is HW/SW implementation.

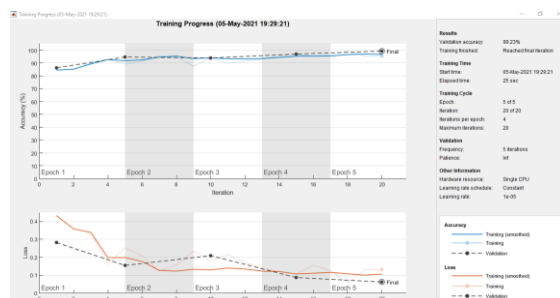


Figure 7 : Graph of RCNN Training

From the Figure 7, it shows the accuracy of network training is 99.23%. The accuracy differs with the network design and architecture.

Utilization Estimates					
Summary					
Name	BRAM_18K	DSP48E	FF	LUT	URAM
DSP	-	-	-	-	-
Expression	-	-	0	12	-
FIFO	0	-	10	88	-
Instance	47	115	10639	16982	0
Memory	20	-	128	2	0
Multiplexer	-	-	-	18	-
Register	-	-	2	-	-
Total	67	115	10779	17102	0
Available	280	220	106400	53200	0
Utilization (%)	23	52	10	32	0

Table 6 : Resource Usage of CNN IP Core

Table 6 shows that 67 BRAM (23%), 115 DSP slices (52%), 10779 FF (10%) and 17102 LUT (32%) are used to generate the CNN IP core. They are not exceed the available FPGA resource requirement and free to use in the hardware system.

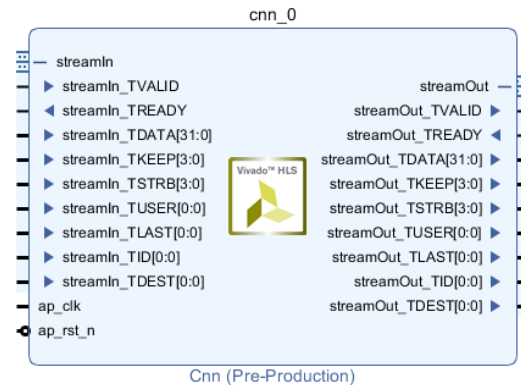


Figure 8 : Architecture of CNN IP Core

Figure 8 shows the structure of CNN IP core generated includes 7 AXI4 stream signals which are TDATA, TKEEP, TSTRB, TUSER, TLAST, TID and TDEST. This IP core allows dataflow of 32 bit.

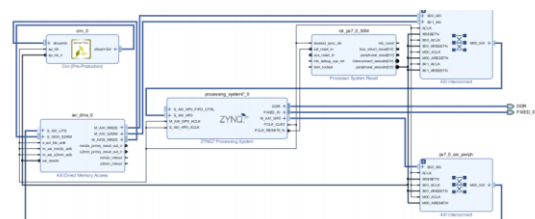


Figure 9 : FPGA Block Diagram

Figure 9 shows the FPGA block diagram with CNN IP core, processor ARM and AXI DMA. The hardware design includes the Zynq7 Processing System, AXI DMA, 2 AXI Interconnect, Processor System Reset and CNN IP

Core. Zynq PS transfers the data to AXI DMA via AXI Interconnect. CNN IP Core receives the bitstream from DMA and then DMA sends it back to the processor ARM.

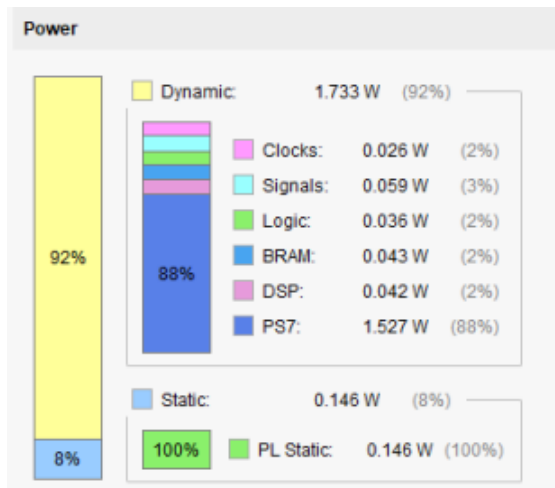


Figure 10 : Power Report

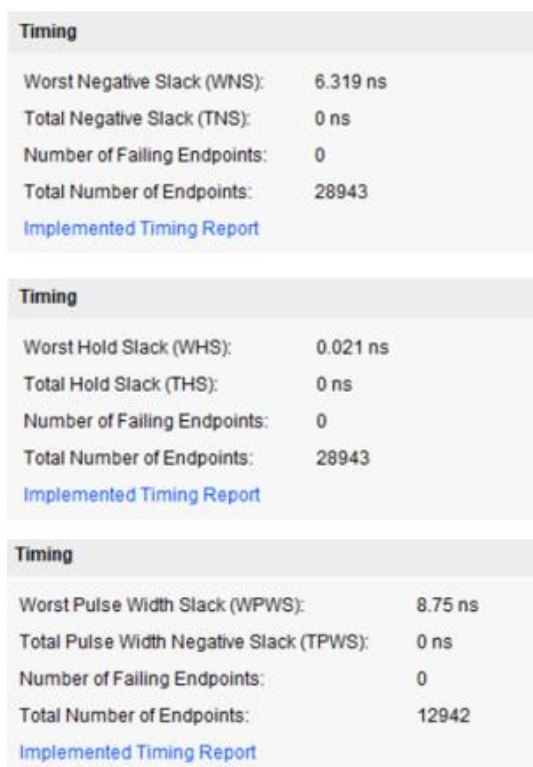


Figure 11 : Timing Report

Figure 10 shows the total power usage on chip is 1.879 W where 92% (1.733 W) is used for dynamic power while 8% (0.146 W) for static power. From Figure 11, it shows the timing is fulfilled with 0 failing endpoints and 0 negative slacks for setup, hold and pulse width.

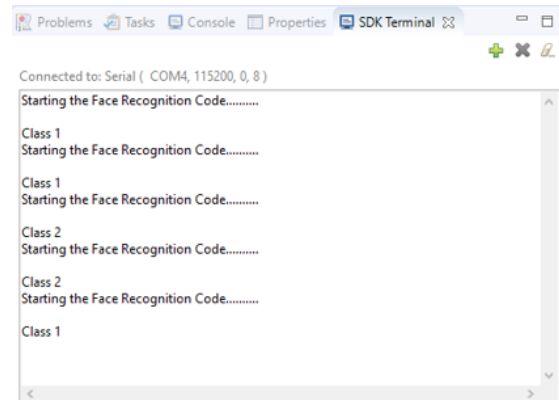


Figure 12 : Face Recognition Result

From Figure 12, it shows that the system is successfully classify and predict the class of 5 input test images one by one. Class 1 means detection of Individual 1 and Class 2 means detection of Individual 2.

CONCLUSION

In conclusion, the study proves that the designed embedded face recognition software is suitable and successful for FPGA SoC implementation with the RCNN module by using Vivado. This system achieves the FPGA resource requirement of 67 18K BRAM, 115 DSP48E, 10779 FF and 17102 LUT with power-on-chip of 1.879 Watts. Finally, 5 input images are all tested, classified and predicted correctly.

ACKNOWLEDGEMENT

The author wishes to express deepest appreciation to Prof. Dr. Sawal Hamid Md Ali for giving advices and guidance on this project. Thanks for the support of hardware to this project. Finally, thanks to Dr. Asma binti Abu Samah for the conduction of technical seminar to increase our thesis and journal writing skills and giving patience when having the questions related to the papers.

REFERENCES

- Smriti Tikoo, Nitin Malik. 2016. Detection of Face using Viola Jones and Recognition Using Back Propagation Neural Network.
- Yashwanth M. 2019. Face-Recognition-by-CNN.
- Pranav KB, Manikandan J. 2020. Design and Evaluation of a Real-Time Face Recognition System using Convolutional Neural Networks.
- J. Zou, R. Song. 2018. Microarray camera image segmentation with Faster-RCNN.

- J. Teich. 2012. Hardware/Software Codesign: “The past, the present, and predicting the future, Proceedings”.
- L. Shang, R. Dick, N. K Jha. 2007. “SLOPES: Hardware-software cosynthesis of low-power real-time distributed embedded systems with dynamically reconfigurable FPGAs”.
- Md Mahmudul Islam. 2019. Region-Based Convolutional Neural Network and Implementation of the Neural through Zedboard Zynq.
- Tilottoma Barua. 2020. Data Transfer Performance Analysis From Programmable Logic To Processing System of Zynq 7000.
- Irene De Rose, Matteo De Silvestri, Andea Solazzo. 2016. CNN2ECST Xilinx Open Hardware Contest 2016 Report.
- Hannes Kinks. 2016. Implementating Neural Networks on Field Programmable Gate Array.
- Xiaoguang Li. 2004. A Hardware/Software Co-Design Approach For Face Recognition by Artificial Neural Networks.
- Narayan T. Deshpande, Ravishankar. 2017. Face Detection and Recognition using Viola-Jones algorithm and Fusion of PCA and ANN.
- Human Samii Moghadam. 2018. Design Exploration of an FPGA Based Face Detection Processing Core Utilizing High Level Synthesis.
- Hanh Phan-Xuan, Thuong Le-Tien, Sy Nguyen-Tan. 2019. FPGA Platform applied for Facial Expression Recognition System using Convolutional Neural Networks.
- Changpei Qiu, Xinan Wang, Tianxia Zhao, Qiuping Li, Bo Wang, Hu Wang. 2021. An FPGA-Based Convolutional Neural Network Coprocessor.
- Bing Liu, Danyin Zou, Lei Feng, hou Feng, Fing Fu, Junbao Li. 2019. An FPGA-Based CNN Accelerator Integrating Depthwise Separable Convolution.
- Smrity Bhattarai. 2017. Digital Architecture For Real-Time Face Detection For Deep Video Packet Inspection Systems.
- Li Luo, Yakun Wu, Fei Qiao, Yi Yang, Qi Wei, Xiaobo Zhou, Yongkai Fan, Shuzheng Xu, Xinjun Liu, Huazhong Yang. 2018. Design of FPGA-Based Accelerator for Convolutional Neural Network under Heterogeneous Computing Framework with OpenCL.
- Tomyslav Sledevic, Arturas Serackis. 2020. mNet2FPGA: A Design Flow for Mapping a Fixed-Point CNN to Zynq SoC FPGA.
- Linus Pettersson. 2020. Convolutional Neural Networks on FPGA and GPU on the Edge: A Comparison.
- Sheiping Zhai, Cheng Qiu, Yuanyuan Yang, Jing Li, Yiming Qiu. 2019. Design of Convolutional Neural Network Based on FPGA.
- Lester Kalms, Pedram Amini Rad, muhammad Ali, Arsany Iskander & Diana Gohringer. 2021. A Parametrizable High-Level Synthesis Library for Accelerating Neural Networks on FPGAs.
- Antonios Georgios Pistis. 2018. Design and Implementation of an FPGA-Based Convolutional Neural Network Accelerator.
- Su Yi, Hu Xiao, Sun Yongjie. 2018. FPGA Accelerating Core Design Based on XNOR Neural Network Algorithm.
- Alireza Ghaffari, Yvon Savaria. 2020. CNN2Gate: An Implementation of Convolutional Neural Networks Inference on FPGAs with Automated Design Space Exploration.
- Gianmarco Dinelli, Gebriele Meoni, Emilio Rapuano, Gionata Benelli, Luca Fanucci. 2019. An FPGA-Based Hardware Accelerator for CNNs Using On-Chip Memories Only: Design and Benchmarking with Intel Movidius Neural Compute Stick.
- P Muthu Krishnammal, T V Padmavathy, M Shakunthala, M N Vimal Kumar. 2021. Convolutional Neural Network Architecture Based on FPGA with Reduced Requirements for Parameters.
- Kamel Abdelouahab, Maxime Pelcat, Francois Berry, Jocelyn Serot. 2018. Accelerating CNN inference on FPGAs: A Survey.
- Kiruki Cosmas, Asami kenichi. 2020. Utilization of FPGA for Onboard Inference of Landmark Localization in CNN-Based Spacecraft Pose Estimation.
- Stylianios I. Venieris, Alexandros Kouris, Christos-Savvas Bouganis. 2018. Toolflows for Mapping Convolutional Neural Networks on FPGAs: A Survey and Future Directions.
- Farhad Fallah. 2019. How to Develop High-Performance Deep Neural Network Object Detection/Recognition Applications for FPGA-based Edge Devices.

Colour Contrast Analyser for Colour Blind Assessment

(Pembangunan Aplikasi Penilaian Kekurangan Penglihatan Warna)

Harhiviin a/l Ganesan, Kalaivani Chellapan

Department of Electrical, Electronic and Systems Engineering,
Faculty of Engineering & Built Environment, Universiti Kebangsaan Malaysia, Malaysia

*Corresponding author: a163774@siswa.ukm.edu.my

ABSTRACT

Colour Vision Deficiency refers to the inability to distinguish different dominant colours. It is an inherited defect that causes damage or functionality weakness in one or more of colour receptors in the eye. There are many of well-known traditional clinical tests for colour vision deficiency diagnosis. One of these tests are by using the Ishihara Plates. In this project a Colour Vision Deficiency Testing Application is being developed to help users to determine the exact type of colour blindness they are experiencing. The methodology of this study was conducted through Matlab software. This Application can be used in colour vision education for school students and their teachers and parents also has the feature of colour vision screening. This paper focuses on the different type of plates that are combined as specific pattern's which will help users to discover their exact type of colour blindness. This application can identify if the user has Red-Green Colour Deficiency, Protanopia, Deutanopia or Monochromacy. A total of 39 users, 19 females and 20 males took part in using the application and a survey was conducted to collect the level of satisfaction of users regarding the application. The survey results show a high level of user experience satisfaction among users. The purpose of this project is to develop an application that is able to provide a high user experience among users in ensuring high accuracy in the deficiency detection.

ABSTRAK

Kekurangan Penglihatan Warna merujuk kepada ketidakupayaan untuk membezakan warna dominan yang berbeza. Perkara ini adalah kekurangan yang diwarisi yang menyebabkan kerosakan atau kelemahan fungsi pada satu atau lebih reseptor warna. Terdapat beberapa ujian klinikal tradisional yang terkenal untuk diagnosis Kekurangan Penglihatan Warna. Salah satu ujian terkenal adalah dengan menggunakan Plat Ishihara. Dalam projek ini, Aplikasi Penilaian Kekurangan Penglihatan Warna telah dikembangkan untuk membantu pengguna menentukan jenis buta warna yang mereka alami. Metodologi kajian ini dilakukan melalui perisian Matlab. Aplikasi ini boleh digunakan dalam pendidikan penglihatan warna untuk pelajar sekolah dan guru serta ibu bapa mereka juga mempunyai ciri penyaringan penglihatan warna. Projek ini memberi tumpuan kepada pelbagai jenis plat yang digabungkan sebagai corak tertentu yang akan membantu pengguna mengetahui jenis buta warna yang tepat. Aplikasi ini dapat mengenal pasti sama ada pengguna mempunyai Kekurangan Penglihatan Warna Merah-Hijau, Protanopia, Deutanopia atau Monokromasi. Sebanyak 39 pengguna, 19 perempuan dan 20 lelaki telah mengambil bahagian dalam menggunakan aplikasi ini serta sebuah tinjauan dilakukan untuk mengumpulkan data mengenai tahap kepuasan pengguna terhadap aplikasi tersebut. Hasil tinjauan menunjukkan tahap kepuasan pengalaman pengguna yang tinggi dalam kalangan pengguna. Tujuan projek ini adalah untuk mengembangkan aplikasi yang dapat memberikan pengalaman pengguna yang tinggi dalam kalangan pengguna bagi memastikan ketepatan tinggi dalam pengesanan Kekurangan Penglihatan Warna.

Keywords: Colour Contrast Analyser; Colour Blind Assessment; Ishihara Plates; Red-Green Colour Deficiency; Protanopia; Deutanopia; Monochromacy; Matlab; Application

INTRODUCTION

Colour vision deficiency refers to the inability of a person to distinguish between dominant colours. According to a biological interpretation, visual perception of colour is a process in which electromagnetic rays within a certain wavelength distance are absorbed by the retina of the eye thus converting it into an electrical signal, and then carried to the brain through the optic nerve (Gambino, O. et al. 2016).

Colour blindness is more common in males since X chromosomes carry the genes responsible for most common and inherited colour vision disorders and males have only one X chromosomes. In females, a functional gene on one of the two chromosomes is sufficient to compensate for loss on the other (Poret, S., Dony, R. D. & Gregori, S. 2009). About 8% of men and less than 1% of women have colour vision deficiency since birth (Ananto, B. S., Sari, R. F. & Harwahu, R. 2011). Colour vision deficiency can be categorized light, moderate or serious. About 40% of students with lack of colour vision leave secondary school and are unaware that they are experiencing colour blindness (Harwahu, R. et al. 2013).

There are various factors that cause a lack of colour vision. Most individuals who suffer from colour vision problems are due to genetics or inherited from their mothers. In addition, individuals can also become colour blind due to other diseases such as diabetes, multiple sclerosis or they get this disease over time due to the aging process. Most people who have colour vision problems can see clearly like other people however, they are not able to see red, green or blue light completely. It is very rare to find cases where an individual person is totally colour blind.

There are several types of colour vision deficiency. Among the types of colour vision deficiencies are Trichromacy, Red-Green deficiency, Dichromacy (Protanopia & Deutanopia) and Monochromacy. Most people experience Trichromacy vision which is also known as normal colour vision.

Red-Green colour blindness is one of the most common forms of hereditary Colour Vision Deficiency, characterized by complete loss or limited functionality of red cone and green cone photo pigment. It is a mild condition and does not hinder daily activities. Protanopia, a rare type of colour vision condition in which long wavelength receptors or known as L-cones did not form completely in the eye. In this, case, an individual person will have difficulty in identifying black, red, green, yellow and orange (Huang, J. et.al. 2009). Besides, an individual experiences Deutanopia when the medium wavelength receptors or known as M cones do not function. In this case, one cannot see

the green and magenta colours (Semary, N. A. & Marey, H. M. 2014). This colour vision deficiency is the most common. Monochromacy is the total inability to perceive colour. This type of colour blindness makes one see the world in shades of grey. Only a handful of humans who cannot see color directly (Ananto, B. S., Sari, R. F. & Harwahu, R. 2011). It is very rare and is called monochromatic vision.

Many methods have been proposed to help individuals to determine whether they are experiencing colour blindness. The most basic and common test would be the Ishihara test. The test is named after Shinobu Ishihara, a professor at the University of Tokyo, who first published the test in 1917 (Ishihara, S. 1917). The test consists of several coloured plates referred to as Ishihara plates where each plate contains a circle of dots that appears randomly in colour and size (Kindel & Eric 2013). In this paper Ishihara test is used as the main source together with the developed application. The full Ishihara test consists of 38 plates.

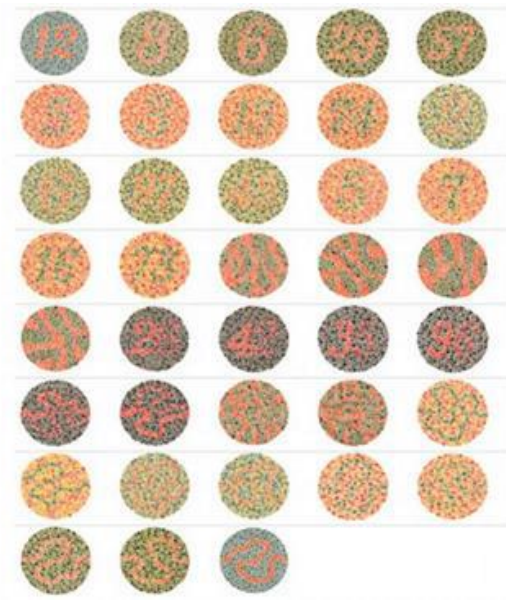


FIGURE 1. All 38 Ishihara Test Plates

The first plate shown in the Ishihara test is called the Introduction Plate. The second plate till the 9th plate is known as the Transformation Plate. The 10th till the 17th plate are known as the Vanishing Plates. The 18th plate till the 21st plate is known as the Hidden Digit Plates. The 22nd till the 27th plate is known as the Classification Plates. Last but not least, 28th plate till the 38th plate contains lines (Laskowski, M. 2012). Plates that only carry lines are for individuals who are not good at reading numbers, they will track the lines contained in the plates from end to end using indicators. Moreover, these plates are most likely not used all the time. For this study, only plates containing numbers were used

to produce the colour vision assessment application. This is because plates that have lines are not suitable to use in the application because they cannot take advantage of the actual functionality. Each Ishihara test plate has a real function that many do not understand. From the studies that have been done, the Ishihara plates can determine the exact type of colour vision deficiency of a person precisely that many people do not realise. In the methodology of this study, it describes the actual function of Ishihara plates, the main reason Ishihara Plates were chosen and as well as how Ishihara Plates were divided into several main groups of pattern to benefit the main purpose of this study.

Among the problem statements of this study are individuals with colour vision problems will face problems in daily life, such as difficulty distinguishing the colour of clothing, signal lights, and certain symbols. People with poor colour vision often live many years without realizing that they have such deficiencies (Lee, J. & Dos Santos, W. P. 2010). In some cases, lack of colour vision can be an obstacle for individuals to pursue education or careers in certain fields if they are not detected since childhood (Harwahu, R. et al. 2013). This becomes even more serious if individuals do not know the exact type of colour vision problems they are experiencing. Thus, early tests of colour vision deficiency are essential to support individuals with this deficiency problem since the early phases of their lives (Gambino, O. et al. 2016).

The main objective of this study is to develop an application for colour vision deficiency assessment with the development of a computerised diagnosis system based on the existing manual evaluation process, traditional testing and online assessment tests. Based on the problems discussed, the main objectives of this study are as follows:

- a) Develop an application that is easy to use, exciting, and robust.
- b) Develop an application that can determine the exact type of colour vision deficiency.

METHODOLOGY

There are several steps followed to complete this study and to develop the proposed application. In the first stage, a visibility study on the Ishihara Test and Plates was conducted. The visibility study will be conducted by studying each plate contained in Ishihara test. Only several plates were chosen to conduct this study and to combine it together with the application. This step also includes planning on arranging the chosen plates in several groups of patterns. Then, the process of developing the application based on the ideation. After that, empathy method was used by conducting a survey on the satisfaction of users regarding the application

which will be discussed more at the end of this study. Lastly, improvements and modification will be done to fulfil people's expectations.

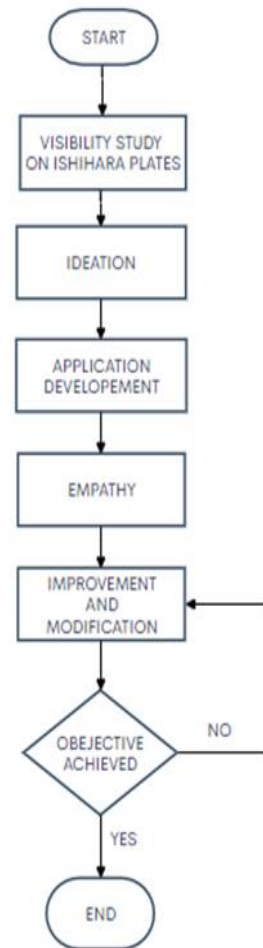


FIGURE 2. Flowchart of research method

Visibility Study of Ishihara Plates and Pattern Selection

In this study, 12 plates from the Ishihara test were selected and divided into three groups of patterns. This is done because each group has a specific reason which will be further explained. All Ishihara test plates are not required to determine the exact type of colour vision deficiency of a person. Therefore, this new technique was introduced in this study to further facilitate the process of determining the exact type of colour vision deficiency of a person.

As we know, the first plate (no. 12) shown in the Ishihara test is called the Introduction Plate. This plate is a compulsory plate to be chosen (Semary, N. A. & Marey, H.M. 2014). So in this study, this plate was made as the first pattern as shown in Figure 3. The main purpose of this plate is to test whether a user has prior colour vision. If a user

is unable to answer or detect the number on the first plate, the user is experiencing Monochromacy colour vision deficiency.

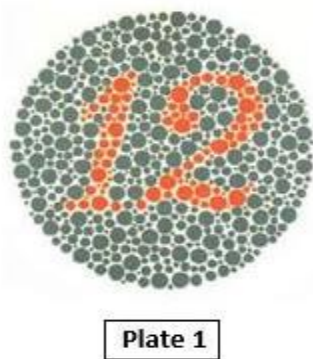


FIGURE 3. Pattern 1 of the Colour Contrast Analyser Application

As for the second group of pattern, only eight plates were selected from the 2nd plate till the 9th plate as shown in Figure 4, which is called the Transformation Plate of the Ishihara test and the 10th to the 17th plate which is called as the Disappearing Plates (Semary, N. A. & Marey, H.M. 2014). The purpose of this plates selection were because a user with normal colour vision will be able to accurately detect all these plates, but a person who suffers from red-green vision deficiency will have difficulty detecting it.

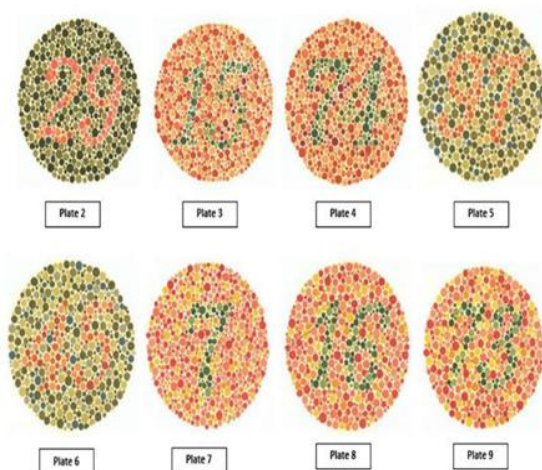


FIGURE 4. Pattern 2 of the Colour Contrast Analyser Application

As for the third group of patterns, three plates from the 22nd plate to the 27th plate of the Ishihara test called the Classification Plate are selected as shown in Figure 5. The purpose in selecting these plates because it helps to determine if

a person is suffering from a type of vision deficiency known as Protan (difficulty in seeing red colour). As for users who experience this situation, they can only see the number on the right side of the plate, whereas a person experiences Deutan will only be able to see the number on the left side of the plate (Semary, N. A. & Marey, H.M. 2014). The selection of these plates will provide an opportunity to further determine the two types of colour vision deficiencies known as Protanopia and Deutanopia.

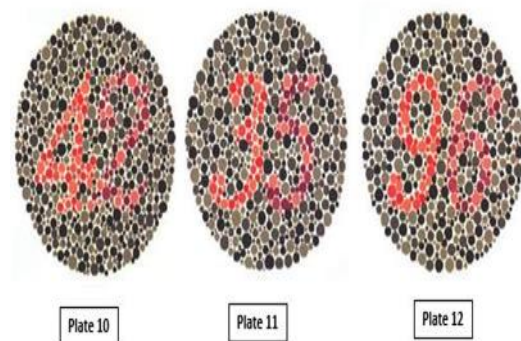


FIGURE 5. Pattern 3 of the Colour Contrast Analyser Application

In overall, from this study we can conclude that all Ishihara plates do not need to be used to know the exact type of colour vision deficiency of a person. Some important plates are sufficient enough to determine the exact type of colour vision deficiency. For this study, only 12 plates were selected in total to be tested through the developed applications. The application being developed in this study using Ishihara plates as the main source will be able to determine each type of colour vision deficiency accurately of a person. Among the type of colour vision deficiency of a person that this application will determine are Monochromacy, Red-Green deficiency, Protanopia and Deutanopia. This is the main objective that distinguishes this study from other studies which uses almost the same concept.

Application Development and User Data Capturing

The application's interface was developed through App Designer Matlab software (Matlab 2021a). App Designer integrates the two primary tasks of app building, laying out the visual components of a graphical user interface (GUI) and programming app behaviour. App designer helps to develop the code and also allows to modify the code accordingly that satisfy the use of the application which is being

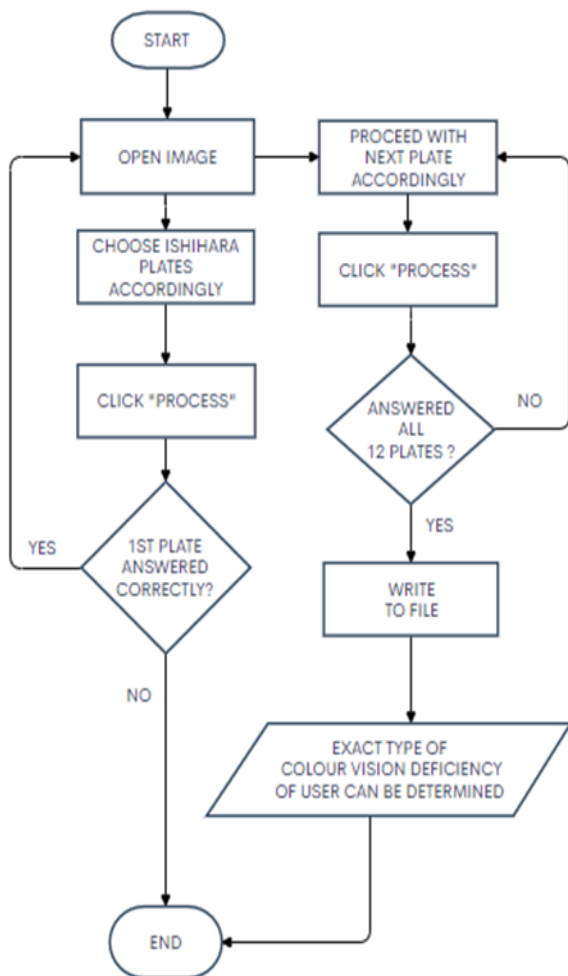


FIGURE 6. Flowchart on the operation of the Application's Interface accordingly

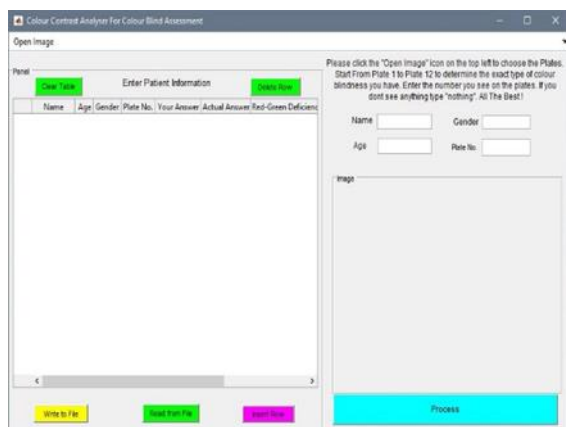


FIGURE 7. Colour Contrast Analyser Application Interface

This application allows users to test their colour vision which will be using the chosen plates from the Ishihara Test. To go through this test, users have to hit the "Open Image" icon present at the top left corner of the application's interface as shown in Figure 6.

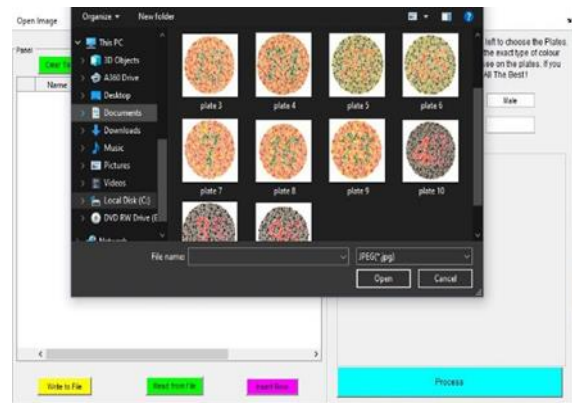


FIGURE 8. Snapshot of folder containing all 12 Plates

Following this, a folder containing all 12 will pop up as shown in Figure 7. This step enables users to start the test by choosing the 1st Plate to the 12th Plate accordingly one by one. The application expects users to fill in the number that he or she observe. The user is also required to answer all 12 Plates from the folder in order to know the exact type of colour vision deficiency he or she is experiencing. Furthermore, as the user answer each plate, the application automatically updates the users results into a table as shown in Figure 9.

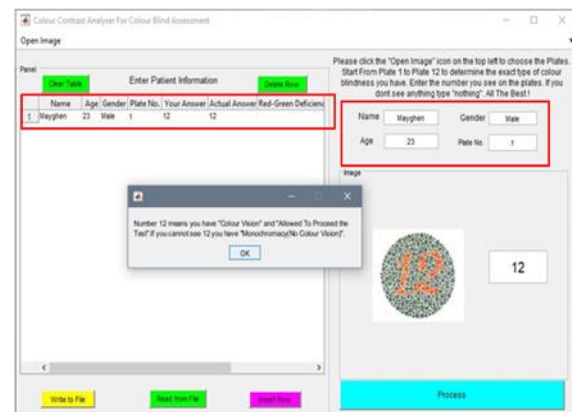


FIGURE 9. Snapshot of users result automatically generated into a table

Users have to insert their details such as their Name, Age, and Gender. Furthermore, a screen will pop up indicating whether the user have answered the right answer. As the user answers each plate a pop up screen will indicate whether the person has a normal view or any type of colour vision deficiency

Wrong answer will indicate the user what type of colour vision deficiency he or she is experiencing accordingly to each plate they answer.

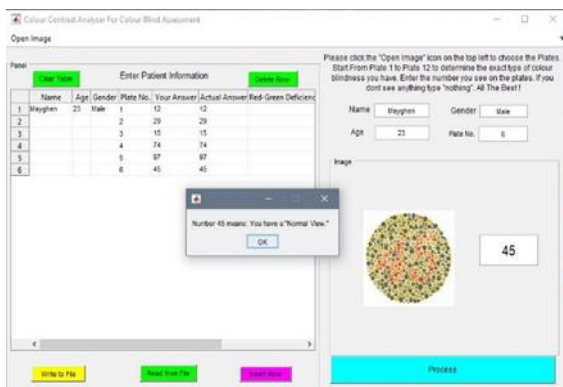


FIGURE 10. Snapshot of pop up screen indicating user has “Normal View” (Pattern 1)

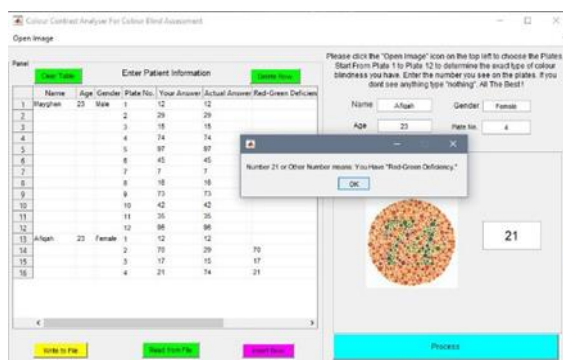


FIGURE 11. Snapshot of pop up screen indicating user experiencing “Red Green Deficiency”

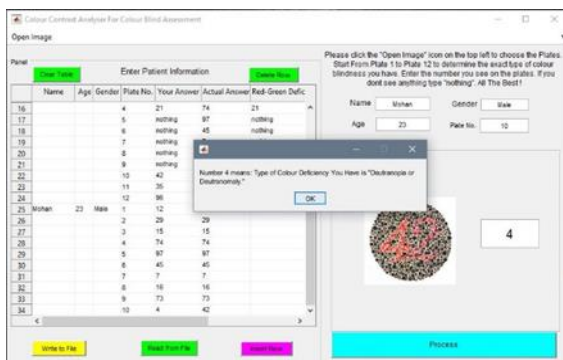


FIGURE 12. Snapshot of pop up screen indicating user experiencing “Deutanopia”

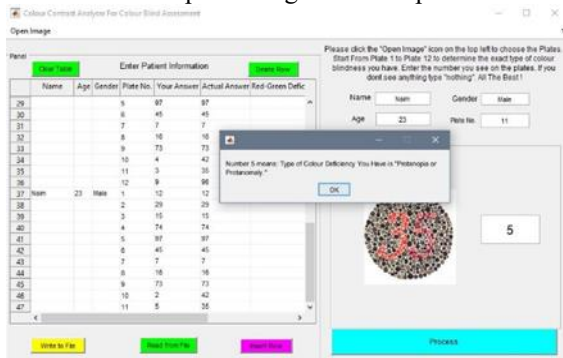


FIGURE 13. Snapshot of pop up screen indicating user experiencing “Protanopia”

RESULT AND DISCUSSION

Design Results and Link Up with Data Recording

Upon completion, users can upload their result into the computer system by hitting the “Write to File” button present at the bottom left corner of the application’s interface as shown in Figure 10.

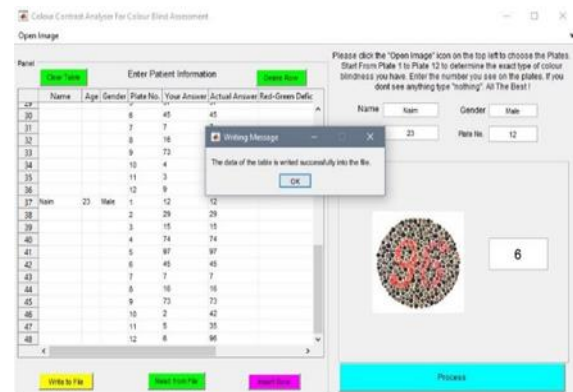


FIGURE 14. Snapshot of app interface and pop up screen indicating results uploaded successfully into the system

This way helps the users to view their result after completion of the test using the application. From the table developed by the application, users can determine their exact type of colour vision deficiency.

Name	Age	Gender	Plate No.	Your Answer	Actual Answer	Red-Green Deficiency	Protanopia (CVD)	Deutanopia (CVD)
Mayghen	23	Male	1	12	12			
			2	29	29			
			3	15	15			
			4	74	74			
			5	97	97			
			6	45	45			
			7	7	7			
			8	16	16			
			9	73	73			
			10	42	42			
			11	35	35			
			12	96	96			
Afiqah	23	Female	1	12	12			
			2	70	29	70		
			3	17	15	17		
			4	21	74	21		
			5	nothing	97	nothing		
			6	nothing	45	nothing		
			7	nothing	7	nothing		
			8	nothing	16	nothing		
			9	nothing	73	nothing		
			10	42	42			
			11	35	35			
			12	96	96			

FIGURE 15. User response generated from the application (Normal View and Red-Green Deficiency)

From Figure 15 shows two example results of users. We can observe that from the generated table above, the application managed to determine whether the user has a “Normal View” of colours (Mayghen) or experiencing “Red-Green Deficiency” (Afiqah). From the results obtained by user Afiqah, it proves that Transformation Plates, from the 2nd plate till the 9th plate which were chosen to be the

second pattern in this study helps to determine the exact type of colour vision deficiency. Not only that, the application developed in this study successfully generated the table automatically which turns out to be an accurate result.

Name	Age	Gender	Plate No.	Your Answer	Actual Answer	Red-Green Deficiency	Protanopia (CVD)	Deutanopia (CVD)
Mohan	23	Male	1	12	12			
			2	29	29			
			3	15	15			
			4	74	74			
			5	97	97			
			6	45	45			
			7	7	7			
			8	16	16			
			9	73	73			
			10	4	42			4
			11	3	35			3
			12	9	96			9
Naim	23	Male	1	12	12			
			2	29	29			
			3	15	15			
			4	74	74			
			5	97	97			
			6	45	45			
			7	7	7			
			8	16	16			
			9	73	73			
			10	2	42			2
			11	5	35			5
			12	6	96			6

FIGURE 16. User response generated from the application (Deutanopia and Protanopia)

As we can see for the other two types of colour vision deficiency left, the application managed to generate an accurate result. We can observe that from the generated table above, the application managed to determine whether the user has experiences “Deutanopia” (Mohan) or experiences “Protanopia” (Naim). From the results obtained by user Mohan and Naim it proves that Classification Plates, from the 10th plate till the 12th plate which were chosen to be the third pattern in this study helps to determine the exact type of colour vision deficiency. Not only that, it is also proven that if a user managed to only see the number on the right of the plate he or she experiences Deutanopia (Mohan), whereas if a user managed to only see the number on the left of the plate he or she experiences Protanopia (Naim).

If a user is experiencing any type of colour vision deficiency, he or she can use this result to seek help and guidance from an expert eye doctor or else an ophthalmologist. In this case, the experts will definitely get a clearer picture of the deficiency problem the experts guidance will definitely help in reducing the problems faced due to colour vision deficiency faced by the individual in their daily live.

Statistical Analysis on Users Satisfaction Regarding Developed Application

A survey was carried out to do a statistical analysis on how the users preferred the application. This survey was filled by 39 users, 19 female and 20 male users who took the colour blind test through the developed application in this study. The 39 users were among age groups and race. The main purpose of this survey was to collect data on the satisfaction of users regarding the test carried through the developed application.

The survey was divided into three sections. Section A was on user satisfaction regarding the Application’s Interface. Section B was about user satisfaction on the Assessment Method done through the developed application. Section C was on the Result Satisfaction obtained by each user.

Each section consists of five questions respectively. Users level of satisfaction was collected in a way where users have to choose among Strongly Disagree, Disagree, Neutral, Agree or Strongly Agree for each questions in the respective sections.

Section A (Assessment on the application's Interface) / (Penilaian Antaramuka Aplikasi)

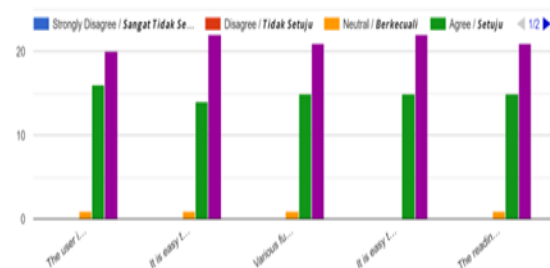


FIGURE 17. Section A (User Satisfaction on Application’s Interface)

Section B (Assessment Method) / (Kaedah Penilaian)

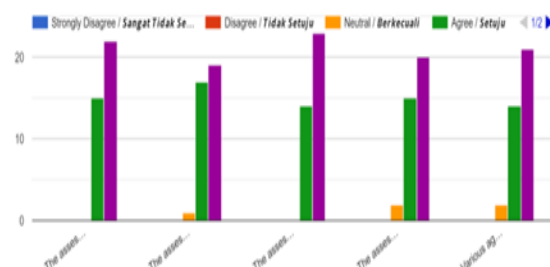


FIGURE 18. Section B (User Satisfaction on Assessment Method)

Section C (Result Satisfaction) / (Kajian kepuasan hasil responden)

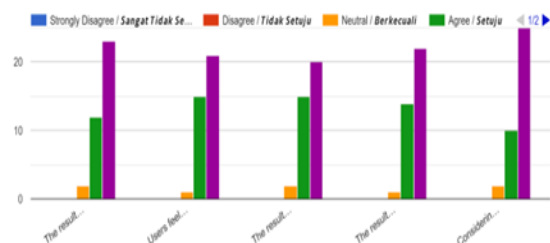


FIGURE 19. Section C (User Satisfaction on the Obtained Results)

Overall, from the statistical analysis done most of the users have chosen the option “Agree” and “Strongly Agree” for the questions asked in each section. Therefore, we can come to a conclusion that most of the users who took the test through the developed application in this study were really satisfied with the application’s interface, the assessment method through the application and the final result obtained. Not only that, the questions asked in the survey was really satisfied with the application’s interface, the assessment method through the application and the final result obtained. Not only that, the questions asked in the survey was also another way to find out whether the objectives of this study have been achieved. Both objective proposed in this study have been achieved successfully.

CONCLUSION AND FUTURE WORK

In a nutshell, all proposed objectives of this study have been successfully achieved. An application that is easy to use, exciting, and robust have been developed. Moreover, an application that can determine the exact type of colour vision deficiency of a person have also been developed.

Besides, there are certain limitations that this study can improve in the future. Among the limitations are this study only focuses on Ishihara Test as the main source. Other than that, this study is developed and also focuses on a single language. In this case, some users might find it hard to read and understand the terms and words used in the development of the application.

Therefore, the improvement that can be made to this study is that the application can be developed using more than one language. For example, the application can be developed with more than one language as English, Malay, Chinese and Tamil. This improvement will give an advantage to the users to choose their preferable language to answer the test using the developed application in this study. Moreover, another improvement that can be taken into consideration is to study and analyse more on other colour vision deficiency test and combine them together with the application in order to develop the perfect colour vision deficiency application that can determine the exact type of colour blindness of an individual.

ACKNOWLEDGEMENT

The author would like to thank Dr Kalaivani Chellapan for providing an opportunity to explore the field of colour vision and the types of colour vision deficiencies. The advice and guidance that has been given is greatly appreciated.

REFERENCE

- Ananto, B. S., Sari, R. F., & Harwahu, R. 2011. Color Transformation for Color Blind Compensation on Augmented Reality System. International Conference on User Science and Engineering (i-USER). hlm. 129-134. Shah Alam, Selangor.
- Gambino, O., Minafo, E., Pirrone, R. & Ardizzone, E. 2016. A Tunable Digital Ishihara Plate for Pre-School Aged Children. 38th Annual International Conference of the IEEE Engineering in Medicine and Biology Society (EMBC). hlm. 5628-5631. Orlando, Florida.
- Harwahu, R. 2013. Implementation of Color-Blind Aid System. Journal of Computer Science. 9(6): 794–810.
- Huang, J., Chen, C., Jen, T. & Wang, S. 2019. Image Re-Colorization for the Color Blind. International Conference on Acoustics, Speech and Signal Processing, hlm. 1161-1164.
- Ishihara, S. 1917. Tests for Color-Blindness. Tokyo, Japan.
- Lee, J. & Dos Santos, W. P. 2010. Fuzzy-Based Simulation of Real Color Blindness. Annual International Conference of the IEEE Engineering in Medicine and Biology. hlm. 6607-6610. Buenos Aires.
- Laskowski, M. 2012. Using Customized Pseudoisochromatic Plates for Detecting Chosen Forms of Dichromacy. Journal of KONES Powertrain and Transport. Vol 19, No. 1. Lublin, Poland.
- MATLAB. 2021a. Version 8. Massachusetts: Math Work Inc.
- Poret, S., Dony, R. D. & Gregori, S. 2009. Image Processing for Colour Blindness Correction. 2009 IEEE Toronto International Conference Science and Technology for Humanity (TIC-STH). hlm. 539-544. Toronto, Ontario.
- Semary, N. A. & Marey, H. M. 2014. An Evaluation of Computer Based Color Vision Deficiency Test: Egypt as a Study Case. International Conference on Engineering and Technology (ICET) hlm. 1-7. Cairo.

Design of Portable Biosensor Reader for Leptospira Detection

(Reka Bentuk Pembaca Biosensor Mudah alih untuk Pengesanan Leptospira)

Kaliswaran a/l Ganesan, Noorfazila Kamal*, Huda Abdullah

Department of Electrical, Electronic and Systems Engineering
Faculty of Engineering & Built Environment, Universiti Kebangsaan Malaysia, Malaysia

*Corresponding author: fazila@ukm.edu.my

ABSTRACT

Leptospirosis is a chronic disease caused by leptospira bacteria that affects risk groups exposed to animal waste reservoirs or contaminated environments. It will cause several health complications such as kidney failure, jaundice, and internal bleeding to humans. Leptospirosis has emerged as a health threat in a new state due to the influence of globalization and climate. The cause of leptospira infection will only be investigated after a case is confirmed or death from leptospirosis. Currently available techniques for leptospira detection are largely limited to the laboratory and require large and expensive instruments to perform the analysis. Therefore, to overcome this problem, this study designed a portable biosensor reader that uses potentiostats for on-site leptospira detection. This biosensor reader uses a linear sweep voltammetry electroanalytic method for detection. This project is divided into two phases which is designing a portable voltammetric potentiostat and designing an on-site leptospira detection system. In the first phase, a voltammetric potentiostat was designed using Proteus Design Suite software. The potentiostat is designed using a microcontroller as a voltage supplier and a current reader, then the operational amplifier circuit operates as a voltage and current transfer to the electrode. On the part of the leptospira detection system, the microcontroller is programmed to detect the presence of leptospira based on the specifications of the PANI-Fe-Al biosensor. LCD board and an application specially developed for displaying the results of the detection system. The results of this study show that the designed potentiostat can run smoothly and the detection system can detect the presence of leptospira according to the required specifications.

Keywords: *Leptospira; Potentiostat; Linear sweep voltammetry; PANI-Fe-Al*

ABSTRAK

Leptospirosis merupakan penyakit kronik yang disebabkan oleh bakteria leptospira yang mempengaruhi kumpulan risiko yang terdedah kepada takungan sisa haiwan atau persekitaran yang tercemar. Ia akan menyebabkan beberapa komplikasi kesihatan seperti kegagalan buah pinggang, penyakit kuning dan pendarahan dalaman kepada manusia. Leptospirosis telah muncul sebagai ancaman kesihatan dalam keadaan baru kerana pengaruh globalisasi dan iklim. Punca jangkitan leptospira hanya akan disiasat setelah kes disahkan atau meninggal dunia akibat leptospirosis. Teknik yang ada pada masa ini untuk pengesanan leptospira sebahagian besarnya terbatas pada makmal dan memerlukan instrumen yang besar dan mahal untuk melaksanakan analisis. Oleh itu bagi mengatasi masalah ini, kajian ini mereka bentuk pembaca biosensor mudah alih yang menggunakan potensiostat untuk pengesanan leptospira di lapangan. Pembaca biosensor ini menggunakan kaedah elektroanalitik voltammetri sapuan linear untuk pengesanan. Projek ini dibahagikan kepada dua fasa iaitu mereka bentuk potensiostat voltammetrik mudah alih dan mereka bentuk sistem pengesanan leptospira di lapangan. Dalam fasa pertama, potensiostat voltammetrik direkabentuk dengan menggunakan perisian Proteus Design Suite. Potensiostat ini direkabentuk dengan menggunakan mikropengawal sebagai pembekal voltan dan pembaca arus, lalu litar penguat operasi sebagai pemindah voltan dan arus ke elektrod. Pada bahagian sistem pengesanan leptospira pula, mikropengawal diaturcara supaya dapat mengesan kehadiran leptospira berdasarkan spesifikasi biosensor PANI-Fe-Al. Papan LCD dan sebuah aplikasidibangunkan khas untuk paparan hasil keputusan sistem pengesanan. Hasil kajian ini menunjukkan, potensiostatyang direkabentuk dapat berjalan lancar dan sistem pengesanan dapat mengesan kehadiran leptospira mengikut spesifikasi yang diperlukan.

Kata Kunci: *Leptospira; Potensiostat; Voltammetri sapuan linear; PANI-Fe-Al*

INTRODUCTION

The pathogenic *Leptospira* bacteria causes leptospirosis, a widespread zoonotic illness (Nagraik et al., 2019). It is one of the most serious human health issues. The pathogenic strain *Leptospira interrogans* and the nonpathogenic strain or saprophyte *Leptospira biflexa* are the two primary species of *Leptospira* (Adler & de la Peña Moctezuma, 2010). Risk groups exposed to animal waste reservoirs or contaminated surroundings, such as slaughterhouses, sewage employees, military personnel, and people who participate in water sports and enjoyment, are all susceptible to leptospirosis (Costa et al., 2015). In subtropical countries, high tropical humidity and mild temperatures are excellent for *Leptospira* to thrive for lengthy periods of time in the environment (Benacer et al., 2013).

Humans are usually infected with *Leptospira* pathogenic infections after coming into contact with polluted water or soil from diseased animals' urine. It will create several health problems, including kidney failure, jaundice, and internal bleeding, all of which will raise the death rate over time. Controlling zoonotic illnesses, which are diseases passed from animals to humans, has received a lot of attention around the world to date (Jampasa et al., 2019). Due to the influence of globalization and climate change, leptospirosis has become a new health issue (Costa et al., 2015).

The presence of leptospira requires laboratory diagnosis employing fluorescent markers to culture bacteria from blood, urine, and tissues. Standard methods for detecting certain bacteria, such as polymerase chain reaction (PCR), for use on urine and blood samples include microscopic agglutination test (MAT) and enzyme-linked immunosorbent assay (ELISA) (Azizi et al., 2014; Vasconcellos et al., 2010). Several approaches can be used to identify leptospira in water, including hybridization probes in Deoxyribonucleic acid (DNA) and Ribonucleic acid (RNA), but this detection method is enhanced since it has a time limit and sensitivity.

After a case of leptospirosis is confirmed or a death due to leptospirosis occurs, the cause of infection will be explored. Preventive interventions are complicated by the lack of a portable leptospira detection system that may be utilized on-site. The existing procedures are mostly limited to laboratory detection, which takes longer and necessitates the use of large, expensive tools to implement advanced analytical systems.

The thin film sensor as shown in Figure 1 works through a biochemical reaction between the thin surface and the content sample, especially bacteria, to describe several accurately measurable electrical values or signals. This response will

introduce certain variations in the value of the detected signal. Electrochemical impedance (EIS) and current voltage ($I - V$) spectroscopic measurements were used to confirm the sensitivity and efficacy of sensors with different concentrations of *Leptospira* bacteria (Jurait et al., 2018).

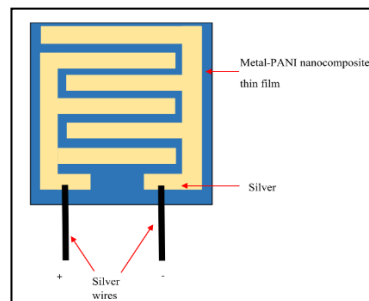


FIGURE 1: The design of comb- structured silver electrode PANI Fe-Al

As a result, this study designed a portable biosensor reader based on a microcontroller and a potentiostat for on-site leptospira detection. This potentiostat is a miniature potentiostat that can do precise potentiostatic measurements. The voltametric approach, voltage range (V), voltage change rate (V), current measurement range (I), resolution, and sampling rate of the potentiostat will vary depending on the intended device usage. There are many types of voltammetry procedures, such as "linear sweep," "square wave," "cycle voltammetry," and so on.

Identify a viable voltametric technique for leptospira detection, develop a compact voltametric potentiostat for on-site leptospira detection, and design a portable leptospira detection system are the three specific aims for this work. The goal of this study is to design a portable leptospira detection device based on a PANI-Fe-Al nanocomposite thin film sensor in the research (Jurait et al., 2018). The approach for determining the presence of leptospira is derived from oft study's findings in (Jurait et al., 2018).

It is important to detect these pathogens in the environment so that early prevention can be undertaken. This research will address few key techniques and components for design the portable biosensor reader.

Leptospira bacterial detection technique

Because of its high conductivity and ease of control, using a thin film of polyaniline nanocomposites (PANI-Fe-Al) to detect *Leptospira* can improve sensitivity. Because of its high conductivity, compatibility with biological molecules, environmental durability, and ease of synthesis of affordable monomers, polyaniline is a form of conductive polymer with a wide range of uses in

electrochemical biosensors (Thakur et al., 2015). The negative charge of the cell structure of *Leptospira* bacteria will create a reactivity with the thin film surface of PANI-Fe-Al nanocomposites. Spectroscopic measurements of electrochemical impedance (EIS) and current voltage (I-V) were conducted to confirm the sensitivity and effectiveness of these sensor in the research (Jurait et al., 2018). Figure 2 displays the findings of the sensor reaction for the concentration of *Leptospira* bacteria using a leptospira sample (108 CFU mL⁻¹). The current voltage curve (I - V) is obtained using a potentiostat.

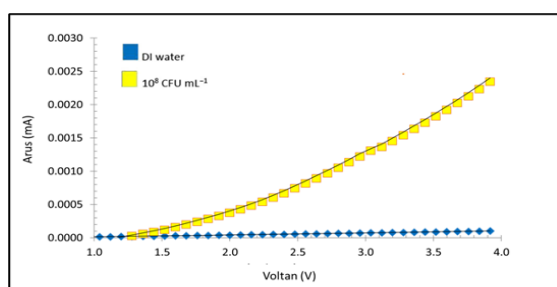


FIGURE 2: Measurement of (I-V) PANI-Fe0.8-Al0.2 thin film sensor nanocomposites

Voltammetry

Voltammetry experiments investigate an analyte's half-cell reactivity. For each voltage supplied, the voltammetry method takes a current reading. The voltage is progressively increased or decreased over time, with the exact current value being measured as a dependent variable. The current at a working electrode (WE) is measured when the voltage between the counter electrode (CE) and the reference electrode (RE) is swept linearly during a fixed time interval in linear sweep voltammetry (LSV). The scan rate is the voltage against time graph, and it can range from 1mV to 1,000,000 V/s. (Scholz, 2015).

Portable potentiostat

A portable potentiostat is a customized device that can make accurate potentiostatic measurements in a compact form while keeping the original potentiostat's definition. Several simple electronic components, such as resistors, capacitors, and operational amplifiers (op-amps), can be used to build a rudimentary potentiostat (Meloni et al., 2016). The operating amplifier controls the flow of current through the electrochemical cell through the response electrode (CE) and the working electrode (WE). Because it involves fewer production stages and allows for subsequent adjustments, a microcontroller-based potentiostat design, such as the Arduino, was chosen. Using pulse width modulation (PWM) pin control, Arduino circuit boards generate fixed voltage waveforms. At a

constant frequency, this voltage oscillates between high and low levels. It is possible to create voltage ramps at different scan rates for different electrochemical studies to perform cyclic voltammetry (CV), linear sweep voltammetry (LV), or Chronoamperometry by adjusting the PWM duty cycle.

Biosensor reader

Biosensor readers are made up of bio-receptors (enzymes/antibodies), transducer components (semiconductor materials/nanomaterials), and electronic systems (signal amplifiers, processors, and displays) (Kaur & Shorie, 2019). The operating amplifier (op-amp) of the biosensor reader is connected between the electrode and the probe channel. The biosensor reader examines the voltage and current changes at the electrode generated by the reaction between the electrode and the target substance in the electrochemical solution. A measurement module and an output module are included in the biosensor reader. The measurement module connects the probe channel to a fixed resistance reference resistor on the op-amp, measuring the reference voltage drop in the reference resistor and the channel voltage drop in the probe channel, and then analysing the change in probe channel voltage value from reference voltage drop and channel voltage drop. The output module outputs the results of the target material's analysis based on the voltage value change.

METHODOLOGY

The waterfall model utilised in the study approach is depicted in Figure 3. The purpose, objectives, and scope of the study for the *Leptospira* detection system were identified during the planning phase. During the analysis phase, a study of the existing *Leptospira* detection system was undertaken to determine the system's shortcomings and advantages. In addition, voltammetry and potentiostat creation approaches were investigated. The portable potentiostat design procedure and the design of a microcontroller based *Leptospira* detection system were then completed in the design phase. Finally, a testing phase of the designed *Leptospira* detection system will be performed.

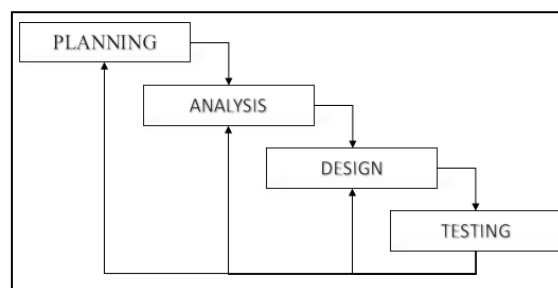


FIGURE 3: Waterfall model

Figure 4 shows the overall flow chart of the research methodology designed for this study. Initially, a planning and analysis process was performed to identify the voltammetry techniques used, and to study the portable potentiostats used in electrochemical studies. Next, based on the research done, a portable potentiostat based on an Arduino microcontroller was designed. Then, an Arduino microcontroller program was constructed to be able to supply voltage based on the results of the study (Jurait et al., 2018). Subsequently, automatic *Leptospira* detection programming based on voltage versus current graph data obtained from the study results (Jurait et al., 2018) was constructed. Finally, a smartphone app was developed to display *leptospira* detection results.

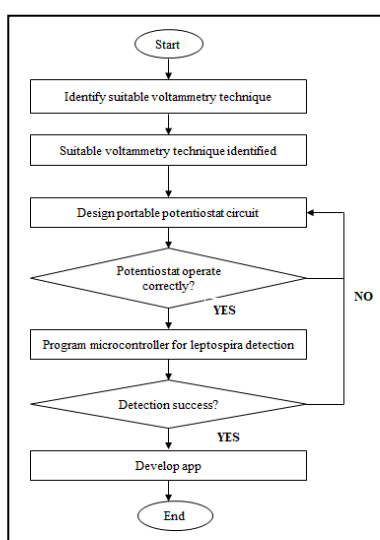


FIGURE 4: Flow chart of research methodology

Portable potentiostat design

Proteus Design Suite was used to design the portable potentiostat used in this study. This software was used to construct the potentiostat circuit as well as simulate the microcontroller with the circuit that was designed. The circuit has been designed in two stages to achieve the research's objective precisely. The supply of voltage to the counter electrode is the first stage. An active low pass filter converts a PWM digital signal to an analogue voltage, an inverting amplifier converts the analogue signal to an inverting analogue signal. The signal is then converted back to its original polarity and buffer output by a second inverting amplifier. The feedback component from the reference electrode via the voltage follower amplifier is included in this buffer

level. The input impedance of the reference

electrode is considerably increased by this feedback signal, which reduces reverse current flow.

The second stage is the current reading from the working electrode, which includes a transimpedance amplifier and a voltage follower that delivers the value of the received current to the microcontroller's ANALOG INPUT pin as a voltage. The portable potentiostat circuit designed in this study is shown in Figure 5. The Arduino Uno microcontroller board is used to control the voltage and collect data in this potentiostat design. The voltage supply circuit uses OP177A which is a single op-amp, and the current reading circuit uses LM324 which is a quad op-amp. The Arduino Uno board runs a program that allows performing linear sweep voltammetry for the detection of the presence of *leptospira*. In this circuit, contains an LCD board, an oscilloscope and a serial monitor to obtain the circuit results.

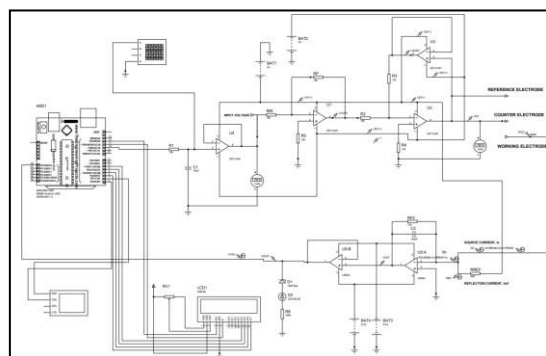


FIGURE 5: Portable potentiostat circuit

The Arduino Uno board transmits the signal in the form of pulse width modulation (PWM) and for linear voltammetry sweep experiments, this PWM signal is sent to the counter electrode for a redox reaction. Since the PWM signal is in digital form, it needs to be converted to analog form, for that purpose, an active low pass filter circuit is used. This circuit contains resistors, capacitors and voltage follower amplifiers. In this type of filter arrangement, the input signal (V_{IN}) is applied to a series combination (both Resistor and Capacitor) but the output signal (V_{OUT}) is only taken in through the capacitor. Equation below is to calculate the output voltage for a resistor (R) and a capacitor (C) connected in series. (f) is the frequency of the PWM signal transmitted from pin 10 of the Arduino which is 490Hz. The values of R and C , $R = 10K\Omega$ and $C = 10\mu F$.

$$V_{OUT} = V_{IN} \times \frac{X_C}{\sqrt{R^2 + X_C^2}} ; X_C = \frac{1}{\sqrt{2\pi f C}}$$

Figure 6 shows the active low pass filter used in the circuit.

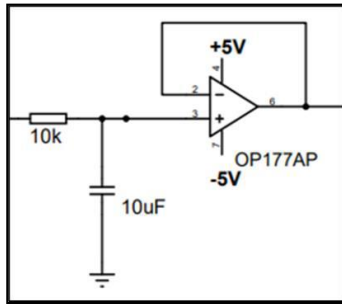


FIGURE 6: Active low pass filter

The inverting amplifier circuit utilised in this study's portable potentiostat circuit is shown in Figure 7. Open loop amplifier operation has a very high DC gain. To minimise and adjust the overall gain of the amplifier, connect an appropriate resistor across the amplifier from the output terminal back to the reverse input terminal. This produces and exerts a negative feedback effect, which results in a highly stable working amplifier-based system. The technique of giving a little portion of the output signal back to the input is known as negative feedback. The output signal must be linked to the negative terminal or the op-amp boost input through a feedback resistor called R_f to provide negative feedback. Because the inverting input terminal will be the sum of the input voltage plus the negative feedback voltage designated as the peak point, the signal will be different from the real input voltage. As a result, an input resistor must be used to separate the true input signal from the reverse input signal, R_{in} . The non-inverse positive input is connected to a compensation resistor to compensate for the input bias current between the two inputs in the op-amp. It works to make the voltage drop to zero.

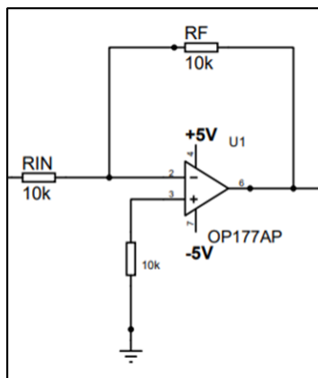


Figure 7: Inverting amplifier

A transimpedance amplifier is a current to voltage converter. The transimpedance amplifier circuit is a simple reverse amplifier with negative feedback. A feedback resistor is connected between the output

terminals inverting the amplifier as shown in Figure 8.

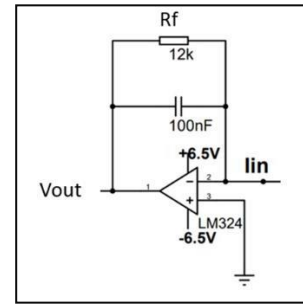


FIGURE 8: Transimpedance amplifier

The op-Amp input current will be zero due to its high input impedance. Therefore, the current from the current source must pass through the resistor (R_f) completely. The current from the current source is (I_{IN}). The output voltage (V_{OUT}) of the op-Amp can be calculated using equation below.

$$V_{OUT} = -I_{IN} \times R_f$$

The transimpedance amplifier circuit Figure 8 uses a generic low power amplifier LM324. Resistors and capacitors are connected to the feedback path. The LM324 amplifier is connected in a negative feedback configuration. The negative input pin is connected to the resistor and the feedback capacitor, the positive pin is connected to earth.

Leptospira Detection System

To design an effective Leptospira detection system, the microcontroller connected to the potentiostat must be programmed to run smoothly after the circuit is designed. As shown in Figure 9, the first level of programming is to digitally supply voltage to the potentiostat via PWM, the second is Leptospira detection programming, and the third is to develop a smartphone app as a display screen displaying current values from leptospira reactions with biosensor, as well as detection results.

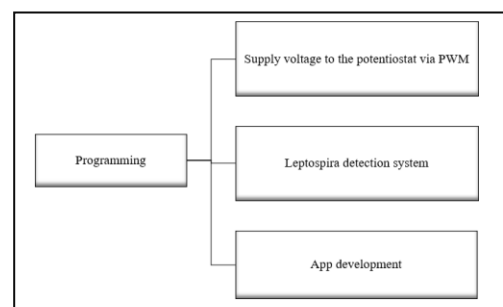


FIGURE 9: Programming

The Arduino Uno microcontroller's PWM voltage is 5V, while the DAC can deliver voltages between 0 and 5V. As a result, to supply the voltage, the Arduino uno must be programmed using the PWM table. The detection system in this study should be supplied with a voltage range of 1.0V to 4.0V with a 0.5V step. The truth tables for the PWM-based DAC utilized in this work to supply the voltage are listed in Table 1.

Table 1: DAC Truth Table

Voltage (V)	PWM level
1.0	51
1.5	76.5
2.0	102
2.5	127.5
3.0	153
3.5	178.5
4.0	204

The comparison program is an important element in the leptospira detection system. Figure 10 shows the flow chart developed for Arduino uno programming to complement this system. Initially, the current data obtained from the graph shown as in Figure 2 will be recorded into the Arduino uno. In this study, a comparison of the current values that determined the presence of leptospira bacteria was performed with a range of $\pm 20\%$ margin as shown in Table 2.

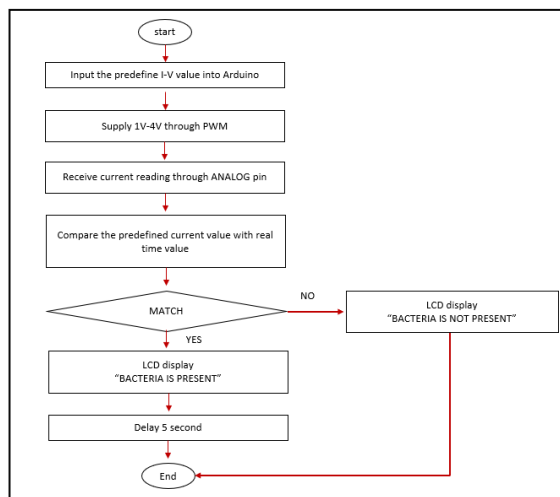


FIGURE 10: Flow chart of Leptospira detection system

Table 2: list of leptospira detection current values by range $\pm 20\%$ margin

Voltage (V)	INPUT - 0.2*INPUT (min) (mA)	INPUT (mA)	INPUT + 0.2*INPUT (max) (mA)
1.0	0.00	0.00	0.00
1.5	0.00016	0.0002	0.00024
2.0	0.00032	0.0004	0.00048
2.5	0.00064	0.0008	0.00096
3.0	0.00104	0.0013	0.00156
3.5	0.00152	0.0019	0.00228
4.0	0.002	0.0025	0.003

After that, the program to supply voltage with range 1.0V- 4.0V will be uploaded. The current values from the study results (Jurait et al., 2018) are supplied to the working electrodes of the potentiostat circuit as a simulation of the leptospira reaction with the biosensor. This current is sent to the Arduino analog input pin in the form of a voltage after passing through the transimpedance amplifier. After the Arduino receives the current value, it will compare the current value with the previously recorded current data. In this comparison, if the two data are matched, are within the set range, the LCD will display the sign "BACTERIA IS PRESENT", otherwise if the two data do not match, the LCD will display the sign "BACTERIA IS NOT PRESENT".

In addition to the LCD board, a prototype user interface was developed to display results from decision -making performed by the Arduino. The developed mobile applications are named as LEPTOSPIRA DETECTION-apps, which function to (1) display the current values of leptospira and biosensor reaction currents; (2) displays the decision made by the Arduino, namely "BACTERIA PRESENT" or "BACTERIA NOT PRESENT". By using "MIT App Inventor", the design process is divided into two phases, namely the design of the user interface using the Component Designer and the implementation of programming logic using the Block Editor. As shown in Figure 11, this developed application is coded to connect to the Arduino uno utilizing a Bluetooth module. An Arduino uno, an Arduino HC-05 Bluetooth module, and a smartphone are the components and equipment used in this system.

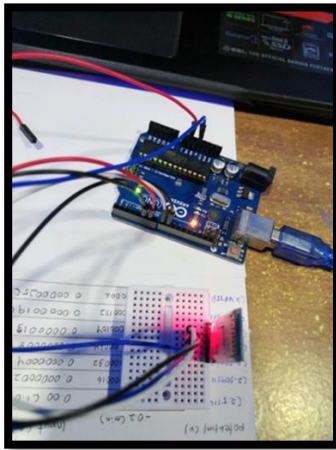


FIGURE 11: Arduino Bluetooth module used for connection to applications

Bluetooth protocol is used by the LEPTOSPIRA DETECTION-apps to communicate with the bluetooth, thus the user must know the Bluetooth name of the module and the connection state. Figure 12 depicts the connection flow chart for the Leptospira detection system using Bluetooth technology. Figure 13 shows the Component Designer, an Android application user interface screen created for this study's leptospira detection system.

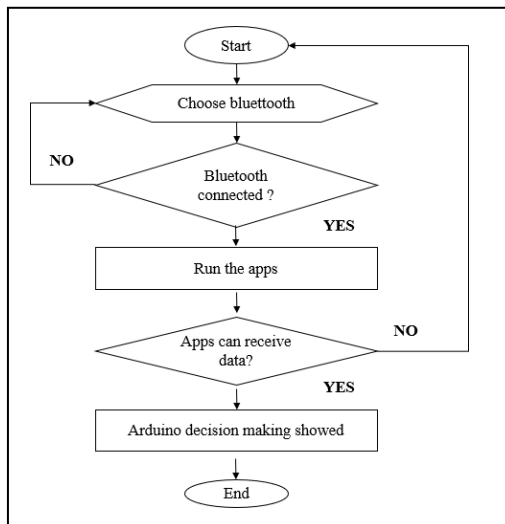


FIGURE 12: Flow chart of smartphone apps

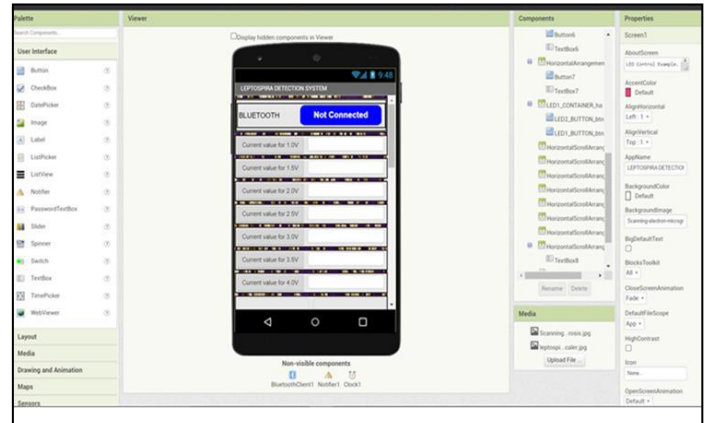


FIGURE 13: LEPTOSPIRA DETECTION-apps user interface screen

RESULTS AND DISCUSSION

Portable Potentiostat

The PWM signal is in digital form, it is converted to analog form with an RC filter. To configure the RC, the RC analysis tool is used as shown in Figure 14. Figure 15 shows the transient analysis graph for the voltage values of 1.0V, 1.5V, 2.0V, 2.5V, 3.0V, 3.5V and 4.0V, for the conversion response complete within 0.3 seconds. Figure 16 shows the results of the active low pass filter, analog voltage value is successfully converted from the PWM signal in the simulation.

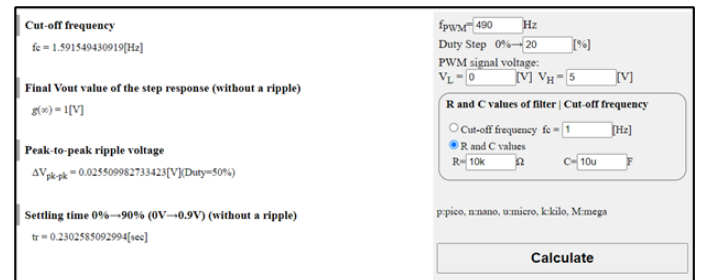


FIGURE 14: RC analysis tool

After the PWM signal is converted to an analog value, a voltage flows through two inverting amplifiers and subsequently to the counter electrode. Figure 17 shows the voltage supplied to the counter electrode in a circuit. It is found that the voltage at the counter electrode is equal to the output voltage of the active low pass filter.

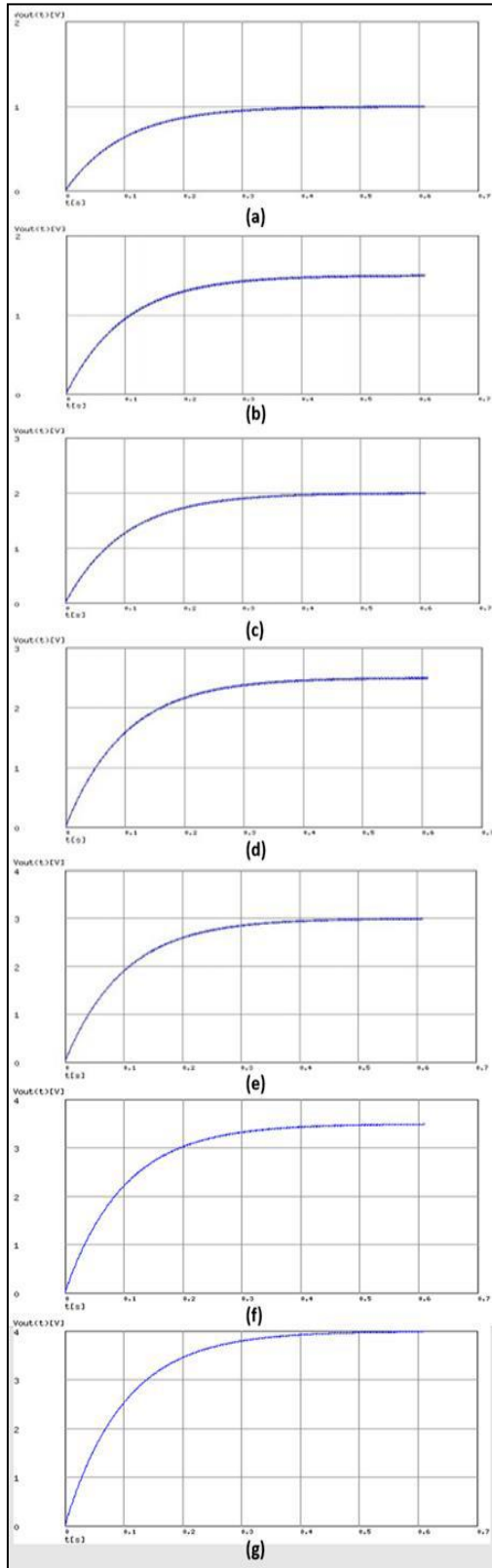


FIGURE 15: Transient analysis graph: (a) 1.0V (b) 1.5V (c) 2.0V (d) 2.5V (e) 3.0V (f) 3.5V (g) 4.0V

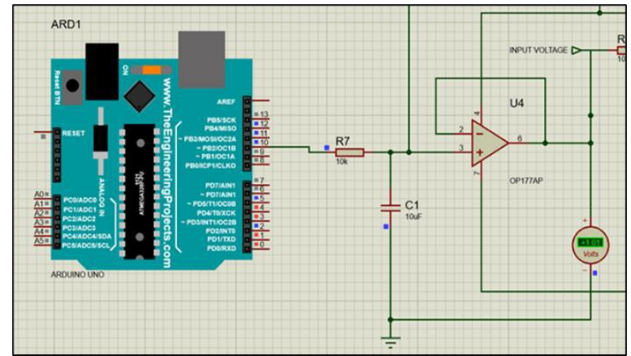


FIGURE 16: The results of the active low pass filter

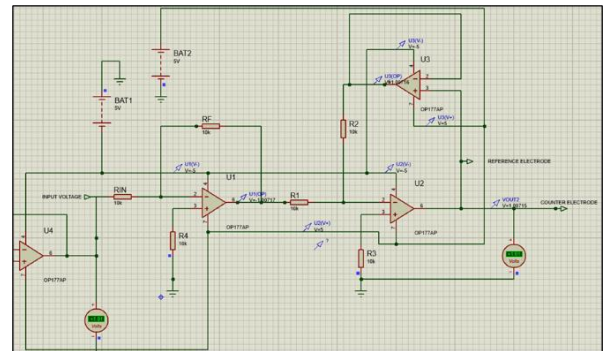


FIGURE 17: Voltage supplied to counter electrode

Figure 18 shows a current receiving circuit that receives a current value from a working electrode. In this simulation the current value is supplied with a DC current source and labeled as the source current, I_S . Because the value of the current received from the working electrode is too low in micro units, this current value cannot be converted to a voltage value that can be read by the ANALOG INPUT pin of the microcontroller. Therefore, the potentiostat of this study uses an additional resistor known as a reflection resistor. This resistor is supplied with (-5V) to obtain the reference current, I_{REF} . This I_{REF} value is added to the I_S value to produce the input current, I_{IN} . The I_{IN} value will enter the negative terminal of the transimpedance amplifier. This I_{IN} can be calculated by equation below.

$$I_{IN} = -I_{REF} + I_S$$

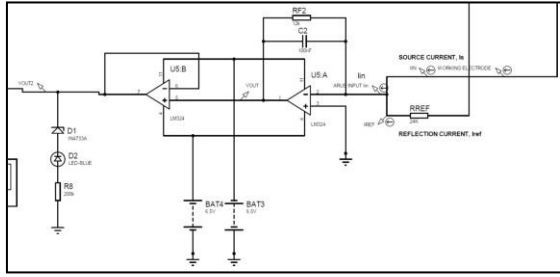


FIGURE 18: Current receiving circuit

Refer to equation below,

$$V_{OUT} = -I_{IN} \times R_{F2}$$

V_{OUT} can be calculated from the I_{IN} current passing through the R_{F2} resistor on the transimpedance amplifier. As shown in Figure 18, V_{OUT} will flow through the voltage follower amplifier circuit and exit as V_{OUT2} , it is read by pin A0 ANALOG INPUT of the microcontroller. Table 3 shows the range of voltage values, V_{OUT2} based on $\pm 20\%$ margin of input current value received for comparison in the microcontroller.

Table 3: List of accepted V_{OUT2} voltage value ranges

INPUT - 0.2*INPUT (min) (mA)	INPUT (mA)	INPUT + 0.2*INPUT (max) (mA)
V _{OUT2} (max)	V _{OUT2}	V _{OUT2} (min)
2.51145	2.51145 (0.00mA)	2.51145
2.50954	2.50907 (0.0002mA)	2.50859
2.50763	2.50668 (0.0004mA)	2.50573
2.50382	2.50191 (0.0008mA)	2.50000
2.49904	2.49594 (0.0013mA)	2.49283
2.49331	2.49978 (0.0019mA)	2.48424
2.48758	2.48161 (0.0025mA)	2.47565

The linear voltage supply in the form of pulse width modulation (PWM) is generated through the use of the `analogWrite()` program in the Arduino microcontroller. The `analogWrite()` function is to specify the duty cycle for the PWM signal. The PWM duty cycles produced in this study are 20%, 30%, 40%, 50%, 60%, 70% and 80%. The PWM linear voltage should be generated based on the

et al., 2018). Figure 19 shows the PWM signal generated from the Arduino in the simulation for the voltages of 1.0V, 1.5V, 2.0V, 2.5V, 3.0V, 3.5V and 4.0V.

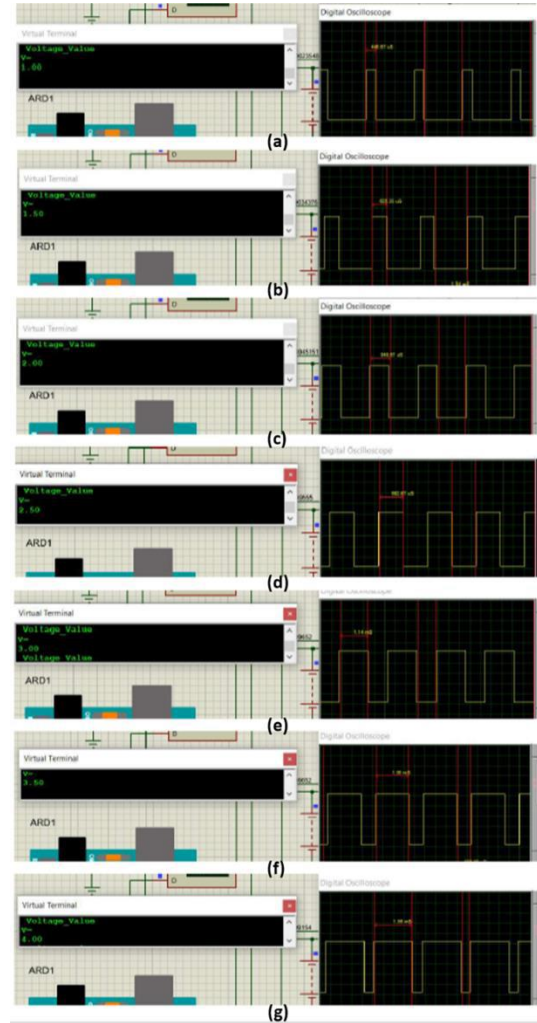


FIGURE 19: Simulation image of PWM signal from Arduino: (a) 1.0V (b) 1.5V (c) 2.0V (d) 2.5V (e) 3.0V (f) 3.5V (g) 4.0V

Leptospira detection system simulation

Table 4 shows the ADC levels based on the voltage value (V_{OUT2}) read by the Arduino microcontroller. This can be derived from the use of the `analogRead()` program in Arduino. The `analogRead()` function is to read the voltage value from pin A0 of the Analog Input. The Arduino board contains a 10-bit analog to digital converter (ADC). This means it will map the input voltage between 0 and the operating voltage (5V) to an integer value between 0 and 1023 using equation below.

$$ADC\ LEVEL = V_{OUT2} \times \frac{1023}{5}$$

linear sweep voltammetry of the study results (Jurait

Table 4: ADC level according to V_{OUT2}

INPUT - $0.2 \times \text{INPUT}$ (min)		INPUT		INPUT + $0.2 \times \text{INPUT}$ (max)	
$V_{OUT2}(\text{max})$	ADC LEVEL	$V_{OUT2}(\text{V})$	ADC LEVEL	$V_{OUT2}(\text{min})$	ADC LEVEL
2.51145	513	2.51145	513	2.51145	513
2.50954	513	2.50907	512	2.50859	512
2.50763	512	2.50668	511	2.50573	511
2.50382	511	2.50191	511	2.50000	510
2.49904	510	2.49594	510	2.49283	509
2.49331	509	2.49978	508	2.48424	508
2.48758	508	2.48161	507	2.47565	506

The leptospira detection system program was constructed based on the ADC level in Table 4. The digit value of this ADC is the range of input values received based on the range of $\pm 20\%$ margin. Figure 20 and Figure 21 are the simulation results of the Leptospira detection system for 1.0V and 1.5V voltages. The LCD board display shows “BACTERIA IS PRESENT” if the current value, IS from the DC current source matches the current value recorded in the Arduino, otherwise the Arduino displays “BACTERIA IS NOT PRESENT” if it does not match. The Arduino can determine the presence of bacteria based on a comparison of the current data recorded in the Arduino with the received current data. For this simulation the current value supply is from a DC current source. For current values from DC current sources that exceed the range, Arduino will decide that the presence of bacteria is negative by displaying “BACTERIA IS NOT PRESENT” on the LCD board.

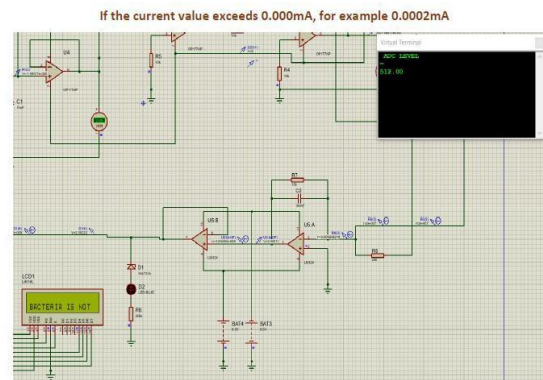
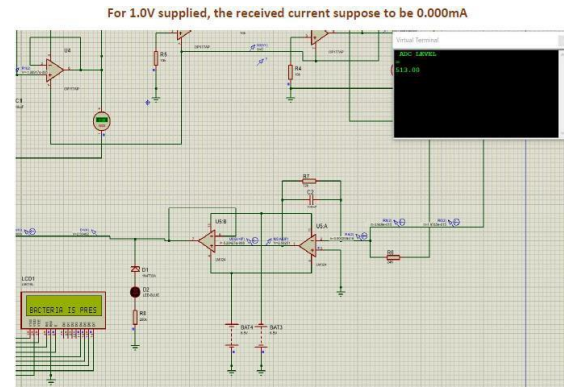


FIGURE 20: Simulation results of Leptospira 1.0V detection system for input current: (a) 0.00mA (b) 0.0002mA

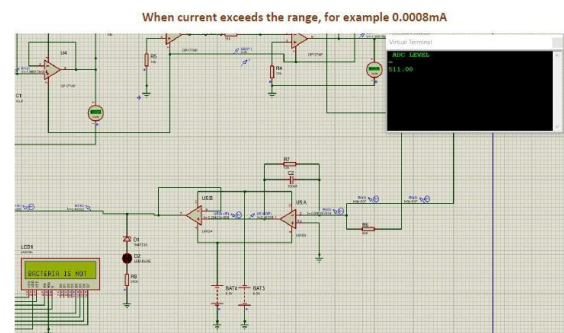
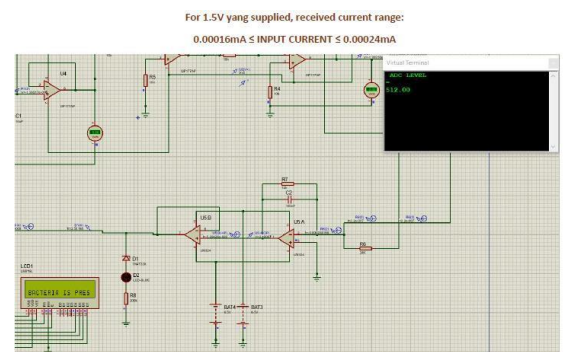


FIGURE 21: Simulation results of 1.5V Leptospira detection system for input current: (a) 0.00022mA (b) 0.0008mA

Leptospira detection apps

Once the designed application is completed, the application download package (Android APK file) can be generated with the 'Build' option in the web application. The APK file can be downloaded by generating a QR code and scanning the code for download in the phone, or by choosing to save the APK to a computer then download it manually on the phone. The size of the built -in application is 10.16MB.

The first phase of testing was done by checking whether the phone application could connect to the HC-05 Arduino Bluetooth module using Bluetooth. Figure 22 shows the results of a Bluetooth connection. Once the application and Arduino are connected, the next phase is to test the application to display the input current value in the Arduino entered through the *SERIAL MONITOR* to make a comparison with the current value recorded in the Arduino and the result showing the presence of bacteria with "BACTERIA PRESENT" or vice versa "BACTERIA NOT PRESENT". An example of the test process is illustrated in. Figure 23 which shows that when the input current value matches the range of current values recorded in the Arduino, the application displays the input current value and the Arduino result "BACTERIA PRESENT". Figure 24 shows the application displaying "BACTERIA NOT PRESENT" when the input current value does not match the recorded current range.

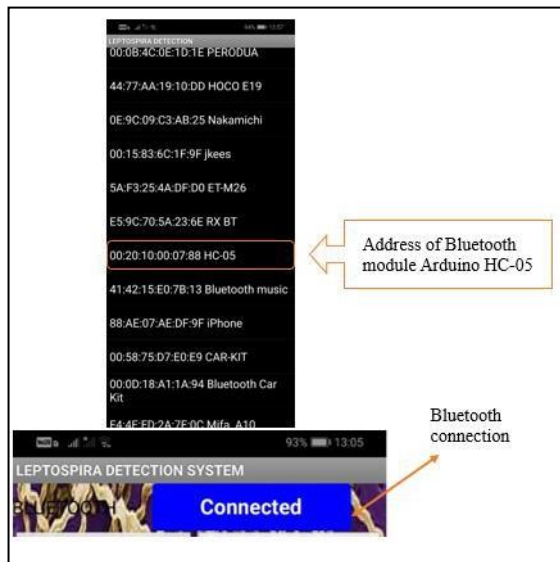


FIGURE 22: Bluetooth connection status

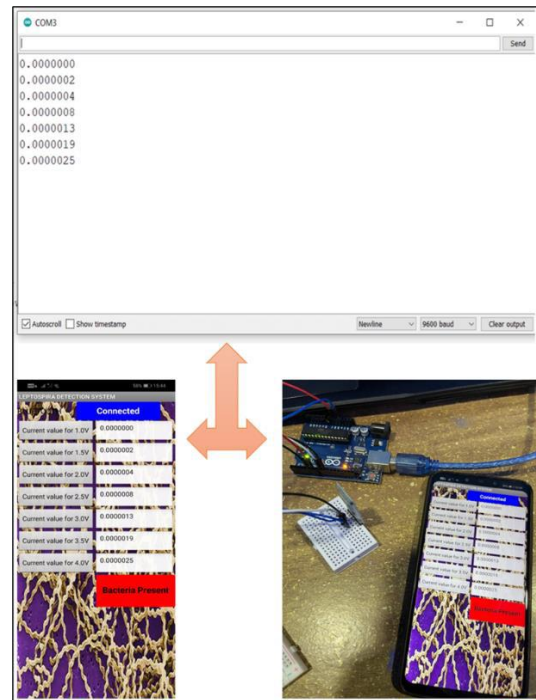


FIGURE 23: The application displays "BACTERIA PRESENT" when the current value is in the range of Leptospira presence

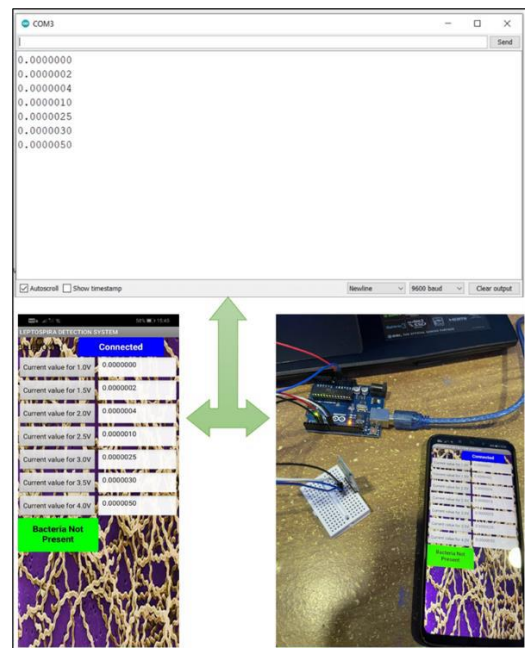


FIGURE 24: The application displays "BACTERIA NOT PRESENT" when the current value is outside the range of Leptospira presence

CONCLUSION

A portable biosensor reader was successfully designed in this study. All three of the desired

objectives were proven to be successful. Linear sweep voltammetry has been discovered as an electroanalytic method for application in the construction of leptospira detection systems (LSV). The designed potentiostat receives the provided voltage in a linear form. The current at the working electrode is measured when the voltage between the counter electrode and the reference electrode is swept linearly during a fixed time interval in linear sweep voltammetry. This is an effective method for the detection of leptospira.

An Arduino microcontroller and multiple circuits comprising an operational amplifier are used to design the voltametric potentiostat. Active low pass filters, inverting amplifiers, transimpedance amplifiers, and non-inverting amplifiers, commonly known as voltage followers, are among the operating amplifier circuits employed. The Arduino's PWM signal is successfully converted to an analogue voltage form, which is then provided to the counter electrode. The current reading from the working electrode can be fed into the Arduino by converting current to voltage, making the Analog pins more understandable.

An on-site leptospira detection system is designed with Arduino microcontroller used was programmed based on the PANI Fe-Al biosensor specifications to detect the presence of leptospira in detail. The developed smartphone app can display leptospira presence and decision making made by Arduino.

ACKNOWLEDGEMENTS

This research was supported by grants GUP-2020-014. The authors would like to thank to the Universiti Kebangsaan Malaysia for supporting this project.

REFERENCES

- Adler, B., & de la Peña Moctezuma, A. (2010). Leptospira and leptospirosis. *Veterinary Microbiology*, 140(3–4), 287–296. <https://doi.org/10.1016/j.vetmic.2009.03.012>
- Azizi, S., Kheirandish, R., & Rahimi, E. (2014). Comparison of polymerase chain reaction and Warthin-Starry techniques to detect Leptospira spp. in kidneys of slaughtered cattle. *The Onderstepoort Journal of Veterinary Research*, 81(1), 1–6. <https://doi.org/10.4102/ojvr.v81i1.821>
- Benacer, D., Who, P. Y., Zain, S. N. M., Amran, F., & Thong, K. L. (2013). Pathogenic and saprophytic Leptospira species in water and soils from selected urban sites in peninsular Malaysia. *Microbes and Environments*, 28(1), 135–140. <https://doi.org/10.1264/jsme2.ME12154>
- Costa, F., Hagan, J. E., Calcagno, J., Kane, M., Torgerson, P., Martinez-Silveira, M. S., Stein, C., Abela-Ridder, B., & Ko, A. I. (2015). Global Morbidity and Mortality of Leptospirosis: A Systematic Review. *PLoS Neglected Tropical Diseases*, 9(9), 0–1. <https://doi.org/10.1371/journal.pntd.0003898>
- Jampasa, S., Lae-ngee, P., Patarakul, K., Ngamrojanavanich, N., Chailapakul, O., & Rodthongkum, N. (2019). Electrochemical immunosensor based on gold-labeled monoclonal anti-LipL32 for leptospirosis diagnosis. *Biosensors and Bioelectronics*, 142(May), 111539. <https://doi.org/10.1016/j.bios.2019.111539>
- Jurait, J., Abdullah, H., Bejo, S. K., & Yahya, I. (2018). *nanocomposite thin films for identification of pathogenic Leptospira*. 1515–1528.
- Kaur, H., & Shorie, M. (2019). Nanomaterial based aptasensors for clinical and environmental diagnostic applications. *Nanoscale Advances*, 1(6), 2123–2138. <https://doi.org/10.1039/c9na00153k>
- Meloni, G. N., Profesor, A., & Prestes, L. (2016). *Building a Microcontroller Based Potentiostat: A Inexpensive and Versatile Platform for Teaching Electrochemistry and Instrumentation*. 1320–1322. <https://doi.org/10.1021/acs.jchemed.5b00961>
- Nagraik, R., Kaushal, A., Gupta, S., Dhar, P., Sethi, S., & Kumar, D. (2019). Optimized DNA-based bioassay for Leptospira interrogans detection: a novel platform for leptospirosis diagnosis. *3 Biotech*, 9(7), 3–9. <https://doi.org/10.1007/s13205-019-1815-4>
- Scholz, F. (2015). Voltammetric techniques of analysis: the essentials. *ChemTexts*, 1(4), 1–24. <https://doi.org/10.1007/s40828-015-0016-y>
- Thakur, B., Amarnath, C. A., Mangoli, S. H., & Sawant, S. N. (2015). Polyaniline nanoparticle based colorimetric sensor for monitoring bacterial growth. *Sensors and Actuators, B: Chemical*, 207(Part A), 262–268. <https://doi.org/10.1016/j.snb.2014.10.045>
- Vasconcellos, F. A., Coutinho, M. L., da Silva, É. F., Fernandes, C. P. H., Monte, L. G., Seyffert, N., Dellagostin, O. A., & Aleixo, J. A. G. (2010). Testing different antigen capture ELISA formats for detection of Leptospira spp. in human blood serum. *Transactions of the Royal Society of Tropical Medicine and Hygiene*, 104(4), 259–264. <https://doi.org/10.1016/j.trstmh.2009.10.005>

The Development Of Solar Charger Based On Sun Detector Using Arduino

(Pembangunan Pengecas Solar Berasaskan Pengesan Suria Menggunakan Arduino)

Izzuan Bin Ismail, Nor Azwan Mohamed Kamari

Department of Electrical, Electronic and Systems Engineering,

Faculty of Engineering & Built Environment, Universiti Kebangsaan Malaysia, Malaysia

**Corresponding author: A166302@siswa.ukm.edu.my*

ABSTRACT

Green energy, often known as renewable energy, has recently received a lot of attention. Solar energy, hydro potential energy, wind energy, biomass energy, and terrestrial heat are examples of renewable energy sources. Solar energy is one of these that is both effective and practical. Solar panels are very popular nowadays, and they are frequently used to convert solar energy into electricity. The majority of solar panels on the market and in use today are static, meaning they cannot create more power. To gather more sunlight, the solar panel should always be parallel to the sun. Using solar panel tracking, this technology seeks to generate more power from sunlight. The power generated by the solar panels will be at their peak if they are parallel to the sun. In other words, the location of the solar panel is the focus of this project. Hardware, electrical, and software development are all part of this system. The microcontroller is then connected to the motor servo and sensor circuit. Finally, write a programme to operate the sensor and servo motor, and upload it to Arduino. The purpose of this project is to create a system that automatically tracks the position of the sun. The device will adjust the angle of the solar panels to maintain them parallel to the sun at all times, generating maximum power. A single-axis sun detector device is provided in this project, and its effectiveness is tested. Finally, the solar panel on this system can be changed to follow the sun's movement and might even charge electronic devices such as smartphones.

Keywords: Solar Panel; Motor Servo; Sensor; Single Axis Solar Detector; Telephone

ABSTRAK

Tenaga yang boleh diperbaharui yang terkategori sebagai tenaga hijau telah mendapat banyak perhatian pada masa kini. Antara jenis tenaga yang boleh diperbaharui adalah tenaga solar, tenaga keupayaan hidro, tenaga angin, tenaga biojisim dan haba daratan. Antara tenaga yang paling mendapat sambutan di Malaysia adalah tenaga solar. Pada masa kini, panel solar adalah yang popular dan sering digunakan untuk menukar tenaga solar kepada tenaga elektrik. Kebanyakan panel solar yang wujud dan digunakan sekarang adalah statik, kesannya ia tidak boleh menjana kuasa yang lebih maksimum. Dalam usaha untuk mendapatkan lebih banyak tenaga, kedudukan panel solar perlu sentiasa selari dengan matahari. Objektif utama bagi projek ini adalah untuk menjana lebih banyak kuasa daripada cahaya matahari dengan menggunakan panel penjejak matahari. Jika panel solar selari dengan matahari, kuasa yang dijana daripada panel solar akan menjadi maksimum. Sistem ini terdiri daripada pembangunan perkakasan, elektrik dan perisian. Perintang bergantung cahaya telah digunakan sebagai sensor untuk mengesan cahaya matahari. Kemudian, motor servo dan litar sensor disambungkan dengan pengawal mikro. Seterusnya, membangunkan satu program untuk mengawal sensor dan stepper motor dan memasukkan program pada Arduino. Matlamat projek ini adalah untuk membangunkan satu sistem pengesan kedudukan matahari secara automatik. Sistem ini akan menggerakkan panel solar supaya selari dengan matahari dan menjana kuasa yang maksimum pada setiap masa. Dalam projek ini, peranti pengesan solar satu paksi dibentangkan dan telah diuji keberkesanannya. Akhir sekali, solar panel pada sistem ini dapat diselaraskan mengikut pergerakan matahari dan mampu untuk mengecas peranti elektronik seperti telefon.

Kata Kunci: Panel Solar; Motor Servo; Pengesan; Panel Pengesan Matahari Satu Paksi; Telefon

INTRODUCTION

Demand for electricity generation is increasing over time. The total average amount of electricity generation in 2018 is 20261 TeraWatt hours per year. Energy sources include coal, natural gas, oil, biomass, nuclear energy and renewable energy such as solar energy, hydropower and geothermal energy. Among renewable energy, solar energy is a clean and renewable energy source. Solar energy is

the best way to reduce its carbon footprint and it does not cause environmental pollution. Not only that, this renewable energy does not release any greenhouse gases. It only needs a light source to function. Therefore, it is safe and environmentally friendly. However, there are still many people, especially in Malaysia, who still doubt why solar energy is good.

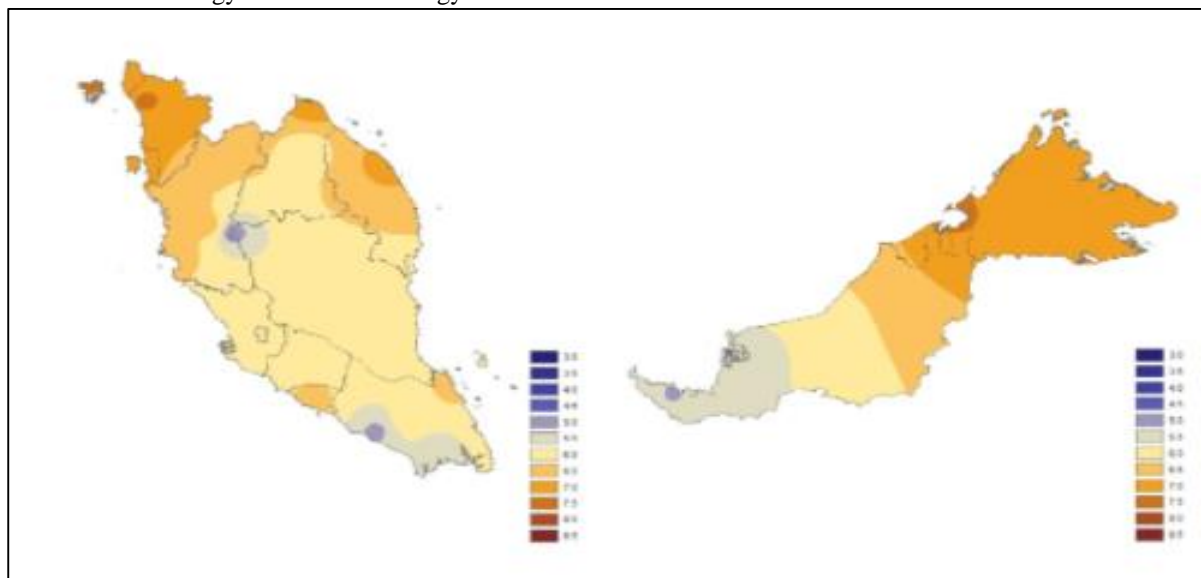


FIGURE 1. Annual radiation rate in malaysia.

Figure 1 shows the average annual rate received by each area in Malaysia. Almost 98 percent of the states in Malaysia get a high value rate while 2 percent get a moderate value. Sunlight consists of two components namely “direct rays” which carry about 90 percent of solar energy and “diffuse sunlight.” Since most of the energy is in direct radiation, maximum accumulation requires the sun to be visible by the panel for as long as possible. On more cloudy days, the ratio of direct and diffused light can drop as low as 60:40 or lower.

Problem Statement

Malaysia is one of the countries that use energy resources from petroleum and natural gas. Based on statistics released by Tenaga Nasional Berhad, a total of 685 million kilowatts of energy were supplied to homes in 2016. However, there was an increase of 31 percent to 900 million kilowatts in 2019. This change in data shows that the demand for electricity supply is very high in Malaysia from time to time. Based on non-renewable resources as the main source of power generation, Malaysia will experience the problem of depletion of natural resources in the long run.

With a high average annual radiation rate, Malaysia has the potential to become a country that uses solar energy as a source of power. Today, the use of solar systems is very widespread among Malaysians either for personal use or facilities provided by the government itself. The use of static type solar systems has become a major choice among consumers. This type of static solar system only points in one direction according to the suitability of the place and the highest average rate of radiation produced by the sun. With this static position of the solar panel it cannot take advantage of all the radiation produced by the sun as the earth rotates on its axis.

There are several types of solar energy available and can be used including solar thermal technology, passive solar extraction and photovoltaic type solar. All these types of solar energy have the same function which is to capture sunlight to produce electricity in different ways. The selection of the photovoltaic type solar system is the most suitable for use in Malaysia because photovoltaic type solar has the highest efficiency in accordance with the weather in Malaysia compared to other solar systems.

Literature Review

Solar tracker type systems produce more electrical energy than static type solar systems. This is because the radiation emitted by the sun is exposed directly parallel to the surface of the solar board. In addition, the amount of space required by a solar tracking system is equal to the amount of surface required to build a fixed type solar system making it ideal for optimizing the amount of land surface to be used. Technological advances and the reliability of electronic and mechanical components make this system durable for a long period of time while reducing concerns about ongoing maintenance over time. (Pratik Pawar, Ashish Yadav, Pritam Makwana 2018)

Although solar energy is a good source of energy, there are some improvements made to obtain maximum results in utilizing solar energy. Among the improvements made is by using a solar tracking system instead of a fixed system. Introduction of the idea of developing a single axis solar solar tracker for solar panels. The circuit is controlled by an Atmega328P microcontroller, two dependent resistors (LDR) and a servo motor. The purpose of the research was to see a comparison of the output voltage readings for fixed type panels and solar tracker type. (Jumaat et al. 2018)

METHODOLOGY

Experiment Design and Procedure

The system consists of 3 main parts namely input, main controller and output. The inputs are for sensors and power supply while the outputs are included with servo motors and solar panels.

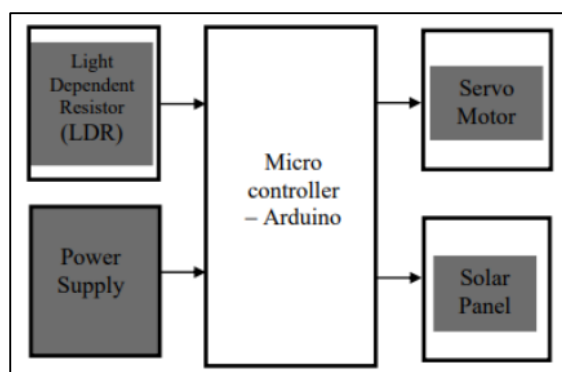


FIGURE 2. Hardware configuration

Figure 2 above describes the overall arrangement of the components and how the system

works. The microcontroller is used as the main key of the controller to control all parts of the system. The Arduino Uno is used to process data input and output and control the solar tracking system. It is also used because of its suitability for small systems and easy to program. In addition, the Arduino Uno can also control many types of sensors, especially servo motors. For the input part, a light dependent resistor (LDR) is connected to the main controller, the Arduino Uno. LDR is used because it can detect sunlight and provide data to the microcontroller for processing. The LDR functions as a sunlight detector and it indicates the direction of sunlight by comparing the intensity of received sunlight. For system output, servo motors have been used to move the solar platform. It will receive the processed data from the microcontroller and move as programmed. Its movement is in the direction of sunlight received by the Light Dependent Resistor. After that, the solar panel will receive and transform the light into electricity as shown below.

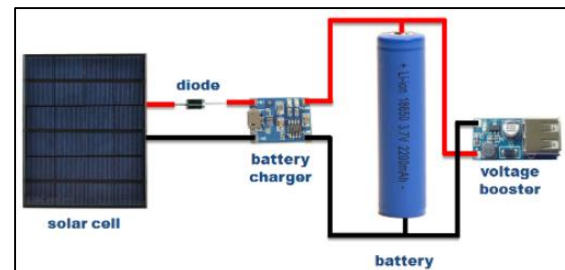


FIGURE 3. Solar charge control circuit.

Figure 3 above shows the connection of the battery as well as the components needed to produce 5V output. In this project, the battery used is a Lithium-ion type battery with a capacity value of 2000 mAh. While the output is 3.7V in direct current. A push switch is installed to turn the circuit on and off. At the end of the circuit, a voltage booster with a USB type A connection is used to boost the voltage up to 5V output voltage.

RESULTS AND DISCUSSION

Simulation

The simulation of the solar detector circuit is done in matlab simulink application. This simulation involves the movement of the sun as well as solar panels. Figure 4 shows the arrangement of components and circuits for a solar panel of a solar detector.

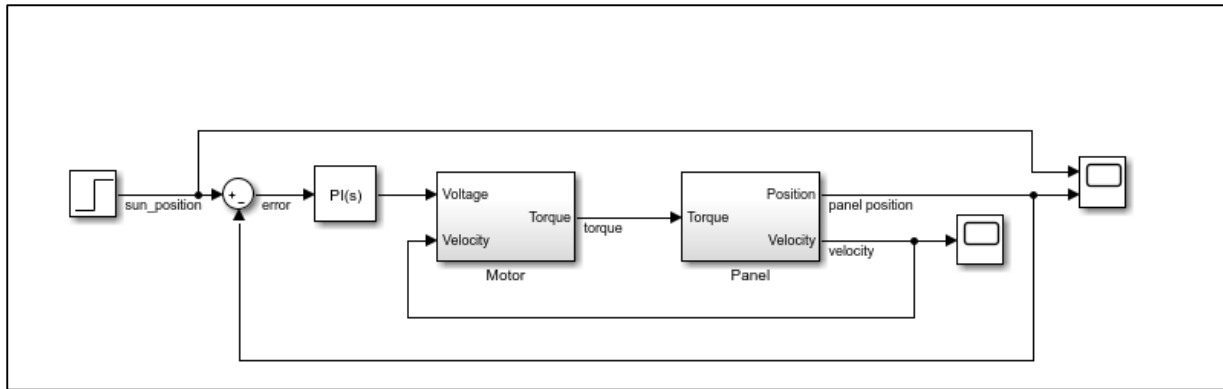


FIGURE 4. Circuit simulation using matlab

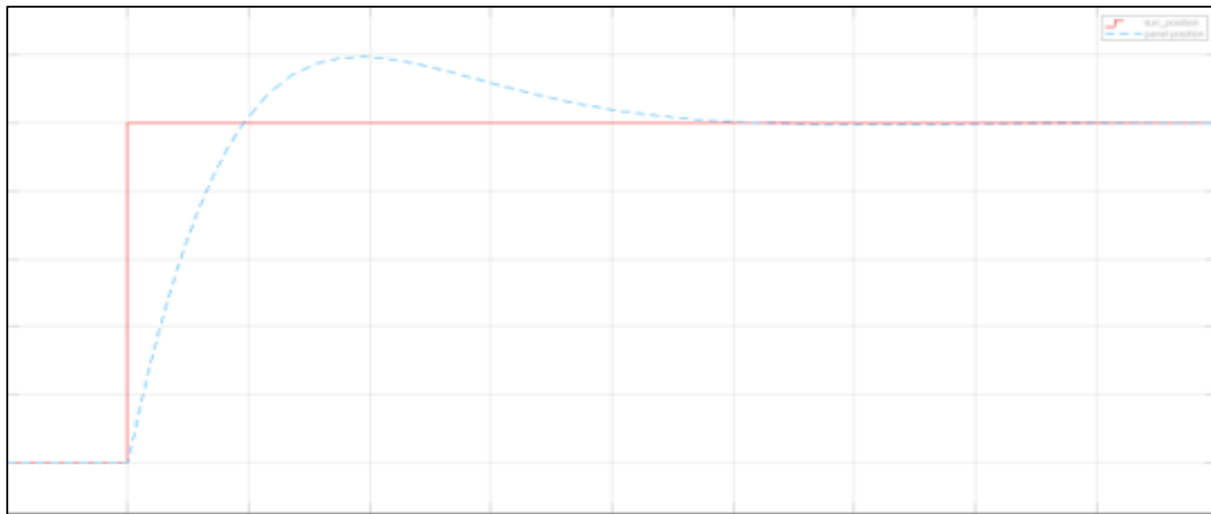


FIGURE 5. Output simulation

Figure 5 above shows the position of the sun and solar panels. X-axis is time while, y-axis stand for displacement. The red color signal indicates the position of the sun while the blue color signal indicates the position of the solar panel. This simulation test is performed in the matlab simulink application. While the data for the position of the sun is also taken from the matlab source which contains the movement of data for the sun in real situations. The data for this sun explains that the sun will be in the east in the morning and slowly move west in the evening. In the diagram above the x-axis refers to a predetermined time in a clock, while the y-axis refers to the position of the solar and solar panels.

Prototype

Because of its solid structure and ease of nailing or screwing, hard wood is the best choice for prototyping and building the frame. But before the framework is made, measurements and sketches should be done first to ensure the project runs as planned. In addition, the project dimensions should include all electronic components used in the project such as battery, solar panel, arduino uno and servo motor.

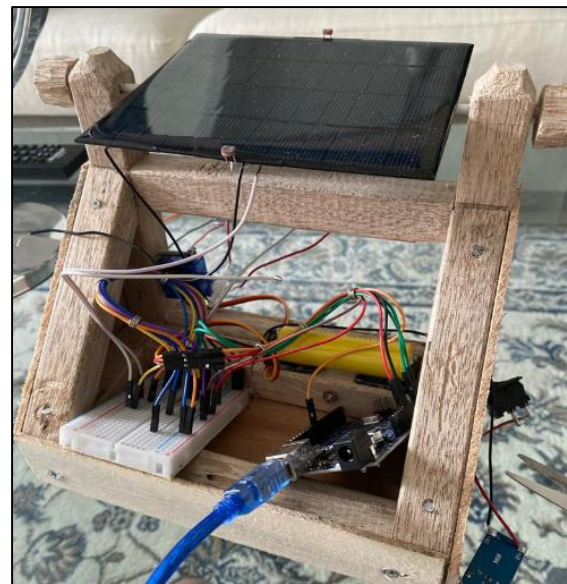


FIGURE 6. Arrangement of components

Figure 6 describes the connection and assembly of components into a prototype. Testing on the applicability of all components to the prototype is done to prove the effectiveness of simulation tests that have been done previously can be practical. The solar panel is placed on the surface of the prototype

while the position of the two LDRs is between the two corners of the left and right solar panel. All other components such as the arduino, battery and voltage booster module are placed in the center of the prototype.

The connection made between the solar panel and the servo motor. The wire is tied to a hole found on the blade of the servo motor which is then connected and glued to the bottom surface of the solar panel. Overall, both ends of the motor blade are fastened and connected to the left and right surface

of the solar panel. This will cause every movement made by the servo motor will also move the solar panel in parallel with its movement. Ultimately, the LDR will find the signal where the position of the highest light intensity is parallel to the position of the sun and then send the signal to the arduino for processing. The Arduino will collect and send a signal to the servo motor to perform the motion. The slight movement performed by the servo motor also results in the movement of the solar panel to move parallel to the position of the sun's rays.



FIGURE 7. Measurement of output voltage on solar panel.

TABLE 1. Output voltage for solar panel.

Number of trials	Output voltage(V)
1	3.01
2	3.83
3	2.91
4	0.71
5	1.61
6	3.35
7	2.73
8	2.05
9	3.48
10	3.50

Figure 7 above shows the method of measurement that has been done. Measurements are performed using a digital multimeter that has been set to dc voltage measuring mode. All measurement data are shown in table 1. A total of ten measurement experiments were performed to identify the characteristics of the output voltage. As shown the highest output voltage from the solar panel is 3.83V and the lowest is 0.71V.

Next, measurements of current and voltage were performed on the voltage booster module. This measurement is important to make sure the current and voltage values are the same as other chargers out there. The current and voltage values should be 5mA and 5V dc respectively. This is a fixed value for charging all devices that use usb type A. In figure 8 below shows the measurement method and output values for current and voltage.



FIGURE 8. Measurement of current and voltage values.



FIGURE 9. Final result.

Figure 9 above shows the testing of a sun tracker solar panel. The position of the solar panel moves according to the light emitted by the phone which acts as radiation from the sun. Both light-dependent resistors work as planned. The resistor responds to changes in light intensity that occur between the resistors. Then the motor moves the solar panel from 45 degrees to 145 degrees. Finally testing the effectiveness of phone charging was carried out.

CONCLUSION

In conclusion, a solar charger system based on solar detectors using arduino has been developed. A system using photovoltaic solar panels is used in this project to capture and convert light into electrical energy. Later, the use of lithium-ion batteries as an energy storage field. Next, the effectiveness of solar panel solar trackers has been tested for effectiveness.

Finally, the system is capable of charging phones and other devices such as power banks.

ACKNOWLEDGEMENT

I would like to thank Dr. Nor Azwan Bin Mohamed Kamari as my supervisor for his assistance and guidance throughout this research. Beside that, special thanks to my family, friends and all my lecturers for their support through my journey to finish this project.

REFERENCES

- (Zone 1 Conference of the American Society for Engineering Education 2014 Bridgeport et al. 2014)AAmaral, G. 2013. No Covariance structure analysis of health-related indicators in the elderly at home with a focus on subjective health
Title. *Journal of Petrology* 369(1): 1689–1699.
- Gustavsson, J. 2016. Energy Storage Technology Comparison. *KTH School of Industrial Engineering and Management*: 44.
- Hossain, C.A., Chowdhury, N., Longo, M. & Yaïci, W. 2019. System and cost analysis of stand-alone solar home system applied to a developing country. *Sustainability (Switzerland)* 11(5).
- Jumaat, S.A., Tan, A.A.A., Abdullah, M.N., Radzi, N.H., Hamdan, R., Salimin, S. & Bin Ismail, M.N. 2018. Horizontal single axis solar tracker using arduino approach. *Indonesian Journal of Electrical Engineering and Computer Science* 12(2): 489–496.
- Khan, M.T.A., Tanzil, S.M.S., Rahman, R. & Alam, S.M.S. 2010. Design and construction of an automatic solar tracking system. *ICECE 2010 - 6th International Conference on Electrical and Computer Engineering*(December): 326–329.
- Modules, C. 1993. 12V Solar Panels 1(603): 0–1.
- Peter, C. 2018. Servo Motor SG90. *Micro motor* 1(2): 180.
- Pratik Pawar, Ashish Yadav, Pritam Makwana, S. patil. 2018. Solar Tracking System Using Arduino. *International Journal of Research and Scientific Innovation* 5(2): 186–188.
- Scrosati, B. & Garche, J. 2010. Lithium batteries: Status, prospects and future. *Journal of Power Sources* 195(9): 2419–2430.
- Sohag, H.A., Hasan, M., Khatun, M. & Ahmad, M. 2016. An accurate and efficient solar tracking system using image processing and LDR sensor. *2nd International Conference on Electrical Information and Communication Technologies, EICT 2015*(Eict): 522–527.
- Vitae, C. 2013. Universiti Teknikal Malaysia Melaka: 1–7.

Zohari, M.H., Heidzer, M., Abidin, Z., Iqbal, L. & Mokhtar, M.H. 2020. Development of Smart Solar Tracking System 2: 31–37.

Zone 1 Conference of the American Society for Engineering Education 2014 Bridgeport, C., Kongar, E., American Society for Engineering Education, Engineering education: industry involvement and interdisciplinary trends proceedings of the 2014 Zone 1 Conference of the American Society for Engineering Education: April 3-5, 2014, University of Bridgeport, Bridgeport, Connecticut, U.S.A. IEEE.:

High Performance Cuk Converter Controller

(Rekabentuk Sistem Kawalan Penukar Cuk Berprestasi Tinggi)

Muhammad Khairul Naim Saaey, Yushaizad Yusof, Radin Za'im Radin Umar

Department of Electrical, Electronic and Systems Engineering,
Faculty of Engineering & Built Environment, Universiti Kebangsaan Malaysia, Malaysia
*Corresponding author: naimsaaey98@gmail.com

ABSTRACT

In today's energy systems, many equipment operates with Direct Current (DC) voltage. However, normal power supply may not always be able to provide the voltage level required for the operation of these devices. As a result, DC-DC converters are utilised to achieve the desired voltage values for equipment that operates at various DC voltage levels. The Cuk converter, which has a low output ripple voltage and can work in both Buck and Boost modes, is the most popular. A continuous current at both the converter's input and output is a significant advantage of the Cuk converter. The Cuk converter has a lot of reactive components and puts a lot of current stress on the switch. The Cuk converter uses an additional inductor and capacitor to store energy. Because the feedback loop must maintain regulation, some form of compensation is unavoidable in order to maintain loop stability. Controlling the load voltage based on changeable supply voltage, reference voltage, frequency and load power is the scope of the control methods. The PI controller is the most extensively utilised controller in industrial settings where system speed is not a concern. OCC method is nonlinear method that uses the concept of control of average value of switching variable at every cycle. FLC is the simplest controller because it does not involve mathematical module and famous in the industry where speed is the most important. The performances of PI, OCC and FLC controllers were compared with respect to performance parameters such as steady state error, voltage overshoot, ripple percentage, settling time and rise time. When the results obtained were evaluated as a whole, it was observed that FLC achieved the desired reference with less rise and settling time. In PI output voltage, it has less steady state error compare others. In OCC, the output voltage has less ripple percentage compare others. In this study, modeling and controller applications of Cuk converter are realized by using MATLAB / SIMULINK program.

Keywords: Converter, Cuk, System, Controller, PI, OCC, FLC

ABSTRAK

Marcapada ini terdapat banyak peralatan menggunakan voltan arus terus-ke-arus terus (AT-AT). Sehubungan itu pelbagai aras arus terus ke arus terus (AT-AT) diperlukan di dalam sesebuah mesin kerana terdapat pelbagai jenis litar. Oleh itu, agak mustahil untuk mendapatkan voltan keluaran yang diperlukan sekiranya hanya satu aras tenaga yang dibekalkan tanpa penukar arus terus-ke-arus terus (AT-AT) yang membekalkan pelbagai nilai voltan keluaran mengikut keperluan. Penukar arus terus-ke-arus terus (AT-AT) yang akan dibincangkan adalah penukar Cuk yang menyediakan voltan keluaran lebih tinggi ataupun voltan keluaran yang rendah berbanding voltan masukan. Kelebihan penukar Cuk ialah arus berterusan di tempat masuk dan keluar penukar. Kelemahan penukar Cuk adalah mempunyai komponen reaktif yang banyak dan tinggi tekanan arus pada di suis. Penukar Cuk menggunakan dua pendaras dan dua pemuat untuk menyimpan tenaga. Penukar Cuk memerlukan sebuah pengawal untuk menyuap balik dan memampas ralat pada voltan keluaran kepada litar semula untuk proses litar yang lengkap. Beberapa jenis pemampas diperlukan dan tidak dapat dielakkan untuk mencapai kestabilan pada voltan keluaran. Oleh itu, fokus akan diberikan kepada kawalan pada voltan di beban mengikut pemboleh ubah voltan masukan, voltan rujukan, frekuensi dan nilai beban. Setelah dikaji kawalan PI, adalah kawalan yang paling popular digunakan dalam industri di mana kelajuan tidak menjadi isu utama. OCC pula kawalan cara tidak kelulusan yang menggunakan purata konsep jumlah purata pada pemboleh ubah pada suis pada setiap pusingan. Kawalan FLC pula sebuah kawalan mudah tanpa menggunakan model matematik dan popular dalam industri di mana kelajuan menjadi aspek keutamaan. Prestasi semua kawalan akan dibandingkan dan dianalisis berdasarkan beberapa aspek seperti masa naik, masa penetapan, voltan terlajak, ralat keadaan mantap dan peratus riak. Apabila keputusan dianalisis secara holistik, pengawal FLC mencapai voltan rujukan dengan masa naik dan masa penetapan yang pendek berbanding pengawal-pengawal yang lain. Pengawal PI pula mempunyai ralat keadaan mantap yang paling rendah antara pengawal-pengawal yang lain. Kelebihan OCC pula

mempunyai peratus riak yang paling rendah. Dalam kajian ini reka bentuk kawalan penukar Cuk gelung terbuka dan gelung tertutup disimulasikan menggunakan program MATLAB/SIMULINK.

Kata Kunci: Penukar Cuk; FLC; OCC; PI; Pengawal

INTRODUCTION

Switching circuits can convert a certain dc voltage to another precise level are known as dc to dc converters. Buck, Boost, Buck–Boost, Cuk, Zeta, and Sepic are the most common dc/dc converters. The dc to dc converters are widely applied in distributed generation resource, power factor correction ,air-space industry ,cranes ,vehicles ,electrical motors and renewable energy resources such as fuel cells and photovoltaic.(Babaei & Seyed Mahmoodieh 2014) Cuk converter has many active components and has higher switching stress to the switch. Cuk converter use additional capacitor and inductor for saving energy. Due to the feedback loop is required to keep on regulation, some type of compensation is inevitable to satisfy the loop stability. Next, simulation output voltage is slightly difference to calculated output voltage for open loop due to internal resistance. Without a controller in open loop the output voltage has a higher ripple percentage and not robust.(Kannan et al. 2017)

Effect of controller will be analyzed based on changing variable that is input voltage, reference voltage and load value.(Marimuthu & Umamaheswari 2019) The main concern is to identify which controller is the best that give output voltage has less settling time, rise time, ripple percentage, steady state error and made Cuk converter operating in high performance. Specifications of DC-DC converters include precise acceleration control, excellent efficiency, quick dynamic response, and the use of fewer power switches. High performance means that when changing the input voltage, reference voltage and load value the output voltage still follow the time and reference voltage. Hence Cuk converter can be chosen as the higher order converter for the implementation of the inverter.

The main difference between DC-DC converters is that they use different topologies. In this study, we used a Cuk converter which is a type of Cuk switch. Its main advantage is that it has continuous input and output currents.(Arun Srinivas et al. 2020)

The control strategy of a converter can be achieved by controlling the S switch's off state or on state. The multiply operating modes of the converter are shown in Figure 1.

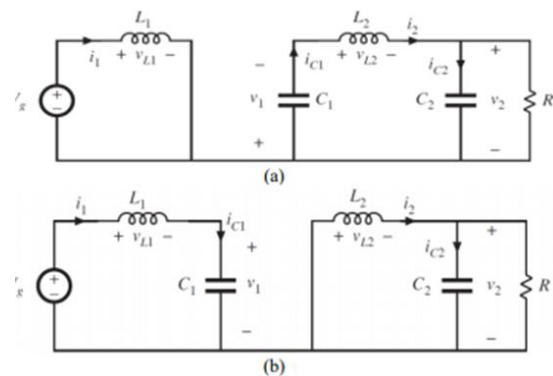


FIGURE 1: Circuits of the converter for on/off states of the switches during;(a)On state,(b)Off state

The two parts of the converter circuit are divided into two components, which are described in Figure 1. When the transistor switch is turned on, current through inductor L1, rises. At the same time, the voltage of capacitor C1 is lowered to prevent the diode D1 from acting as a reverse bias. When the input voltage is switched on, the forward biased D1 of diode is used to charge the capacitor C1 and the energy is transferred to the load through L2.(Pratiwi et al. 2020)

The Cuk converter can vary the voltage depending on the duty cycle. It can also step the voltage up or down. The Cuk converter contains the series inductors at both input and output, so it has much lower current ripple in both circuits.(Soedibyo et al. 2016). The quality of the output voltage is an important parameter, and it should have the least amount of ripple as possible. Furthermore, the switching current stress in these converters should be kept to a minimum. In this study, three controller has been chosen for Cuk controller which are OCC, PI and FLC.

The one-cycle control (OCC) methodology is a nonlinear control method has advantage of the switching converters pulsed and nonlinear nature to accomplish quick dynamic control of the switched variable's average value.(Ćuk 1995) After a transient, the average value of the switched variable only requires one switching cycle to achieve a new steady-state.

Between the reference signal and the average value of the switched variable, there is no steady-state or dynamic error.(Kasthala 2017) Fast dynamic responsiveness, great power source perturbation, robust performance, and automatic switching error correction are all features of this approach. It has been widely used in dc-dc conversion, particularly in buck converters, power amplifiers as control methods, power factor correction, active shunt power filters, multi-input

DC-DC converters.(Kannan et al. 2017)On the other hand, OCC has a faster transient reaction, a shorter settling time, and a lower maximum deviation from steady state than PI control. The steady state error of PI control is quite small. When the load is modified when OCC is implemented, some spikes may occur. The Cuk converter with PI control, does not have these spikes.(Bildirici & Karaarslan 2017).

The second controller in this study are Fuzzy Logic controller (FLC). The most notable aspect of fuzzy control, which has recently emerged as a key competitor to classical controllers in the field of control, is that it relieves the designer of mathematical procedures. Fuzzy logic-based controllers are currently used in practically every industry, from vehicle brake systems to washing machines and freezers to factory product quality control systems (Priyadarshi et al. 2019).

To construct the controller in the classic types of controls (P, PI, and PID), a number of mathematical expressions must be examined. Although this procedure is straightforward for linear systems, it necessitates the completion of complicated mathematical operations in the case of nonlinear systems. It is not necessary to analyse the mathematical expressions when developing an FLC for any linear or non-linear system.

Fuzzification, rule base, and defuzzification are the three main components of the fuzzy logic controller (YILMAZ et al. 2020), which was first employed by Mamdani in 1974. Figure 2 illustrates the FLC basic block diagram.

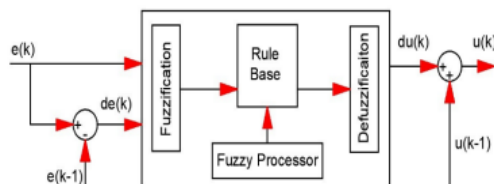


FIGURE 2. Basic block of FLC controller

According to Fig. 2, the error (e) and change of error (de) refers to inputs of the system and, the control signal (u) refers to the output system.

Because of its simple form and implementation, the Proportional-Integral PI Controller is the last controller in this study that is most used to control the DC-DC converter output voltage. A PI controller uses the error signal as the control loop's feedback(Devi & Srivani 2016).A proportional control system and an integrated control system are coupled to control a plant in a PI control system. The ability of a PI control system to modify the plant according to the set-point value while maintaining the plant position steady at a preset set-point value and having a faster response time are examples of strong performance. The exact constants needed in each of these control systems are proportional (K_p) and integral (I) to get the best

results on the performance of PI controllers .This constant value must be established in order to achieve good control results, including faster response times, more steady output, and low overshoot error values. (Karaarslan 2018) The diagram of the PI controller block used for the proposed system is represented in Figure 3.

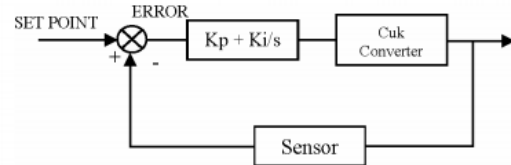


FIGURE 3. Block Diagram PI controller

Figure 3 is a schematic of a PI controller. Minimizing the error signal is one of the control functions. The error signal is the difference between the desired and actual magnitude. The controller will be predisposed to speed up or slow down the achievement of the target settings as a result of this difference.(Shoumi et al. 2020)

METHODOLOGY

Open loop Cuk Converter

In open loop, Cuk converter can increase and reduce the output voltage based on the duty cycle. The series inductors are present at both the input and output of the Cuk converter, resulting in substantially lower current ripple in both circuits. The switch duty cycle can be used to calculate the average output voltage.(Asadi et al. 2017) Duty cycle,

$$D = \frac{-V_o}{V_s - V_o} \quad (1)$$

where, D is on time duration of switch/ total switching time period.

$$\text{Output voltage, } V_o = \frac{-DV_s}{1-D}$$

For open loop, two simulation were done to study the effect of duty cycle in output voltage, the first simulation the duty ratio was 0.4 and the parameter were calculated in this equation:

Duty cycle

$$D = \frac{-V_o}{V_s - V_o} = \frac{12}{18 - (-12)} = 0.4 \quad (1)$$

Inductor current of inductance I_{L1}

$$I_{L1} = \frac{P_s}{V_s} = \frac{40}{18} = 2.222 \text{ V} \quad (1)$$

Inductor current of inductance I_{L2}

$$I_{L2} = \frac{P_s}{-V_o} = \frac{40}{-12} = 3.333 \text{ A} \quad (2)$$

Rate of change inductor ΔI_{L1}

$$\Delta I_{L1} = I_{L1} \times 10\% = 2.222 \times 10\% = 0.222 \text{ A} \quad (3)$$

Rate of change inductor ΔI_{L2}

$$\Delta I_{L2} = I_{L2} \times 10\% = 3.333 \times 10\% = 0.333 A \quad (5)$$

$$\text{Inductor value, } L_1 \quad (4)$$

$$L_1 = \frac{V_S D}{\Delta I_{L1} f_s} = \frac{(18)(0.4)}{(0.222)(50000)} = 649 \mu H$$

$$\text{Inductor value, } L_2 \quad (5)$$

$$L_2 = \frac{V_S D}{\Delta I_{L2} f_s} = \frac{(18)(0.4)}{(0.333)(50000)} = 432 \mu H$$

$$\text{Capacitor value, } C_2 \quad (6)$$

$$C_2 = \frac{1 - D}{r 8 L_2 f^2} = \frac{1 - 0.4}{(0.01)(8)(432 \mu H)(50000)^2} = 6.94 \mu H$$

$$\text{Rate of change capacitor, } \Delta V_{C1} \quad (7)$$

$$\Delta V_{C1} = (V_S - V_O) r_{C1} = (18 - (-12))(0.01) = 0.3 A$$

$$\text{Load resistance, } R \quad (8)$$

$$R = \frac{(V_o)(V_o)}{P} = \frac{(12)(12)}{40} = 3.6 \Omega$$

$$\text{Capacitor value, } C_1 \quad (9)$$

$$C_1 = \frac{V_O D}{R f \Delta V_{C1}} = \frac{(12)(0.4)}{(5)(0.3)(50000)} = 64 \mu H$$

For second simulation the duty ratio that has been chosen is 0.6 to make sure the Cuk converter working in Boost mode to increase the input voltage, the calculation for parameter:

$$\text{Duty cycle, } D \quad (10)$$

$$D = \frac{-V_O}{V_S - V_O} = \frac{18}{12 - (-18)} = 0.6$$

$$\text{Inductor current of inductance, } I_{L1} \quad (11)$$

$$I_{L1} = \frac{P_S}{V_S} = \frac{40}{12} = 3.33 A$$

$$\text{Inductor current of inductance, } I_{L2} \quad (12)$$

$$I_{L2} = \frac{P_S}{-V_O} = \frac{40}{18} = 2.22 A$$

$$\text{Rate of change inductor, } \Delta I_{L1} \quad (13)$$

$$\Delta I_{L1} = I_{L1} \times 10\% = 3.333 \times 10\% = 0.333 A$$

$$\text{Rate of change inductor } \Delta I_{L2} \quad (14)$$

$$\Delta I_{L2} = I_{L2} \times 10\% = 2.222 \times 10\% = 0.222 A$$

$$\text{Inductor value, } L_1 \quad (15)$$

$$L_1 = \frac{V_S D}{\Delta I_{L1} f_s} = \frac{(12)(0.6)}{(0.333)(50000)} = 432 \mu H$$

Inductor value, L_2

$$L_2 = \frac{V_S D}{\Delta I_{L2} f_s} = \frac{(12)(0.6)}{(0.222)(50000)} = 649 \mu H \quad (16)$$

$$\text{Capacitor value, } C_2 \quad (17)$$

$$C_2 = \frac{1 - D}{r 8 L_2 f^2} = \frac{1 - 0.6}{(0.01)(8)(432 \mu H)(50000)^2} = 4.29 \mu H$$

$$\text{Rate of change capacitor, } \Delta V_{C1} \quad (18)$$

$$\Delta V_{C1} = (V_S - V_O) r_{C1} = (12 - (-18))(0.01) = 0.3 A$$

$$\text{Load value, } R \quad (19)$$

$$R = \frac{(V_o)(V_o)}{P} = \frac{(18)(18)}{40} = 8.1$$

$$\text{Capacitor value, } C_1 \quad (20)$$

$$C_1 = \frac{V_O D}{R f \Delta V_{C1}} = \frac{(18)(0.6)}{(8.1)(1.5)(50000)} = 89 \mu H$$

TABLE 1. Cuk converter parameter

Simulation	Simulation 1	Simulation 2
Input voltage	18	12
Simulation output voltage	12.01	18
Calculation output voltage	12	18
Frequency	50 kHz	50 kHz
Duty Cycle	0.4	0.6
Ripple %	10%	10%
Inductor 1	649 μ H	432 μ H
Inductor 2	432 μ H	649 μ H
Capacitor 1	6.94 μ F	89 μ F
Capacitor 2	64 μ F	4.29 μ F
Load	3.6 Ω	8.1 Ω

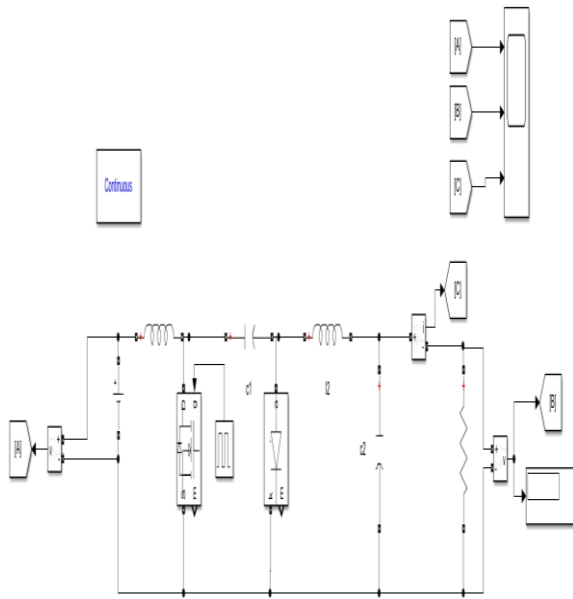


FIGURE 4. Open loop Cuk Converter

Figure 4 shows Cuk converter in MATLAB/SIMULINK. This circuit has 2 inductor, 2 capacitor, 2 switch which are MOSFET, diode and 3 sensor. The sensor that has been used in the circuit are voltage sensor and current sensor to detect the value of currents and voltage at the load for analysis. All the parameter that has been calculated and determined has been inserted in the circuit to do simulation.

Closed Loop Controller Cuk Converter

By definition, power converters are non-linear, with a different structure for each switching cycle. Due to saturating inductance and voltage clamping, they have non-linearity difficulties. The efficiency and stability of DC-DC converters suffer as a result of this non-linearity. The primary goal of the control action is to put the system's steady-state and dynamic behaviour within well-defined bounds of steady-state error, overshoot, and settling time, while also improving response and stability.

The converters switching losses are reduced by having a good dynamic responsive. For the control of DC-DC converters, a variety of linear and non-linear controllers are used. Although linear converters are simple and straightforward to use, they are poor in dealing with system parameter change. In order to overcome these drawbacks, various types of controller are developed in this study which are PI, OCC and FLC. All the parameters are the same for the three controllers to get the best analysis on output voltage.

PI controller

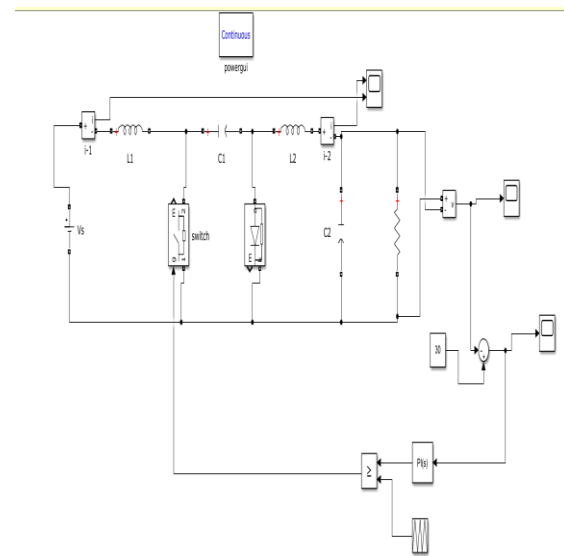


FIGURE 5. Cuk converter with PI controller

Figure 5 shows Cuk circuit with PI controller. Output voltage errors enter back to the MOSFET after the voltage has been compensated by the PI block. Two ways to determine the values of K_p and K_I are Ziegler-Nichols second method and heuristic method. For this circuit, the heuristic method has been chosen to get the values of K_p and K_I because the output voltage using the heuristic method has better overshoot in output voltage compared to the Ziegler-Nichols second method. The heuristic method is any approach to problem solving or self-discovery that employs a practical method that is not guaranteed to be optimal, perfect, or rational. The most fundamental heuristic is trial and error, by entering the values of K_p and K_I manually and at the same time, the output voltage was observed to get the best result. Reference voltage also has been used to subtract the output voltage in the second scope; if the value in the second scope is zero, the error in output voltage has been successfully compensated.

OCC Controller

Figure 6 depicts a one-cycle control technique's basic circuit. The clock signal is generated via a resettable integrator, a comparator, an SR flip-flop, and an oscillator (clock). Let $U(t)$ be the input signal, and $W(t)$ be the output signal. In a single switching cycle of the switch 'SW', the desired averaged output value is produced. The oscillator determines the switching period T_s (constant) using the clock signal. For a time T_{on} the switch is closed and $W(t)=U(t)$. When T_{off} the switch is opened and $W(t)=0$. Thus the average value of output is the same as the average of an input signal over the ON period. Figure 6 is the concept of OCC controller and Figure 7 is OCC in MATLAB/SIMULINK.

$$W = \frac{1}{T_s} \int W(t) dt = \frac{1}{T_s} \int_0^{T_{on}} U(t) dt \quad (21)$$

Where \bar{W} = The average value of output $W(t)$ = Instantaneous value of Output signal $U(t)$ = Instantaneous value of Input signal T_s = Switching Period

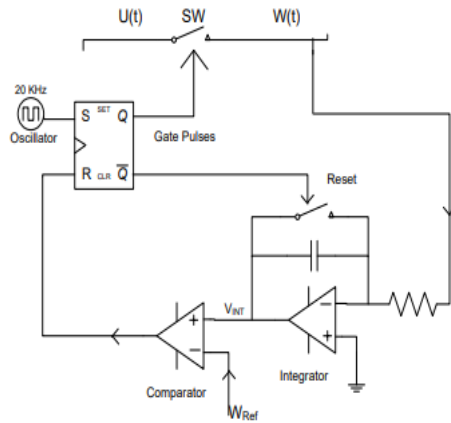


FIGURE 6. OCC Controller concept

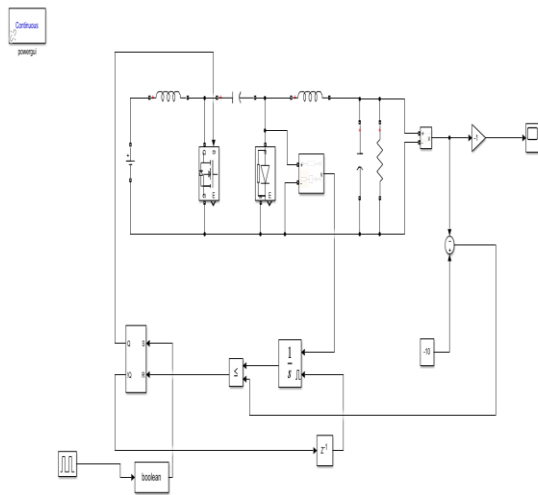


FIGURE 7. Cuk Converter with OCC controller

FLC Controller

Fuzzy logic-based controllers are currently used in practically every industry, from vehicle brake systems to washing machines, freezers, and factory quality control systems. From figure 8 the error and change of error enter the FLC block to compensate the error before entering the MOSFET for complete the cycle.

In this rule base in FLC block, “e” represents error, “de” represents error change and “du”

represents output. The terms Negative Big (NB), Negative Small (NS), Zero Error(ZZ), Positive Small (PS), and Positive Big (PB) are all terms used to describe the rules in FLC blocks. The following is a quick summary of how fuzzy control rules work. When a system's output is lower and farther than the stated reference point, indicating a significant positive error, the controller must immediately increase the output voltage.

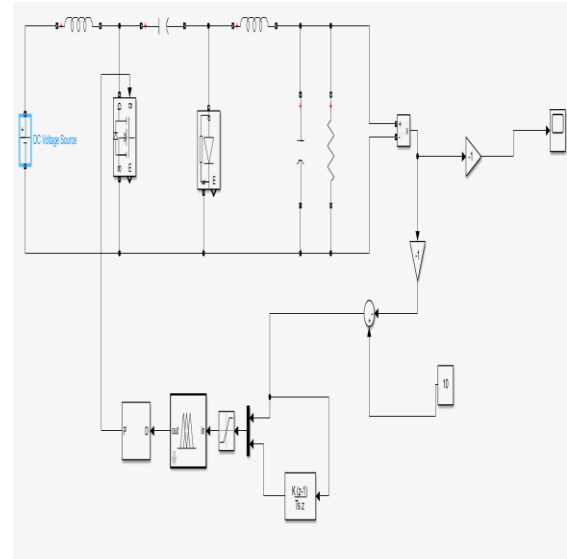


Figure 8. FLC controller

Table 2 Base rule in FLC block

Error/ change of error	Negative Big (NB)	Negative Small (NS)	Zero Error(ZZ)	Positive Small (PS)	Positive Big (PB)
Negative Big (NB)	Positive Big (PB)	Positive Big (PB)	Positive Big (PB)	Positive Small (PS)	Positive Small (PS)
Negative Small (NS)	Positive Big (PB)	Positive Small (PS)	Positive Small (PS)	Positive Small (PS)	Zero Error(ZZ)
Zero Error(ZZ)	Positive Small (PS)	Positive Small (PS)	Zero Error(ZZ)	Negative Small (NS)	Negative Small (NS)
Positive Small (PS)	Zero Error(ZZ)	Negative Small (NS)	Negative Small (NS)	Negative Small (NS)	Negative Big (NB)
Positive Big (PB)	Negative Small (NS)	Negative Big (NB)	Negative Big (NB)	Negative Big (NB)	Negative Big (NB)

Dynamic response Cuk converter

Two important factors influencing the dynamic response are the control loop(s) and the dc-dc converter topology. By an optimized design on the control loop compensator the dynamics can be improved. After designing the best circuit, two reference point were choose to make sure high performance cuk converter can operate in two mode which are Buck and Boost. For PI and OCC controller before 0.3 seconds reference voltage were set to 10 V and after 0.3 second the reference were

change to 50 V to make sure the converter can operate in Boost mode. For FLC the reference voltage were set same as PI and OCC but the voltage reference change after 0.03 seconds. All the output voltage were observed and make comparison based on settling time, rise time, ripple percentage and stability.

Parameter closed loop

All the three converter has same parameter as Table 3 for make sure when do comparison, the result observed were analyze fairly. The parameter was choose because the component value are easy to do and realistic for doing hardware.

Table 3 Cuk converter for all controller

Controller	PI	OCC	FLC
Vin(V)	40	40	40
Vout(V)	10	10	10
L1	0.1mH	0.1mH	0.1mH
L2	0.1mH	0.1mH	0.1mH
C1	1000 μ F	1000 μ F	1000 μ F
C2	1000 μ F	1000 μ F	1000 μ F
F	50 kHz	50 kHz	50 kHz
R	18 Ω	18 Ω	18 Ω

RESULT

Open Loop Cuk Converter

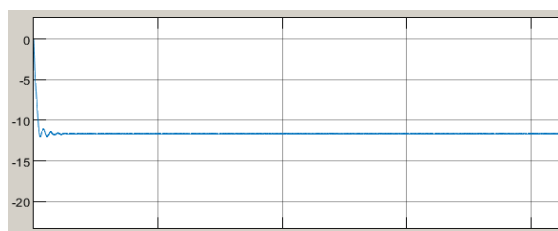


Figure 9 Output voltage for duty cycle 0.4

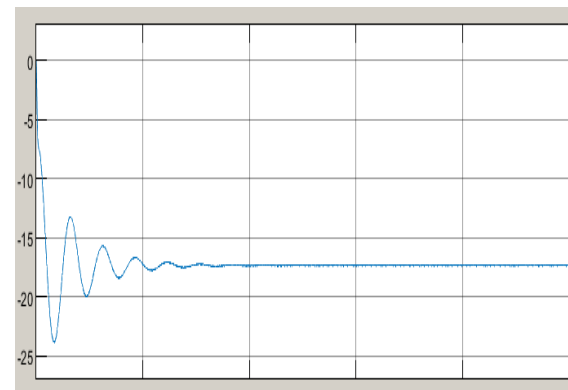


Figure 10 Output voltage for duty cycle 0.6

When duty cycle 0.4 in Figure 9, output voltage form in simulation is 12 V and this shows this Cuk converter in mode Buck has reducing input voltage from 18 V. For duty cycle 0.6 in Figure 10, output voltage form shows that Cuk converter act as Boost converter that increase the input voltage from 12 V to 18 V. This shows that duty cycle effect the output voltage of Cuk converter.

Closed Loop Cuk Converter with PI,OCC and FLC controller

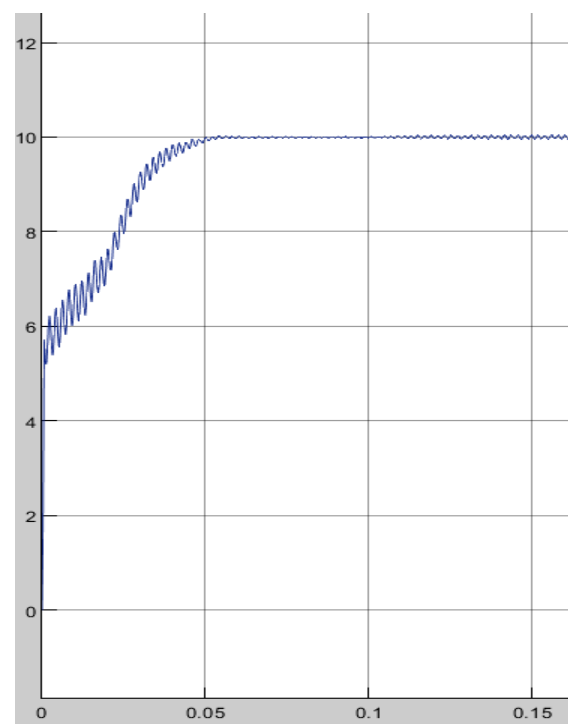


Figure 11 Output voltage PI controller

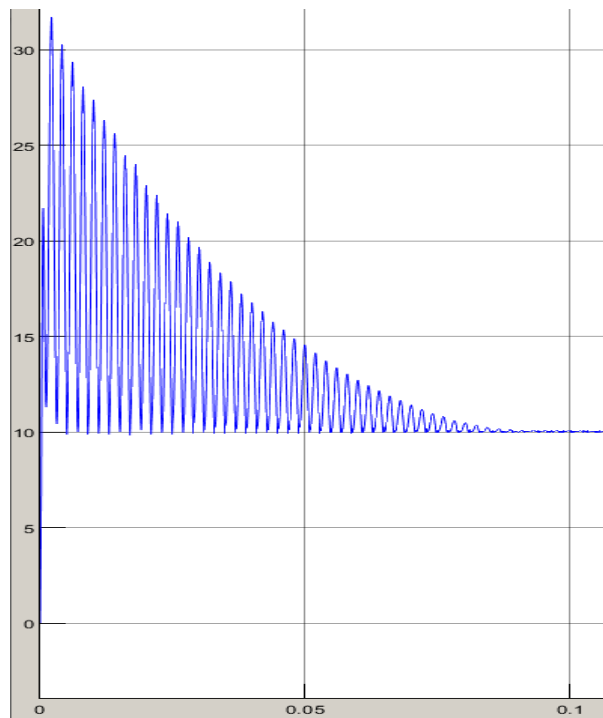


Figure 12 Output voltage OCC controller

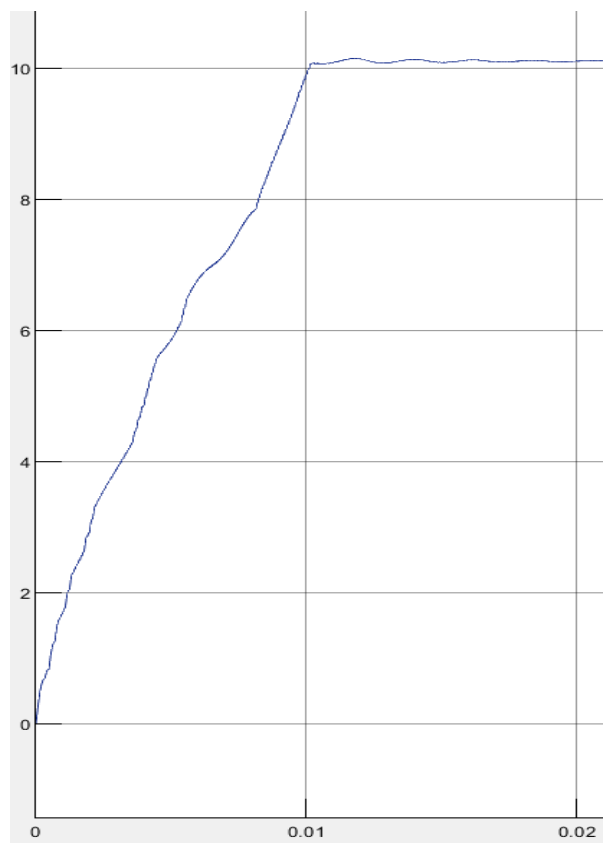


Figure 13 Output voltage FLC controller

Controller	PI	OCC	FLC
Rise time(ms)	29.461	39.321	0.009
%overshoot voltage	0.275	230	15
Settling time	0.0611s	0.0811s	0.012s
%Ripple	5	3	7
%Steady state error	1	2	5

For output voltage PI controller in Figure 11, PI controller has rise time and settling time second lowest compare to other controllers. Primary advantages for PI controller, it has minimum overshoot voltage and steady state error base on table 4. This shows, If the system doesn't need a fast response but an accuracy needed, so the PI controller is the best controller for the system. Based on simulation, when frequency chosen is less than 50 kHz, settling time will decreases but the ripple percentage on output voltage increases.

Figure 12 shows output voltage simulation on OCC controller that has highest value rise time, settling time and overshoot voltage compare others controller. Advantages for OCC it has less ripple percentage compare others controller. OCC is the most complex controller because it has many components and follows period cycle that has been control by SR flip-flop. Thus, OCC has highest overshoot voltage which is 230%. On top of that, system that suitable for OCC is system that focus on accuracy and ripple percentage. When frequency value less than 50 kHz, steady state error will reduce but after 40 kHz, output voltage become zero.

Based on output voltage in Figure 13, FLC output voltage has lowest rise time and settling time compare to others controller. Unfortunately, FLC has highest steady state error compare others controller. FLC is the simplest controller compare others because it operates base on rule base but unfortunately it has highest steady state error due the system operating on rule base that need expertise to choose the rules. The method for determine the rules are heustirical method which means try and error. FLC is the best controller for the system that require speed but not accuracy.

TABLE 4. Dynamic response for output voltage with controller PI, OCC and FLC

Based on all the simulation, ripple percentage in all controller can be reduced by changing value of inductor, load and frequency on Cuk controller.

Dynamic response for Cuk controller

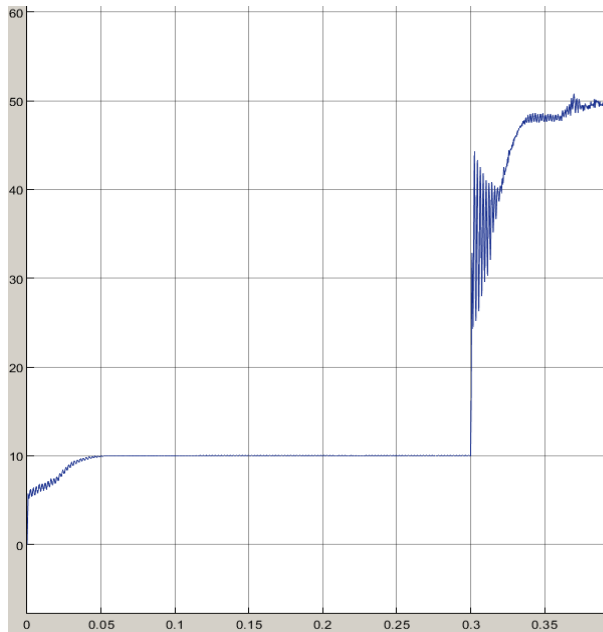


FIGURE 14. Dynamic response PI controller

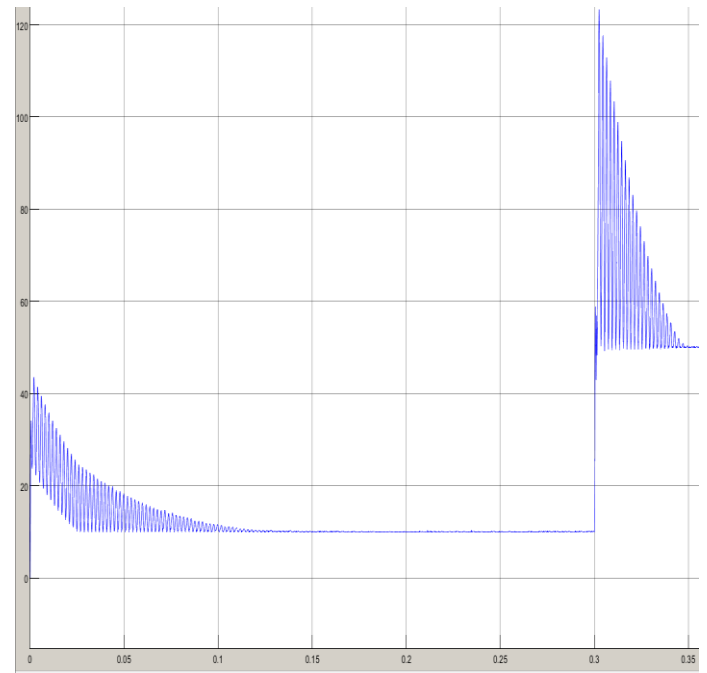


FIGURE 14. Dynamic response OCC controller

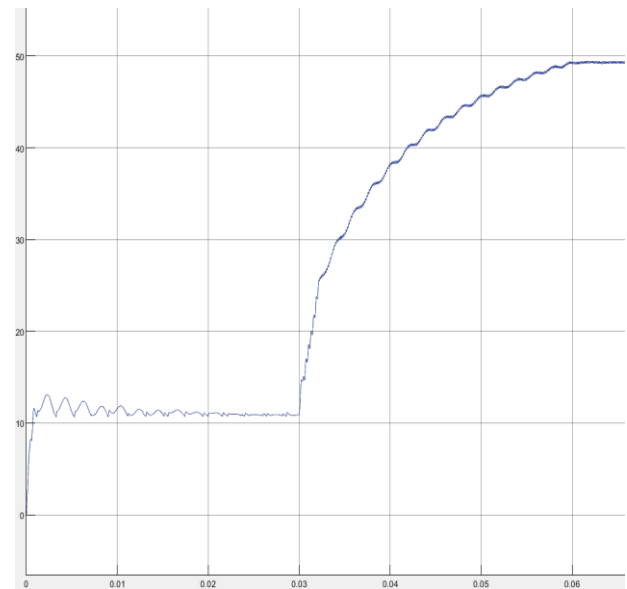


FIGURE 14. Dynamic response FLC controller

Table 5 Characteristic of output voltage when reference voltage change

Controller	PI	OCC	FLC
Settling time	0.06s	0.04s	0.03s
Rise time	0.056s	0.032s	0.024s
% Ripple	8%	5%	6%
Stability	stable	stable	stable

All the output voltage in Figure 14, Figure 15 and Figure 16 for three controllers are stable because the output voltage follows the reference voltage when the reference voltage change and output voltage stay at the same level as reference voltage. This show the circuit that has been designed can do both mode which is Buck and Boost. This controller also fulfills characteristic to become high performance controller.

From Table 5, FLC has settling time and rise time lowest follows by OCC and PI. For steady state error PI has lowest value and best accuracy to follow reference voltage.

CONCLUSION

In conclusion, Cuk converter can do both mode which are Buck and Boost. For open loop, duty cycle plays essential role for determine output voltage value. It also can be seen open loop output voltage is not robust and has higher ripple percentage that why a controller needed to solve the problem. In closed loop, the best performance based on speed are FLC because it has lowest rise time and settling time in output voltage. In term of accuracy, PI is the most accurate because it has lowest steady state error in output voltage. OCC controller has lowest ripple percentage but has highest overshoot output voltage.

ACKNOWLEDGEMENT

I would like to thank. Dr. Yushaizad Bin Yusof as my supervisor for his assistance and guidance through out this research. Special thanks to my family, friends and all my lecturer for their support through my journey to finish this project.

REFERENCES

- Arun Srinivas, T., Themozhi, G. & Nagarajan, S. 2020. Current mode controlled fuzzy logic based inter leaved cuk converter SVM inverter fed induction motor drive system. *Microprocessors and Microsystems* 74: 103002. doi:10.1016/j.micpro.2020.103002
- Asadi, F., Abut, N. & Akca, U. 2017. International Journal of Advanced and Applied Sciences Designing a PI controller for Cuk converter using converter dynamics toolbox for MATLAB. Designing a PI controller for Cuk converter using converter dynamics toolbox for MATLAB 4(6): 175–180.
- Devi, V. S. K. & Srivani, S. G. 2016. Performance assessment of PV energy conversion system with Buck-boost and Cuk converter for cascaded H-Bridge inverter. 2016 - Biennial International Conference on Power and Energy Systems: Towards Sustainable Energy, PESTSE 2016. doi:10.1109/PESTSE.2016.7516462
- Karaarslan, A. 2018. the Implementation of One Cycle Control Method To Inverting Buck-Boost Converter (June).
- Marimuthu, G. & Umamaheswari, M. G. 2019. Analysis and Design of Single Stage Bridgeless Cuk Converter for Current Harmonics Suppression Using Particle Swarm Optimization Technique. *Electric Power Components and Systems* 47(11–12): 1101–1115.
- Priyadarshi, N., Ramachandramurthy, V. K., Padmanaban, S. & Azam, F. 2019. An ant colony optimized mppt for standalone hybrid pv-wind power system with single cuk converter. *Energies* 12(1). doi:10.3390/en12010167
- Kannan, R., Lokesh, N., Hasan, K. N. M. & Aravind, C. V. 2017. Implementation of one cycle controller for single phase bi-directional converter. *International*
- Soedibyo, Amri, B. & Ashari, M. 2016. The comparative study of Buck-boost, Cuk, Sepic and Zeta converters for maximum power point tracking photovoltaic using P&O method. *ICITACEE 2015 - 2nd International Conference on Information Technology, Computer, and Electrical Engineering: Green Technology Strengthening in Information Technology, Electrical and Computer Engineering Implementation*, Proceedings 327–332.
- Kasthala, S. 2017. Implementation of One Cycle Control Method in Buck and Boost Converter 6(6): 80–87.
- Ćuk, S. 1995. One-Cycle Control of Switching Converters. *IEEE Transactions on Power Electronics* 10(6): 625–633. doi:10.1109/63.471281
- Pratiwi, A. A., Efendi, M. Z. & Murdianto, F. D. 2020. CUK Converter for Power Factor Correction Using Moth Flame Optimization-PI Controller. *IOP Conference Series: Materials Science and Engineering* 982(1). doi:10.1088/1757-899X/982/1/012020
- Shoumi, H. N., Sudiharto, I. & Sunarno, E. 2020. Design of the CUK converter with PI controller for battery charging. *Proceedings - 2020 International Seminar on Application for Technology of Information and Communication: IT Challenges for Sustainability, Scalability, and Security in the Age of Digital Disruption, iSemantic 2020* 403–407. doi:10.1109/iSemantic50169.2020.9234

Simulation of the Performance of Iron Pyrite Thin Film Solar Cell by SCAPS 1-D

(Simulasi Tahap Prestasi Sel Suria Jenis Filem Nipis Ferum Disulfida Berdasarkan SCAPS 1-D)

Nik Khaliq Zailani Nik Iskandar^a, Badariah Bais^a, Puvaneswaran a/l Chelvanathan^b,

^aDepartment of Electrical, Electronic and Systems Engineering, Faculty of Engineering & Built Environment, Universiti Kebangsaan Malaysia, Malaysia

^bSolar Energy Research Institute (SERI), Universiti Kebangsaan Malaysia, 43600 Bangi, Malaysia

*Corresponding author: A164791@siswa.ukm.edu.my

ABSTRACT

Iron pyrite (FeS_2) is the material that have a higher absorption coefficient and potential to be alternative material to replace CIGS because of its abundance element and non-toxicity than CIGS which is have rare element such as indium and gallium. This study was conducted to study the performance of FeS_2 thin film solar cell as a p type semiconductor in solar cell by using simulation from SCAPS 1-D software. Maximum conversion efficiency of FeS_2 solar cells demonstrated to date, however, is below 3%, which is significantly below the theoretical efficiency limit of 25%. This poor conversion efficiency is mainly the result of the poor photovoltage, which has never exceeded 0.2 V with a device having appreciable photocurrent. In this study, electrical properties and physical properties of FeS_2 will be analysis for increasing the performance efficiency of FeS_2 inside of completed model structure of solar cell. Electrical properties and physical of FeS_2 that will be manipulate are the thickness, carrier density, band gap and electron mobility. Next, the numerical modelling will be done for increasing the performance of FeS_2 to optimum power. The performance of FeS_2 are determined by their efficiency, fill factor, short circuit current density, and open circuit voltage. The result of the study had shown the performance of FeS_2 is affected by every single electrical characteristic of FeS_2 that have been manipulated. Finally, the performance FeS_2 had shown improvement by using the simulation technique and suggestions of a few research directions are also presented.

Keywords: Solar Cell, Conversion Efficiency, Performance

ABSTRAK

Ferum disulfida (FeS_2) merupakan bahan yang mempunyai pekali penyerapan yang tinggi dan berpotensi sebagai bahan alternatif untuk menggantikan CIGS kerana unturnya mudah didapati dan tanpa toksin berbanding CIGS yang mempunyai unsur yang sukar ditemui seperti indium dan galium. Kajian ini dilakukan untuk mengkaji prestasi sel suria jenis filem nipis FeS_2 sebagai bahan semikonduktor jenis p dalam sel suria dengan kaedah simulasi menggunakan perisian SCAPS 1-D. Penukaran kecekapan maksima FeS_2 telah diperolehi, walaubagaimanapun, rendah daripada 3% dan menunjukkan perbezaan yang ketara dengan penukaran kecekapan teori iaitu 25%. Tahap penukaran yang kecekapan yang rendah telah menyebabkan hasil fotovoltan yang rendah, tidak mencecah 0.2 V dengan arusfoton yang sederhana terhadap peranti tersebut. Dalam kajian ini, sifat elektrik dan fizikal FeS_2 akan dianalisis bagi meningkatkan tahap prestasi kecekapan FeS_2 dalam satu model struktur sel suria yang lengkap. Sifat elektrik dan fizikal FeS_2 yang akan dimanipulasi adalah ketebalan, ketumpatan penerima, jurang jalur dan kelincahan elektron. Seterusnya, kaedah pemodelan berangka dibuat untuk mendapatkan nilai kecekapan yang optimum terhadap FeS_2 . Prestasi FeS_2 akan ditentukan oleh kecekapan, faktor isi, jumlah arus litar pintas dan voltan litar buka sel suria tersebut. Hasil kajian telah mendapati setiap sifat elektrik yang dimanipulasi memberi kesan terhadap prestasi FeS_2 . Kesimpulannya, prestasi FeS_2 telah menunjukkan peningkatan dari segi kaedah simulasi dan sedikit cadangan untuk kajian akan datang telah dinyatakan.

Kata Kunci: Sel Suria, Penukaran Kecekapan, Prestasi

INTRODUCTION

The greenhouse effect causes global warming, which is defined as an increase in average

global temperatures. Certain gases in the atmosphere operate like greenhouse glass, allowing sunlight to warm the earth's surface while storing the heat as it radiates back into space. The Earth becomes hotter as greenhouse gases pile up in the atmosphere. One

of the major factors of greenhouse effect was from the coal-fired power plant. Coal-fired power plants are a type of power plant that generates electricity by using combustion coal. The gases from coal-fired plant have affected the atmosphere layer become thinner and causes global warming. The effect can be reduced by replacing a coal-fired power plants with renewable power plant such as solar farm which is using solar energy to electrical energy.

Solar energy, often known as solar power, is the conversion of solar energy into electricity, which can be done directly using photovoltaics (PV), indirectly using concentrated solar energy, or a mix of both. Solar tracking systems and lenses or mirrors are used in concentrated solar energy systems to focus huge amounts of sunlight into little rays. Photo-voltage cells use photo-voltage effects to convert light into electrical current. Panels, inverters, racks, and solar battery storage units are the four basic components of a solar energy system (if required). Solar panels are the most visible component of solar energy systems, and numerous solar cells comprised of wafer-based crystalline silicon cells or thin film cells are used in solar panels. Second-generation solar cells are formed by spreading one or more thin layers, or a thin film (TF), of photovoltaic material on a substrate such as glass, plastic, or metal. In this study, pyrite thin film solar has been used to be simulate.

Pyrite (FeS_2) has long been recognized as a material with high potential as a solar absorber for photovoltaic devices (Rahman et al. 2020). This is due to pyrite's exceptional absorption coefficient ($>10^5 \text{ cm}^{-1}$ above 1.2–1.4 eV rendering a less than 100 nm thick-film capable of absorbing over 90% of the sun's light), good mobility ($>300 \text{ cm}^2 \text{ V}^{-1} \text{ s}^{-1}$ in single crystal form), and a suitable minority carrier diffusion length (100–1000 nm). However, its low open-circuit voltage ($V_{\text{OC}} < 0.2 \text{ eV}$) resulted from its narrow band gap of $E_g = 0.95 \text{ eV}$ leads to its low photoelectric conversion efficiency of 3% (Uchiyama et al. 2016), (Bhandari et al. 2017). Recently, various causes have been proposed to explain its low V_{OC} , including bulk defects, low intensity states at the bottom of the conduction band, intrinsic surface states and the presence of competing phases.

In this study, we develop one simple model structure for FeS_2 and investigated the performance of FeS_2 and examined conversion efficiency by using device simulation SCAPS 1-D. Furthermore, we modeled a device structure of n-semiconductor which can achieve high efficiency.

LITERATURE REVIEW

Understanding of Photovoltage Loss in Iron Pyrite Solar Cells

FeS_2 offers possibilities of the lowest priced electricity production among the known solar cell

materials. However, FeS_2 solar cells never have exceeded a PCE greater than 2.8% (Luo et al. 2015; Zhang et al. 2015). The fundamental difficulties behind this poor conversion efficiency have been documented as surface conduction phenomena and unwanted doping, which then lead to phenomena including surface inversion, ionization of deep donor states, and photocarrier recombination for photovoltage loss.

Increase Band Gap FeS_2 by Doping

Doping is a typical method for mediating the band gap of semiconductors by substituting isovalent elements for cations or anions. To boost the VOC of pyrite, doping with larger band gap material is used. Zn has been mentioned as a potential focus for future research. ZnS_2 is thought to have a band gap of 2.5 eV. Of all other known pyrite type candidates, including CoS_2 , MnS_2 , CuS_2 , NiS_2 , RuS_2 , and OsS_2 , however, CoS_2 is an itinerant electron ferromagnet below $T_c = 120 \text{ K}$, MnS_2 , CuS_2 are metallic materials, NiS_2 is not suitable to alloying with pyrite because its lower band gap. The remaining candidates are ZnS_2 , RuS_2 ($E_g^{\text{expt}} = 1.3 \text{ eV}$) and OsS_2 ($E_g^{\text{expt}} = 2.0 \text{ eV}$). In cation doping, the bowing effect will decrease the band gap when alloying with Zn, while Ru and Os alloying slightly increase the band gap. It is a very successful approach to increase the band gap by doping oxygen atoms in anion doping. Density functional theory shows that doping oxygen atoms can raise the band gap of FeS_2 by roughly 0.2–0.3 eV without creating gap states (DFT) (Liu & Zhang 2020).

METHODOLOGY

Overview

There are several steps that need to be followed to complete this study. In the first stage, the data parameter of each layer collected from the various articles and develop a simple solar cell model structure for FeS_2 . In the second stage, the simulation was performed to determined the FeS_2 performance by inspect the efficiency, open circuit voltage, fill factor, and short circuit current density. Lastly, we modeled a device structure of n-semiconductor which can achieve high efficiency.

DATA COLLECTING AND MODEL STRUCTURE

Table 1 shows the collected data parameter for each layer from the various articles. The data is used for the simulation for determined the performance of FeS_2 . Source from (Xiao et al.

2014),(Altermatt et al. 2002),(Yu et al. 2015) and (Hossain et al. 2018).

	Al:ZnO	n-CdS	p-FeS ₂
Thickness (µm)	200	0.05	0.9
Band gap (eV)	3.3	2.4	0.8
Electron affinity (eV)	4.6	4.2	4.5
Dielectric permittivity (relative)	9	10	13.6
CB effective density of states (cm ⁻³)	2.2x10 ¹⁸	2.2x10 ¹⁸	3x10 ¹⁸
VB effective density of states (cm ⁻³)	1.8x10 ¹⁹	1.8x10 ¹⁹	8.5x10 ¹⁹
Electron thermal velocity (cm/s)	1x10 ⁷	1x10 ⁷	1x10 ⁷
Hole thermal velocity (cm/s)	1x10 ⁷	1x10 ⁷	1x10 ⁷
Hole thermal velocity (cm ² /Vs)	1x10 ²	1x10 ²	1x10 ²
Hole mobility (cm ² /Vs)	25	25	2x10 ⁻²

TABLE 1 Layer for each parameter.

The simple model structure of solar cell created by the ideas from the articles. Al: ZnO as metal, CdS as n-type semiconductor and FeS₂ as p-type semiconductor as refer of FIGURE 1. The simulation will be conduct by the followed model structure.

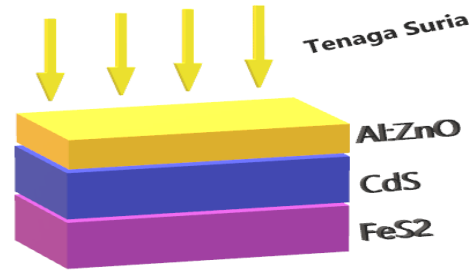


FIGURE 1 Model Structure

SIMULATION AND NUMERICAL MODELING

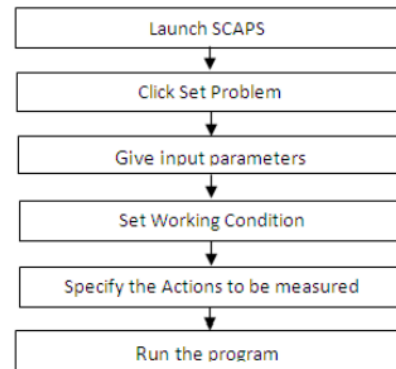


FIGURE 2 Flow chart simulation of SCAPS 1-D

SCAPS is a window application program, developed at the University of Gent with lab windows/CVI of the national instrument. The program organized in a number of panels in which the user can set the parameters or in which the results are calculated. SCAPS analyses the physics of the model and it explains the recombination profiles, electric field distribution, carrier transport mechanism and individual current densities (Mandadapu 2017). The simulation of FeS₂ followed as mentioned by flow chart in FIGURE 2. To find out the best performance of solar cell, the optimum parameter of FeS₂ must be used and find out by using the simulation proses. The simulation set working condition 300 °K as the temperature and 1x10⁶ Hz frequency and 1000 Wm⁻² power of solar energy from the sun. The simulation will determined the performance FeS₂ by manipulate the variable of thickness, acceptor density, band gap and acceptor density of FeS₂ by using the most optimum value. Lastly, numerical modelling for n-type semiconductor to achieve a high efficiency by manipulate it donor density.

RESULTS AND DISCUSSION

Optimum Parameter

The simulation will find out optimum value parameter by manipulated the acceptor density and the thickness of FeS₂. It simulated from 100 μm until 1000 μm with the difference 100 μm for each simulation while the acceptor density we are using $1 \times 10^{13} \text{ cm}^{-3}$ until $1 \times 10^{18} \text{ cm}^{-3}$ with difference $1 \times 10^5 \text{ cm}^{-3}$ for each simulation.

	Acceptor Density NA (cm^{-3})	Thickness (μm)
η (%)	1×10^{16}	900
FF (%)	1×10^{16}	900
J_{sc} (mA/cm^2)	1×10^{16}	200
V_{oc} (V)	1×10^{16}	400

TABLE 2 Optimum parameter for acceptor density and the thickness.

Table 2 show the optimum value of acceptor density and thickness for performance of FeS₂. From the simulation 900 μm is the optimum value should use to get the good value of the performance. When the thickness increases the efficiency and fill factor of FeS₂ likely to get a higher value. For the acceptor density, $1 \times 10^{16} \text{ cm}^{-3}$ show the best result of performance of the solar cell. The 900 μm of thickness and $1 \times 10^{16} \text{ cm}^{-3}$ of acceptor density will be remain and use for the next simulation.

Next, the optimum parameter from previous simulation will be remain for find out the next optimum value for FeS₂. The simulation proses into next step by manipulated the value of parameter of band gap and electron mobility. To find the optimum value, the simulation started by using a band gap from 0.8 eV until 1.3 eV with difference 0.1 eV for each simulation and electron mobility from $1.5 \times 10^2 \text{ cm}^2/\text{Vs}$ until $4.0 \times 10^2 \text{ cm}^2/\text{Vs}$ with difference $0.5 \times 10^2 \text{ cm}^2/\text{Vs}$ for each simulation.

	Electron Mobility (cm^2/Vs)	Band Gap (eV)
η (%)	1.50×10^2	1.3
FF (%)	1.50×10^2	1.3
J_{sc} (mA/cm^2)	4.0×10^2	0.8
V_{oc} (V)	1.50×10^2	1.3

TABLE 3 Optimum parameter for electron mobility and band gap of FeS₂.

Table 3 show the optimum value of the electron mobility and band gap for each factor. From the result, $1.50 \times 10^2 \text{ cm}^2/\text{Vs}$ of electron was the optimum value for electron mobility since it promising the high value of efficiency, fill factor and open-circuit voltage except for short circuit current

density. The lower the electron mobility will result the good performance. As for the band gap, the higher the band, the good the performance. From the simulation 1.3 eV of band gap also promising the high value of efficiency, fill factor and open-circuit voltage except for short circuit current density same as electron mobility.

Numerical Modelling

To achieve the high efficiency in solar cell. The next step is produced a numerical modeling toward the n type semiconductor which is CdS. To boost the performance of solar cell FeS₂ to optimum. The donor density of CdS will be the parameter will be simulated. The value will be simulated from $1.0 \times 10^{15} \text{ 1}/\text{cm}^3$ until $1.0 \times 10^{20} \text{ 1}/\text{cm}^3$ with differences $1.0 \times 10^5 \text{ 1}/\text{cm}^3$ for each simulation.

Donor density ($1/\text{cm}^3$)	η (%)	FF (%)	J_{sc} (mA/cm^2)	V_{oc} (V)
1.0×10^{15}	9.91	51.02	32.3804	0.6002
1.0×10^{16}	10.54	55.93	32.3632	0.5821
1.0×10^{17}	13.57	75.77	31.8283	0.5627
1.0×10^{18}	12.04	76.31	27.9373	0.5646
1.0×10^{19}	11.92	76.34	27.6370	0.5648
1.0×10^{20}	11.88	76.35	27.5444	0.5648

TABLE 4 Optimum parameter for donor density of CdS.

Table 4 show the result of simulation of changing the value of donor density. From the simulation the higher efficiency recorded is 13.57 % by using $1.0 \times 10^{17} \text{ (1}/\text{cm}^3)$. The high value of donor density used, the high value of fill factor will produced but inverserly toward volatge open circuit. As the objective is to get the higher efficiency of FeS₂. The value $1.0 \times 10^{17} \text{ (1}/\text{cm}^3)$ will consider as the suitable value use to increase the performance of FeS₂.

Performance of FeS₂

The simulation proses have develop the new optimum value parameter used to increasing the performance of thin film solar cell FeS₂. As result it show some improvement toward solar cell of FeS₂. The simulation has proven some parameter will give a huge effect toward performance FeS₂.

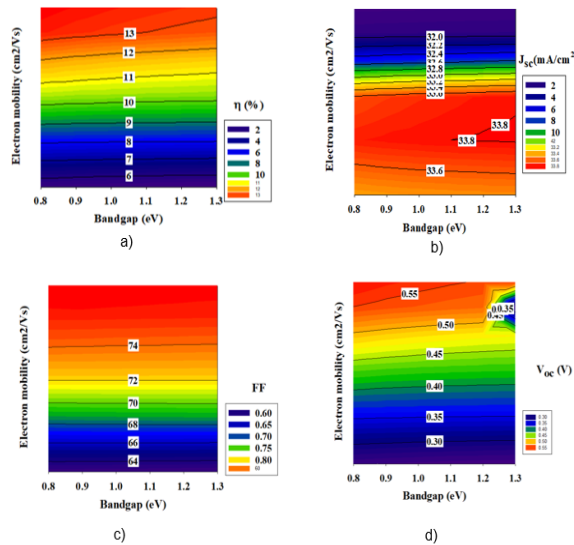


FIGURE 2. (a) Absorption spectra of ZnO, (b) $\text{ZnMn}_{0.05}\text{O}$ and (c) $\text{ZnMn}_{0.10}\text{O}$.

Figure 2 show the spectrum graph for each electric characteristic of FeS_2 . The final result recorded the efficiency was 13.57%, fill factor is 75.77%, 31.82838 mA/cm^2 for J_{SC} dan 0.5627 V for V_{OC} . The result from simulation have shown the improvement toward FeS_2 . As mentioned before the higher efficiency of pyrite that have been required is 2.8% which is a little bit lower for the thin film solar cell with a good absorption coefficient. From the simulation the efficiency have improvent to 13.57 % but still it shown a huge difference towards the theoretical value which is up to 25 %. The high V_{oc} produce from the simulation have causes the high of J_{SC} in FeS_2 .

CONCLUSION

As a conclusion from the journal that have been study the simulation toward FeS_2 have shown some improvement toward its performance. Each parameter that have been used is the logical value from the articles and some is from the modification of FeS_2 which defect FeS_2 . The pyrite solar cell having the architecture $\text{Al:ZnO/FeS}_2/\text{CdS}$ is designed and analyzed using Solar cell capacitance simulator. Absorber layer thickness, acceptor density, band gap and electron mobility influence on the performance of the solar cell are investigated and the numerical modelling have shown effect on the PV, characteristics are observed.

ACKNOWLEDGEMENT

The authors would like to thank Prof Madya Dr Badariah Bais and Dr Puvaneswaran A/L Chelvanathan from Solar Energy Research Institute

(SERI), Universiti Kebangsaan Malaysia for their moral support, knowledge provided and also for their technical support.

REFERENCES

- Altermatt, P. P., Kiesewetter, T., Ellmer, K. & Tributsch, H. 2002. Specifying targets of future research in photovoltaic devices containing pyrite (FeS_2) by numerical modelling. *Solar Energy Materials and Solar Cells* 71(2): 181–195. doi:10.1016/S0927-0248(01)00053-8
- Bhandari, K. P., Tan, X., Zereshki, P., Alfadhili, F. K., Phillips, A. B., Koirala, P., Heben, M. J., et al. 2017. Thin film iron pyrite deposited by hybrid sputtering/co-evaporation as a hole transport layer for sputtered CdS/CdTe solar cells. *Solar Energy Materials and Solar Cells* 163(January): 277–284. doi:10.1016/j.solmat.2017.01.044
- Hossain, E. S., Chelvanathan, P., Shahahmadi, S. A., Sopian, K., Bais, B. & Amin, N. 2018. Performance assessment of Cu_2SnS_3 (CTS) based thin film solar cells by AMPS-1D. *Current Applied Physics* 18(1): 79–89. doi:10.1016/j.cap.2017.10.009
- Liu, T. L. & Zhang, J. M. 2020. Feasibility of band gap engineering of iron pyrite (FeS_2) by codoping Os, Ru or Zn together with O. *Materials Chemistry and Physics* 244(October 2019): 122742. doi:10.1016/j.matchemphys.2020.122742
- Luo, L., Luan, W., Yuan, B., Zhang, C. & Jin, L. 2015. High Efficient and Stable Solid Solar Cell: Based on FeS_2 Nanocrystals and P3HT: PCBM. *Energy Procedia* 75: 2181–2186. doi:10.1016/j.egypro.2015.07.368
- Mandadapu, U. 2017. Simulation and Analysis of Lead based Perovskite Solar Cell using SCAPS-1D. *Indian Journal of Science and Technology* 10(1): 1–8. doi:10.17485/ijst/2017/v11i10/110721
- Rahman, M., Boschloo, G., Hagfeldt, A. & Edvinsson, T. 2020. On the Mechanistic Understanding of Photovoltage Loss in Iron Pyrite Solar Cells. *Advanced Materials* 32(26). doi:10.1002/adma.201905653
- Uchiyama, S., Ishikawa, Y., Kawamura, Y. & Uraoka, Y. 2016. Numerical modeling of device structure for FeS_2 thin film solar cells. *Proceedings of AM-FPD 2016 - 23rd*

*International Workshop on Active-Matrix
Flatpanel Displays and Devices: TFT
Technologies and FPD Materials* 215–218.
doi:10.1109/AM-FPD.2016.7543671

- Xiao, P., Fan, X. L., Liu, L. M. & Lau, W. M.
2014. Band gap engineering of FeS₂ under
biaxial strain: A first principles study.
Physical Chemistry Chemical Physics 16(44):
24466–24472. doi:10.1039/c4cp03453h
- Yu, P., Qu, S., Jia, C., Liu, K. & Tan, F. 2015.
Modified synthesis of FeS₂ quantum dots for
hybrid bulk-heterojunction solar cells.
Materials Letters 157: 235–238.
doi:10.1016/j.matlet.2015.05.033
- Zhang, X., Scott, T., Socha, T., Nielsen, D.,
Manno, M., Johnson, M., Yan, Y., et al.
2015. Phase Stability and Stoichiometry in
Thin Film Iron Pyrite: Impact on Electronic
Transport Properties. *ACS Applied Materials
and Interfaces* 7(25): 14130–14139.
doi:10.1021/acsami.5b03422

Stroke Monitoring System using The Microwave Imaging System

(Sistem Pemantauan Strok Menggunakan Sistem Pengimejan Gelombang Mikro)

Nurrol Athirah Mohamad, Norbahiah Misran, Mohammad Shahidul Islam, Mohammad Tariqul Islam

Department of Electrical, Electronic and Systems Engineering,
Faculty of Engineering & Built Environment, Universiti Kebangsaan Malaysia, Malaysia

*Corresponding author: nurrolathirah7727@gmail.com

ABSTRACT

Stroke or known as brain attack is a disease that is becoming more prevalent now after a heart attack. Stroke is a serious injury to the brain that can cause fatal. Computed tomography (CT) and magnetic resonance imaging (MRI) are the introduced machines in line with technological advances in the field of medicine, but they were inefficient in terms of radiation generation that endangered the patients and impractical large size. The operating costs for both are high and not suitable for continuous monitoring sessions especially for the underprivileged. Thus, microwave imaging technology emerged as a user-friendly technology. Low cost, medium size, portable, safe and its waves are able to penetrate the tissue layers are among the advantages of microwave technology. This study aims to develop a stroke monitoring system that is more effective than existing systems as well as evaluate and validate the performance of the system. A 3D antenna model of a folded structure with a PEC type wall with dimensions of $70 \times 30 \times 14 \text{ mm}^3$ is modelled in a CST Microwave Studio 2019 with frequency operation of 1-3 GHz. The Hugo head model, hemorrhagic stroke elements and nine antenna array elements were integrated in the simulator. The obtained scattering parameters were collected and then analyzed for image reconstruction process using existing algorithms. The antenna showed a consistent directional radiation with the gain of 5.31 dBi and the simulations on the nine elements of the antenna array showed the reflection coefficients for the transmitter antenna and the receiver antenna are below -10 dB and -20 dB, respectively. The image formed is clear and sharp because the noise interference obtained is minimal. Overall, the developed system has the capability in detecting hemorrhagic stroke accurately in the head phantom model by using a microwave system.

Keywords: Haemorrhagic; microwave imaging; image reconstruction

ABSTRAK

Strok ataupun serangan otak adalah penyakit yang makin berleluasa kini selepas serangan jantung. Strok merupakan kecederaan serius pada otak yang boleh membawa maut. Tomografi berkomputer (CT) dan pengimejan resonans magnetik (MRI) adalah mesin yang diperkenalkan selaras dengan kemajuan teknologi dalam bidang perubatan tetapi ia tidak efisien dari penghasilan radiasinya yang membahayakan pengguna dan saiz besar yang tidak praktikal. Malah kos operasi untuk keduanya adalah tinggi dan tidak sesuai untuk sesi pemantauan yang berterusan terutamanya bagi golongan yang tidak berkemampuan. Oleh itu, teknologi pengimejan gelombang mikro muncul sebagai sebuah teknologi mesra pengguna. Berkos rendah, bersaiz sederhana, mudah alih, selamat dan gelombangnya mampu menembusi lapisan tisu adalah antara kelebihan teknologi gelombang mikro. Kajian ini bertujuan untuk membangunkan sistem pemantauan strok yang lebih efektif daripada sistem yang sedia ada kemudian menilai dan mengesahkan prestasi sistem. Model antena 3D struktur berlipat bersama dinding jenis PEC berdimensi $70 \times 30 \times 14 \text{ mm}^3$ dibangunkan di dalam pensimulasi CST 2019 dengan operasi frekuensi 1-3 GHz. Model fantom kepala Hugo, elemen strok hemoragik dan sembilan elemen tatasusunan antena disatukan di dalam simulator. Parameter serakan yang diperolehi dikumpul kemudian dianalisis untuk proses pembentukan semula imej dengan menggunakan algoritma sedia ada. Antena menunjukkan kriteria arah radiasi yang konsisten dengan nilai gandaan sebanyak 5.31 dBi dan simulasi pada sembilan elemen tatasusunan antena menunjukkan pekali pantulan untuk antena pemancar dan antena penerima masing-masing di bawah -10 dB dan -20 dB. Imej yang terbentuk adalah jelas dan tajam kerana gangguan hingar yang diperolehi adalah minimal. Keseluruhannya, sistem yang dibangunkan mempunyai keupayaan dalam mengesan strok hemoragik dengan tepat dan jelas didalam model fantom kepala dengan menggunakan sistem gelombang mikro.

Kata Kunci: Hemoragik; pengimejan gelombang mikro; pembentukan semula imej

INTRODUCTION

Older age, diabetes, high cholesterol, high blood pressure and atrial fibrillation are among the factors the risk of stroke attack its prey. A stroke occurs when the blood flow to a part of the brain is interrupted. Blood flow is interrupted when the blood vessels in the head clogged or broken. Without a blood supply, brain cells can be damaged. Ischemic and hemorrhagic as shown in Figure 1 are the typical types of strokes. The cause of ischemic stroke is a blood clot in the arteries that supply blood to the brain, whereas the cause of hemorrhagic stroke is a rupturing of a blood vessel, resulting in bleeding and increased pressure in the brain. Stroke can be fatal or permanent disability problems if not treated promptly.

For the treatment and rehabilitation of patients, an effective diagnosis is crucial. Thus, head imaging is a critical component in ensuring the affected patient's recovery through timely treatment and on-the-spot detection. In medical diagnostic imaging system, now doctors rely on the system more advanced diagnostic devices such as Computed Tomography (CT) scans and Magnetic Resonance Monitoring Imaging (MRI) for diagnostic and examination purposes (Sohani et al. 2019). However, they are costly, expose patients to dangerous radiation, difficult to access in remote areas, and not affordable to everyone. The size of existing imaging devices makes it difficult for pandemic teams to transport them to specified locations for diagnosis purposes.

Nowadays, microwave technology is the main focus research in medical imaging applications. It has a variety of positive criteria among them, the non-ionized radiation, which is safe at any ages, affordable cost, medium size and portable. Microwave-based imaging is different when compared to techniques traditional imaging i.e., CT scans and MRI. The MWI technique is about detecting differences in the dielectric properties of healthy tissue and diseased tissue.

This technique is safer compared to the use of ionizing radiation which can endanger the patient.

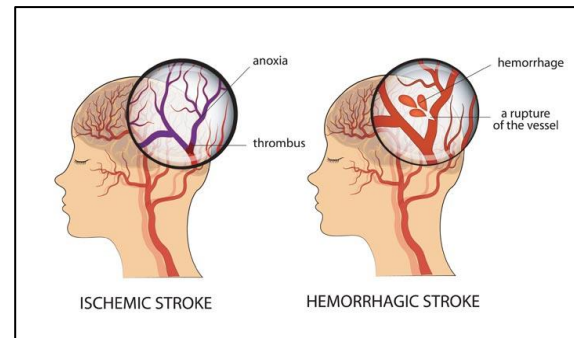


FIGURE 1: Ischemic and hemorrhagic stroke
Source: (Tan 2019)

The use of wideband EM imaging in the diagnosis of breast cancer and the detection of brain damage has become commonplace. The antenna is the most important part of the EM head imaging system. The antenna array sends out a low-level EM signal in the direction of the human head. Then the scattered signal is collected and processed using a variety of algorithms in order to reconstruct the interior of the human head and pinpoint the injuries. To detect and recreate the images, the variations in electrical properties between normal and diseased heads are used.

Many studies in the past literature focus on system performance on detecting the stroke. Table 1 shows six studies with different objectives conducted on the interaction between the system and the type of stroke detection. Based on Table 1, the type of hemorrhagic stroke is the component that frequently studied by the researcher. Only three studies were carried out on the ischemic stroke. According to Table 1, these studies are related to different dielectric properties between the healthy head tissue and dielectric properties of ischemic and hemorrhagic stroke.

TABLE 1: Investigation on system interaction

No	Reference	Stroke Elements	
		Ischemic	Haemorrhagic
1	Karadima et al. (2020)	x	x
2	Pokorny et al. (2019)	x	x
3	Merunka et al. (2019)		x
4	Scapaticci et al. (2018)		x
5	Hopfer et al. (2017)	x	x
6	Bialkowski & Ireland (2011)		x

Stroke can be detected when there is a difference in dielectric between damaged tissue and normal human head tissue. Stroke is a blood vessel disorder that can cause damage to tissues. Thus,

stroke will be detected through the tissue damage produced. In terms of antenna setup and image reconstruction, researchers are now proposing numerous techniques for EM head imaging. Sohani

et al. (2020) shows a triangular patch antenna with two antenna array elements for obtaining the scattering signals that limit the ability to reconstruct images. While Alqadami et al. (2020) describes a flexible antenna for EM head imaging that concentrates primarily on scattering parameters and fidelity factor rather than image reconstruction, a head phantom with tissue mimicry is required to confirm antenna performance. Algorithm for ICH image detection presented in Mobashsher et al. (2016) is not well detected even though data acquisition process is quite fast. Following various studies conducted by researchers, many weaknesses have been identified.

In UKM the research on head imaging system have been conducted on prototype and computerized simulators. Previous research by Hossain et al. (2020) conducted shows the simulation analysis on the head model and it focuses on scattering parameters and performance factors of the antenna model compared to the formation stroke image. Low gain and inconsistent radiation direction at the antenna causing the performance and capabilities of existing systems to decrease. Low gain due to high energy loss during signal reflection occurs as well as the influence of the antenna model structure. This limitation causes stroke detection in the head will be disrupted and improvements on the model antennas need to be done to increase the effectiveness of head imaging systems.

The purpose of this study is to investigate the capabilities of the antenna model on stroke detection. The antenna model developed by modification from the existing antenna model and research paper from Hossain et al. (2020) and Shahidul Islam et al. (2021) are referred. Besides, it also aims to detect stroke's location accurately and to obtain the image reconstruction using the existing algorithm more clearly. Basically, this paper is about the performance evaluation of a system modeled in a computer simulation by detect stroke more effectively.

METHODOLOGY

Antenna Design

The single antenna modeled is a 3D type antenna with PEC type walls on both sides and bottom of the antenna. The optimum dimensions of a single antenna are $70 \times 30 \times 14 \text{ mm}^3$ and 1.57 mm thickness of Rogers RT5880 is used as an antenna substrate where the relative permittivity and loss tangent of the material is 2.2 and 0.0009, respectively. The antenna patch and ground have same dimension which is responsible to control the high resonant frequencies of the antenna. The antenna model and its parameter are shown in Figure 2 and Table 2. The antenna's properties are

designed and analyzed using CST, a frequency domain-based EM simulator software.

Nine elements antenna array of a circle - configured modeled using the same nine single antennas as developed in Figure 3. The coordinates and the distance between the antennas should be thoroughly scrutinized as it gives effect on simulation. The angle of each antenna is 40° to form round structured antenna array.

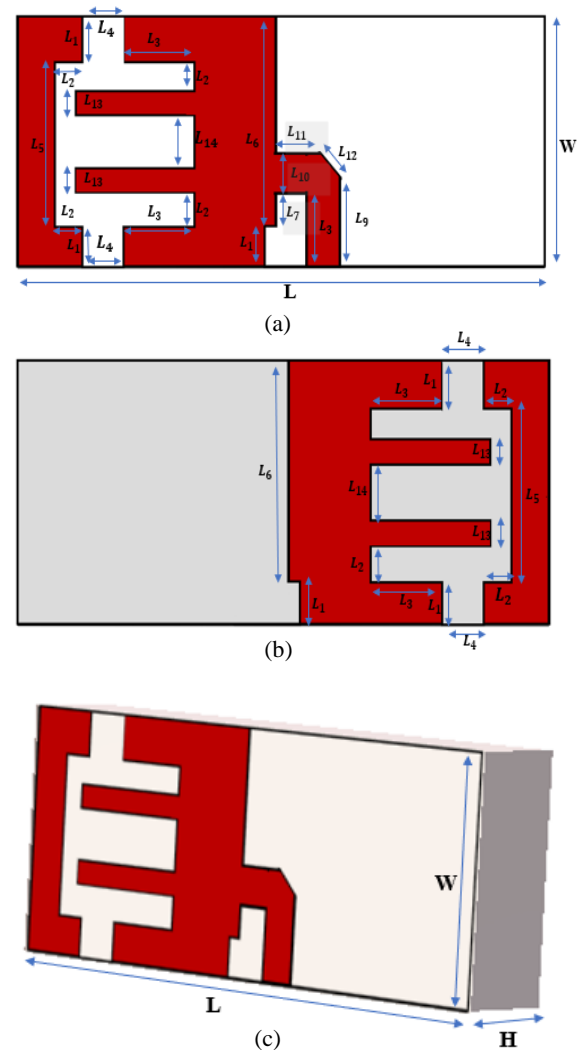


FIGURE 2: Antenna model (a) front view, (b) bottom view and (c) perspective view

TABLE 2: Antenna parameter

Parameter	Size(mm)	Parameter	Size(mm)
W	30	L_8	9
L	70	L_9	11
L_1	5	L_{10}	4.2
L_2	3.5	L_{11}	7.5
L_3	9	L_{12}	3.38
L_4	5.5	L_{13}	3
L_5	20	L_{14}	10
L_6	25	H	14
L_7	4		

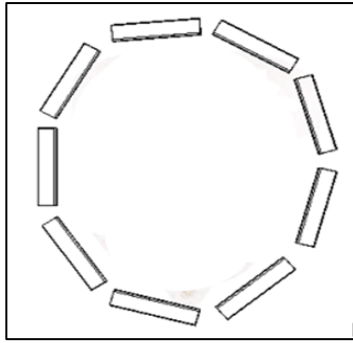


FIGURE 3: Nine elements antenna array

Head Phantom Model and Hemorrhagic Element

The human head has several layers such as skin, fat, skull, gray matter, white matter, CSF, and blood (hemorrhagic stroke). Each element has their own tissue layer thickness, dielectric properties, and electrical conduction. Developing the Hugo head phantom model must have the properties and criteria that similar to a real human head. This is to analyze the antenna performances and test its effectiveness to detect hemorrhagic stroke in the head human. To obtain the dielectric accuracy and thickness of the tissue layer, analysis of several men head at various ages was carried out. The result, thickness tissue for the skin is from 0.5-1.5 mm and the skull is 3-11 mm. The dielectric properties of head tissues are given in Table 3.

TABLE 3: Dielectric of head tissues

Tissue type	Relative permittivity (ϵ_r)	Conductivity (S/m)
Fat	5.46	0.051
Skull	12.45	0.143
Skin	43.75	0.856
CSF	68.64	2.413
Gray Matter	52.73	0.942
White Matter	38.89	0.591
Blood	61.36	1.538
Hemorrhagic	68.0	5.34

Six layers of tissue of Hugo head phantom with radius of 100 mm placed at the center of the antenna array with the distance between the arrangement of the antennas and the layer of skin tissue is 15 mm as shown in Figure 4.

The nine-element antenna array of 3D antenna, Hugo head phantom model and hemorrhagic stroke element were combined and developed into CST Suite Studio 2019 software for further analysis. Thus Figure 5 shows the flowchart of the whole system operation.

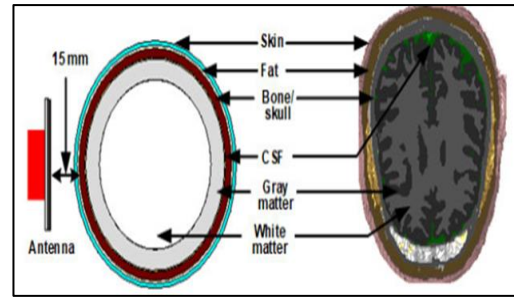


FIGURE 4: Cross section of head model
Source: (Hossain et al. 2020)

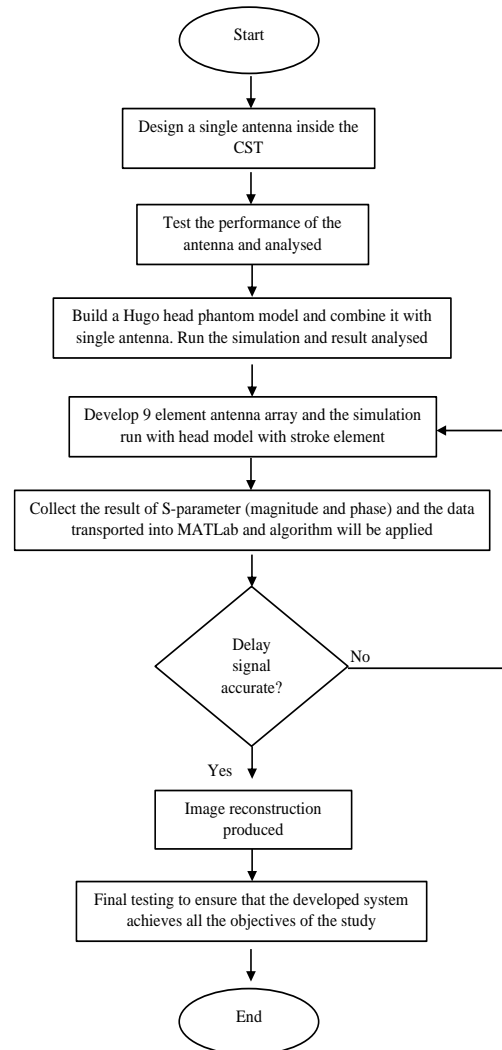


FIGURE 5: Flowchart of the whole system operation

From the flowchart given in Figure 5, the analyzing process occur when the result of the simulation has been done on the CST. The gain, s-parameter and reflection coefficient are be observed and recorded. The best antenna performance should produce a gain value higher than 4 dBi, radiation should be directional, and the reflective coefficient of s-parameter must below than -10 dB. Otherwise, it will affect the result

because while analyzing the data it may show nothing or very high distortion and will facing the difficulties on imaging process. Two conditions of Hugo head phantom model are tested to obtain the capability of antenna to penetrate the tissue layers and hemorrhagic stroke.

Image reconstruction

The images are reconstructed using a modified delay and sum technique. This existing IC-CF-DMAS algorithm are tested, and it gives the high resolution of image, low noise on image reconstruction, stroke detection is accurate, sharp and clear. The flow of the reconstruct image is shown in Figure 6.

Simulation result for s-parameter of nine elements antenna array is used for the analysis of microwave signal contrast and to construct the image. The magnitude and phase of the antennas are collected by using one antenna transmitter and other eight as receivers. The resulting s-parameter from antenna array simulation divided into two namely S_{odd} and S_{even} . The Inverse Fourier Transform is then used to transform the S_{odd} signal into time-domain mode. After that, the time domain signal is processed to reconstruct the images by applying the IC-CF-DMAS algorithm. The delay

signal is produced by getting signal from transmitting antenna and receiving antenna in the antenna array. Numerical data is received as algorithm output, then the data is transport into OriginPRO software to develop the image of the head.

Testing and validation

Three sets of image reconstruction scenario were used in the system for testing and validation. The imaging on clear head without any stroke element is the first set, and this can be used to determine the imaging area covered by the developed model. Second one is the image on the head model with element stroke, this is to determine the location of the stroke in the head. The third set is the image on the head model with stroke element. This is to determine the antenna performance and radiation while detecting the hemorrhagic stroke accurately. The three sets of imaging compared and concluded.

There are two contour graphs that have been generated, one for the head model without stroke and the other for the head model with stroke. Both graphs are compared to make sure if the bleeding has been captured at its exact location.

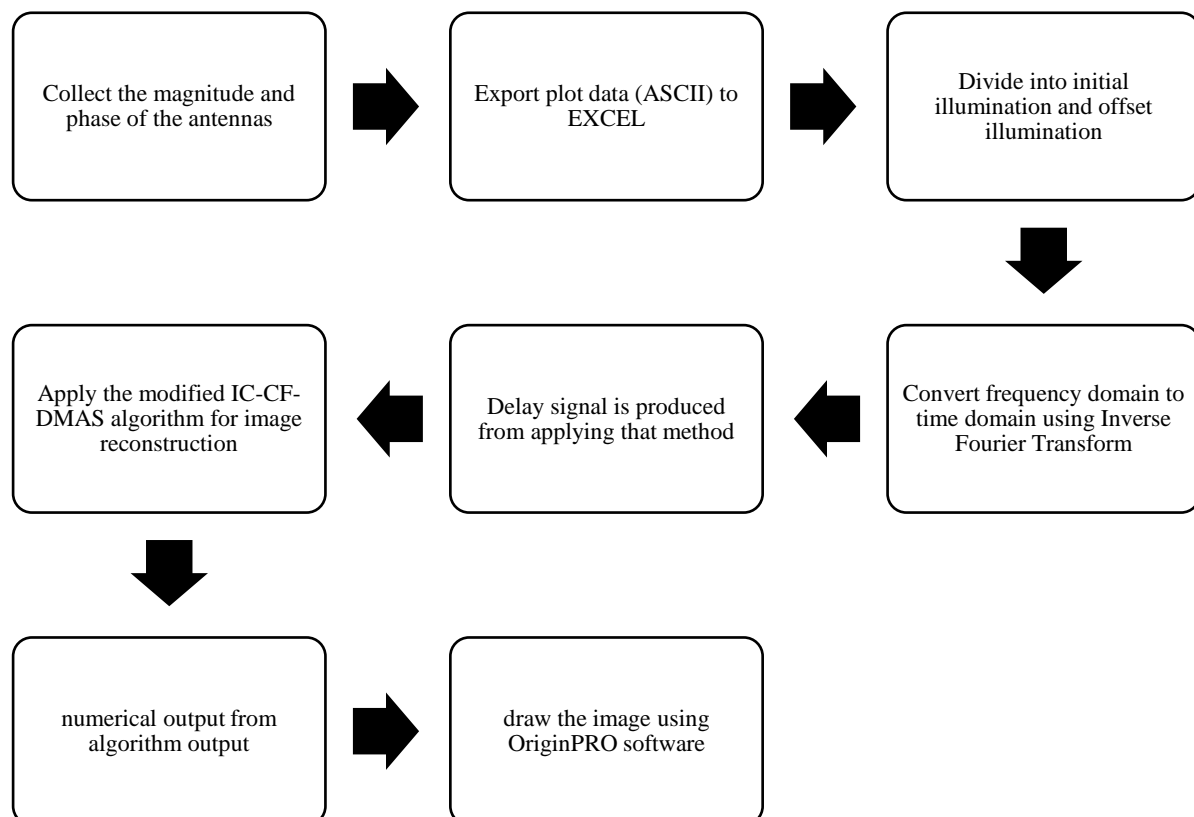


FIGURE 6: The flow of image reconstruction

RESULT AND DISCUSSION

Antenna Analysis

The antenna is modelled using the given parameter in Table 2. Several references are used as the comparison on antenna performance. The antenna is developed by the modification on the existing antenna prototype in UKM. The analysis is done by running the simulation using the CST Microwave Suite Studio 2019.

The response of the scattering parameter or known as the s-parameter is a measure reflected energy and radiated energy in microwave filters. It is measured by a VNA is connected to the developed system model. VNA able to separate the emitted and reflected energy using a directed coupler for the measure of power. Generally, s-parameter is used to identify the operating frequency of antenna. The operating frequency has been optimized to be 1 GHz to 3 GHz. It is determined by the frequency range in which the antenna operates when the signal level falls below -10 dB, which means that only 10% of the input power is reflected by the antenna, and the rest is delivered completely.

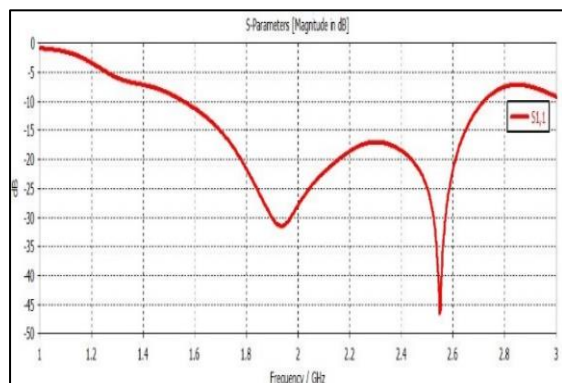


FIGURE 7: Scattering parameter

The scattering parameter of the antenna which is represented in Figure 7 shows the reflective coefficient under -10 dB and the highest scattering parameter is -46.12 dB at 2.55 GHz. The antenna functions in the frequency range of 1.58 GHz to 2.74 GHz, according to the simulation.

Next is the simulating the gain of the antenna and realized gain are presented in Figure 8. The term "realized gain" refers to a gain calculation that includes losses due to reflection and losses due to the antenna structure. The simulated on the antenna design shows the maximum gain of 5.31 dBi at 2.6 GHz.

The 3D radiation pattern is analyzed with far field radiation characteristic at 1.94 GHz and 5.55 GHz respectively. The simulated result shown in Figure 9. The antenna exhibits a consistent

directional radiation characteristic at the specified frequencies, with an average gain of 4.92 dBi.

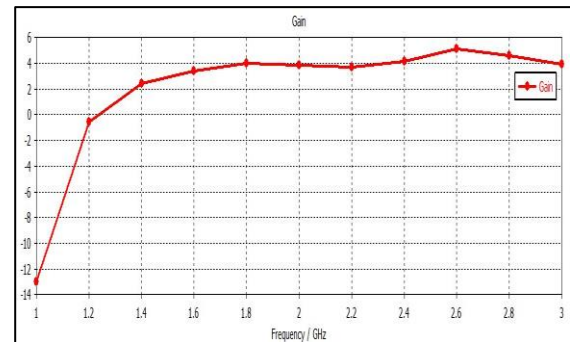
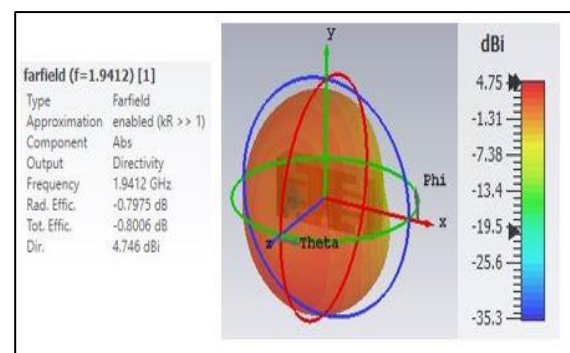
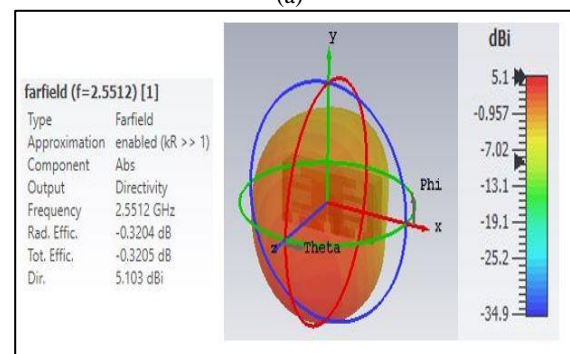


FIGURE 8: Realized gain



(a)



(b)

FIGURE 9: 3D radiation pattern

Head model and stroke element analysis

The Hugo head phantom is developed according to the parameters set in Table 3, then hemorrhagic stroke is developed in spherical shape with radius of 15 mm, placed inside the head phantom to test the radiation level of the antenna in detecting stroke. A single antenna is positioned at a 90° angle from the head model's center.

The analysis is carried out on the antenna scattering parameters on the two conditions of head model which is with or without the stroke element. A single antenna's scattering parameter that is 15 mm away from the head model is presented in Figure 10. The simulation s-parameter for both

condition of head models shows the reflective coefficient continuously remain below -10 dB but different in reflection coefficient value and frequency value.

The reflection coefficient value of head model with stroke is -45.2 dB at 1.92 GHz while the reflection coefficient of model without stroke is -32.6 dB at 2 GHz. So, the head model with stroke gives the lowest reflection coefficient at the lowest frequency.

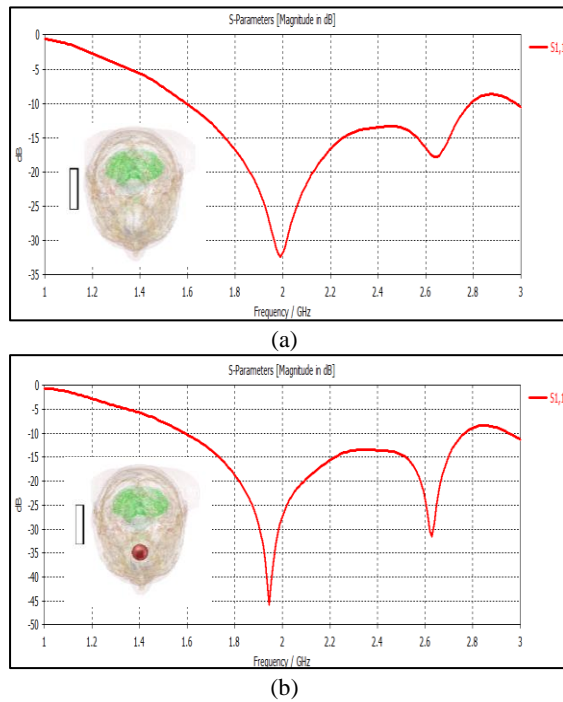


FIGURE 10: Scattering parameter on head model (a) without stroke and (b) with stroke

Figure 11 represents the setup of nine elements of antenna array with their scattering parameter. The first antenna is a transmitter while the other eight are receiver. The scattering parameter shows the reflective coefficient for both transmitting and receiving antenna are remain below -10 dB and -20 dB respectively.

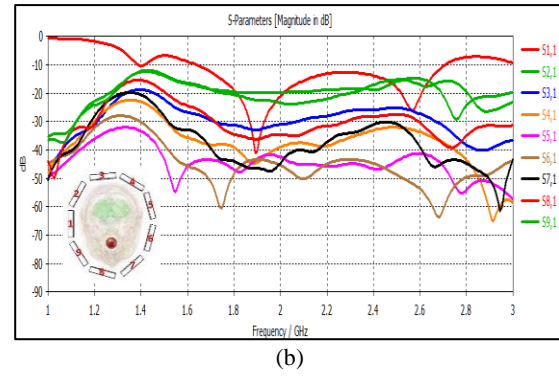
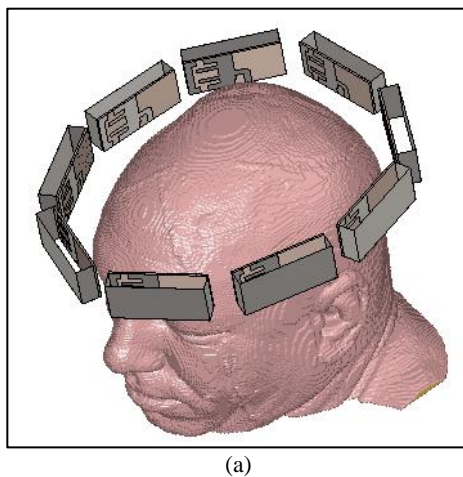


FIGURE 11: Nine element antenna setup with (a) perspective view and (b) scattering parameter

Image reconstruction analysis

Three sets of image reconstruction have been executed for analysis on system model validation. The flow of reconstructing the image has been followed as Figure 6.

Figure 12 represents the first imaging set of clear head without any stroke element. It is observed that the whole contour graph is filled with blue color while the green contour indicates as the antenna radiation in the head model.

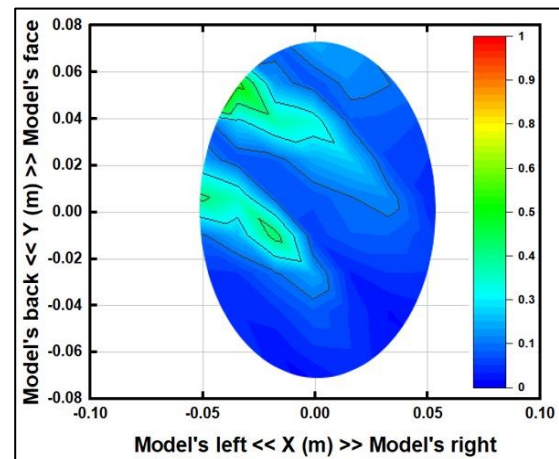


FIGURE 12: Contour graph without stroke element

Figure 13 represents the contour graph with stroke element as mentioned as imaging set two and three. Two different antenna position is placed to test the validation of system model on detecting stroke. The highest contour on the image is shown as the stroke detection. The rectangular red mark shows the hemorrhagic detection on their exact location.

Two different antenna location is the changes of transmitter antenna location in the system. Original location is at the origin of the clockwise rotation while the changes of transmitter antenna is at 180° of the clockwise rotation. The different radiation observed on the contour graph of how the antenna radiated to detect stroke element.

The stroke is detected clearly with the highest color contour in the graph.

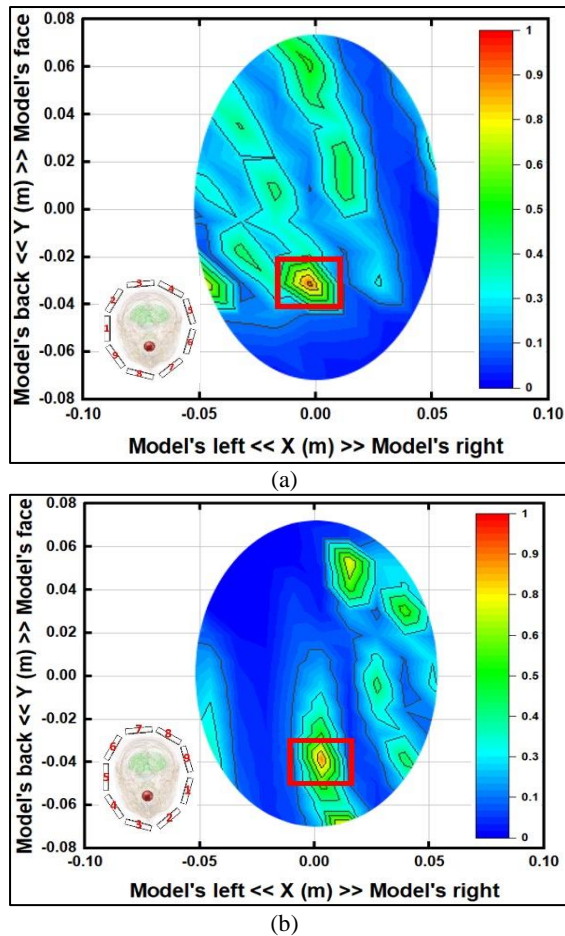


FIGURE 13: Contour graph with element stroke (a) original antenna location and (b) different antenna location

CONCLUSION

The model of stroke monitoring system is presented using $70 \times 30 \times 14 \text{ mm}^3$ dimensions of 3D antenna type with folded structured. The design of the patch and ground in same dimension, which is to enhance the antenna performance in directionality, gain and accurately in imaging. The antenna model achieves realized gain of 5.31 dBi, within the frequency range 1 GHz to 3 GHz, also achieving stable performances. Besides, the antenna also gives the stable far field radiation pattern within the stated operational frequency. The nine elements of antenna array, dielectric constant of head tissues and hemorrhagic stroke, algorithms, and post-processing of the scattered signals are the main components to the head imaging system. The 3D antenna is validated by using it with a head model phantom and using the IC-CF-DMAS technique to reconstruct the image and immediately detect the hemorrhagic stroke. The location of the stroke was determined by the highest contour in the

imaging graph. The stroke location is identified since the executed images are brighter and sharper in color. As a result of the reconstructed images, the system model appears to be a potential strategy for detecting the early stage of brain hemorrhages in a portable EM imaging system for the head.

ACKNOWLEDGEMENT

I would like to thank the Microwave Technology Laboratory and the Department of Electrical, Electronic and Systems Engineering, Universiti Kebangsaan Malaysia for their support and assistance in completing this study.

REFERENCES

- Alqadami, A.S.M., Nguyen-Trong, N., Mohammed, B., Stancombe, A.E., Heitzmann, M.T. & Abbosh, A. 2020. Compact Unidirectional Conformal Antenna Based on Flexible High-Permittivity Custom-Made Substrate for Wearable Wideband Electromagnetic Head Imaging System. *IEEE Transactions on Antennas and Propagation* 68(1): 183–194.
- Bialkowski, M. & Ireland, D. 2011. Microwave Head Imaging for Stroke. *Progress In Electromagnetics Research* 21(August): 163–175.
- Hopfer, M., Planas, R. & Hamidipour, A. 2017. Tomography for Detection , Differentiation , and Monitoring of Brain Stroke. *IEEE Antennas and Propagation Magazine* (October): 86–97.
- Hossain, A., Islam, M.T., Chowdhury, M.E.H. & Samsuzzaman, M. 2020. A Grounded Coplanar Waveguide-Based Slotted Inverted Delta-Shaped Wideband Antenna for Microwave Head Imaging. *IEEE Access* 8: 185698–185724.
- Karadima, O., Rahman, M., Sotiriou, I., Ghavami, N., Lu, P., Ahsan, S. & Kosmas, P. 2020. Experimental validation of microwave tomography with the DBIM-twist algorithm for brain stroke detection and classification. *Sensors (Switzerland)* 20(3): 1–16.
- Merunka, I., Massa, A., Vrba, D., Fiser, O., Salucci, M. & Vrba, J. 2019. Microwave tomography system for methodical testing of human brain stroke detection approaches. *International Journal of Antennas and Propagation* 2019: 1–9.
- Mobashsher, A.T., Mahmoud, A. & Abbosh, A.M. 2016. Portable Wideband Microwave Imaging System for Intracranial Hemorrhage Detection Using Improved Back-projection Algorithm with Model of Effective Head Permittivity. *Scientific Reports* 6(March 2015): 1–16.

- Pokorny, T., Vrba, D., Tesarik, J., Rodrigues, D.B. & Vrba, J. 2019. Anatomically and dielectrically realistic 2.5D 5-layer reconfigurable head phantom for testing microwave stroke detection and classification. *International Journal of Antennas and Propagation* 2019: 1–7.
- Scapatucci, R., Tobon, J., Bellizzi, G., Vipiana, F. & Crocco, L. 2018. Design and Numerical Characterization of a Low-Complexity Microwave Device for Brain Stroke Monitoring. *IEEE Transactions on Antennas and Propagation* 66(12): 7328–7338.
- Shahidul Islam, M., Islam, M.T., Hoque, A., Islam, M.T., Amin, N. & Chowdhury, M.E.H. 2021. A portable electromagnetic head imaging system using metamaterial loaded compact directional 3d antenna. *IEEE Access* 9: 50893–50906.
- Sohani, B., Khalesi, B., Ghavami, N., Ghavami, M., Dudley, S., Rahmani, A. & Tiberi, G. 2020. Detection of haemorrhagic stroke in simulation and realistic 3-D human head phantom using microwave imaging. *Biomedical Signal Processing and Control* 61(1–10): 102001. <https://doi.org/10.1016/j.bspc.2020.102001>.
- Sohani, B., Tiberi, G., Ghavami, N., Ghavami, M., Dudley, S. & Rahmani, A. 2019. Microwave Imaging for Stroke Detection: Validation on Head-mimicking Phantom. *Progress in Electromagnetics Research Symposium 2019-June*: 940–948.
- Tan, I.O. 2019. Recovering with Stroke Rehabilitation | Health Plus. *Mount elizabeth hospitals* <https://www.mountelizabeth.com.sg/healthplus/article/stroke-rehabilitation> [11 July 2021].

Underwater Data Logger Development: Bluetooth Wireless Communication Implementation for Monitoring

(Pembangunan Pengellog Data Bawah Air: Pelaksanaan Komunikasi Tanpa Wayar Bluetooth untuk Pemantauan)

Nurul Izzati Saleh, Iskandar Yahya

Department of Electrical, Electronic and Systems Engineering,
Faculty of Engineering & Built Environment, Universiti Kebangsaan Malaysia, Malaysia
*Corresponding author: izzatisaleh55@gmail.com

ABSTRACT

In the past five years of study in building an underwater data logger, researchers involved a microcontroller-based with sensors and a microSD card. But the main limitations are showing that the recorded parameters are limited while other case, the system diving can only go at most 30 meter and the other case is there is no mentioning on how the recorded file in microSD is required during reading process. Therefore, other alternatives are studied in this study which focuses on its use in underwater environment with maximum depth of 50m with multi-parameter. Wireless communication technique is presented which require recorded file of the parameters in the microSD through Bluetooth on a Bluetooth module HM-10 and a terminal of PuTTY. The main pillar of this system is the Arduino Uno microcontroller along with other sensors such as depth or pressure sensor with built-in temperature sensing called MS5803, salinity sensor TDS SKU: SEN0244, ambient light sensor TEMT6000 and GPS module U-Blox 6M. Robust underwater housings are constructed for this logger using PETG, Cylindrical Acrylic Tube, silicone-based O-Ring and an epoxy This combination turns this logger into a multi-level menu for the users. This paper describes a wide range of parameters to be recorded by a logger in underwater at most 50 meters.

Keywords: *underwater data logger; environmental monitoring; PuTTY; Arduino-based logging platform; harsh environment*

ABSTRAK

Pada lima tahun yang lalu bagi kajian dalam membina pengellog data bawah laut, para penyelidik melibatkan mikrokontroler dengan sensor dan kad microSD. Tetapi batasan utama adalah bahawa parameter yang dirakam adalah terhad sementara kes lain, sistem menyelam hanya dapat mencapai paling banyak 30 meter dan kes lain adalah tidak ada menyebut tentang bagaimana fail yang direkam dalam microSD diperlukan semasa proses membaca. Oleh itu, alternatif lain dikaji dalam kajian ini yang memfokuskan penggunaannya di persekitaran bawah laut dengan kedalaman maksimum 50m dengan multi-parameter. Teknik komunikasi tanpa wayar disajikan yang memerlukan fail parameter yang direkodkan dalam microSD melalui Bluetooth pada modul Bluetooth HM-10 dan terminal PuTTY. Tiang utama sistem ini adalah mikrokontroler Arduino Uno bersama dengan sensor lain seperti sensor kedalaman atau tekanan dengan sensor suhu terbina dalam yang disebut MS5803, sensor salinitas TDS SKU: SEN0244, sensor cahaya ambien TEMT6000 dan modul GPS U-Blox 6M. Perumahan bawah air yang kuat dibina untuk penebang kayu ini menggunakan PETG, Tiub Akrilik Silinder, O-Ring berasaskan silikon dan epoksi Kombinasi ini menjadikan pembalok ini menjadi menu pelbagai peringkat untuk pengguna. Makalah ini menerangkan pelbagai parameter yang akan direkodkan oleh penebang di bawah air paling banyak 50 meter.

Kata Kunci: *pengellog data bawah air; pemantauan persekitaran; PuTTY; Pelantar pengellog berasaskan Arduino; persekitaran yang lasak*

INTRODUCTION

The variation of underwater data logger either made by the industry or researchers are all had the same pattern of giving the basic needs of the definition of this type of logger. To be exact, those systems are included a microcontroller-based which the common is Arduino, with limited sensors which then the readings are recorded into a microSD and the whole system can go down only for 30 meters. The utmost reason of those limitations is because they want to keep a low cost and the investigation or objectives of the system is specific to record one or two underwater parameters which the common are temperature, salinity, and depth. A study conducted by Grant et. al. (2016), Arduino platform was chosen over Raspberry Pi and Gumstix because of its lower price and extensive online support network. Meanwhile, Theodore et. al. (2020), were only used a MS5803 to measure wave characteristics with the open-source Arduino software development environment.

When came to a data logger, it means there are two main processes which are recording and reading the data. Data here may include all the required parameters in the environment whether it is in the air or in the water while in this paper, the subject is in the water or to be specific it is in the tropical sea. Before, it has been stated how the limitations during recording process was seen

Knowledge Gap

Most used material in designing the enclosure of the system is Poly Vinyl Chloride (PVC) because of its ability to be waterproof and resist to chemicals. But it degrades when exposed to Ultraviolet (UV). Till today, researchers for the underwater environment choose to implement this material in their project. Standard PVC pipe is used in the main waterproof housing by Grant et. al. (2016) to develop an Arduino-based Sonde for coastal applications at 4-meter subsurface depths. Meanwhile, the standard PVC is referring to ASTM D1785 which is the Standard Specification for PVC Plastic Pipe that specifically for water distribution and irrigation system.

The cons introduced by the PVC is indeed noted by the researchers and hence some has taken step to do mitigations on that. Patricia et. al. in their Cave Pearl Data Logger (2018), a protective coating of water based exterior latex has been used for the UV exposures while to reduce thermal stress on the electronic components. First to know that

throughout the previous studies where the number of parameters involvement is limited with low consideration of the length of depth that system can go down in water. Hence, the topic to be discussed later is about the methodology to cover the deficiency by introducing strong and waterproof housing and the involvement of variety of sensors. Now, as for the reading process, there is no findings on previous study about the technique to acquire the microSD card from the housing. Since the system is operating in the water environment, it is supposed to be a closed housing with an airtight and watertight capabilities. Instrument use in an underwater camera-TV system (Zhang et. al, 1987) has used a watertight underwater cubicle while it only needs to penetrate the seabed to about 100-150 mm. So, when the microSD card is needed, it is assumed that the closed housing is being opened. The mechanical design of the system housing can include one specific back door for the microSD card which is the same as the GoPro HERO9. It is important to know that it is not good for an airtight and watertight housing to be opened frequently as it will degrades the performance of that water and airtight capabilities over time. As being known in industry that watertight enclosures does not necessarily guarantee long-lasting protection and reliable performance because pressure differentials, which over time can cause leak paths.

latex paints consist of a pigment and binder with water used as a carrier (Kelly, 2019). Water based paint was initially introduced in 1865 when the first patent received by D. P. Flinn. Meanwhile, with the introduction of latex in 1940, the paint industry has been revolutionized and what to be noted here is that the purpose of its early use is its low cost due to a lower ratio of acrylic polymers. But, at the end of the day, the existence of the probability of the paint to not stick to all surfaces will expose the system enclosure to the UV and hence harm the inside electronic components.

Volatile memory has been used since 1984 by M. P. Pearson et. al. which used a tape cassette to store the recorded value of the levels of oxygen, temperature, and underwater light. Till recent, the invention of the volatile memory has been substituted to a non-volatile memory which the common is SD card. In a microcontroller-based such as Arduino, an SD module is required while the size of the SD or microSD card can be within 4 MB till 128 MB. Many studies form a .txt file or .csv file for the recorded parameters stored in the card. But the technique used is not found or

explained when file inside is to be read. Meanwhile, in this paper, it is not focusing in the mechanical design on making back door or separate compartments for the SD card itself. Instead, the lens is going towards the technology of wireless communication during the reading process as it increases the efficiency of the system. In short, the file data is required from the card through a wireless communication and passing through a 'bridge' called terminal to go into a computer. This function will need one more wireless module that compatible to the Arduino.

METHODOLOGY

Data Calibration

Calibration is a comparison between known (standard) measurements and measurements using other instruments. Typically, the accuracy given by the standard needs to be ten times more accurate compared to the accuracy of the instrument being tested. This method is carried out at the first stage in the whole process of building the study system. Such a thing is to identify any uncertainty of the measurement of the past instrument, an analysis can be made whether the deficiency can be fixed because it is due to technical errors or faulty software or even the instrument itself does not have high enough accuracy. Thus, it can be decided on the possibility of switching to other better instruments. As in this study, initially the depth and pressure sensor were MS5540C, but after a testing on the operating limits of the readings given, it was decided to replace it with another sensor that named MS5803.

Referring to the figure below, calibration of the pressure parameters was made by placing the book on top of a balloon containing the MS5803 sensor. Book variations were then added to see the difference in reading output by the sensor. The relation is then made by doing an analysis discussed in the later section. Instead of using a specialized temperature sensor for underwater use, DS18B20, MS5803 is also used to sense temperature as it has a temperature reading function. Further, calibration of the temperature parameter was carried out by contrasting it with the parameters given by the room thermometer. Whereas the variable used is room temperature and not water temperature. This is due to the lack of complete equipment and the pandemic situation that does not allow any meeting with the supervisor, to coat the sensor so that it is waterproof. So, it is possible to measure using room temperature because the difference is only in the density where it is generally known that the

density of water is higher than that of air which then causes the giving of the water temperature to be later than the air temperature. Hence, the water temperature should follow the air temperature or room temperature after a certain time. Another consequence of today's pandemic is that this depth sensor calibration from the same MS5803 cannot be accomplished and that is when an inference has been made in the end by using a relationship with the pressure value in an algorithm used in the programming.

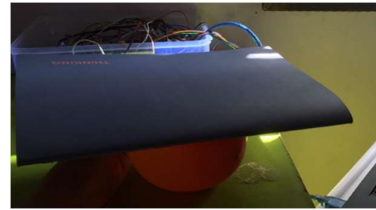


FIGURE 1. Pressure sensor calibration

The TDS SKU: SEN 0244 salinity sensor consists of a probe, is an electric charge (EC) meter in which two electrodes (end probe needle) of equal distance are inserted into water and used to measure the charge. For this study, the sensor was calibrated with different amount of weighted salts. Then, analysis is made with the theoretical statement of the value of salt contained in the reality of the sea in the tropics to justify the ability of the sensor to work well in the targeted environment. Figure 2 explained the calibration for the light intensity sensor, TEMT 6000 which has been made in the comparison with smartphone application 'Lux Light Meter'. The application can measure the illumination of ambient conditions. Initially, the sensor was placed at the same distance as the smartphone that had the app. The first position between the two sensors with the light source from the voltage-powered lamp of three AAA-sized batteries is 50 cm. Lux unit light readings were then obtained and recorded. The position distance of the light source is subsequently varied according to a downward trend.

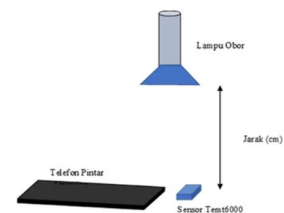


FIGURE 2. TEMT 6000 calibration

The Global Positioning System or GPS is a system for determining the exact geographical

location by the user. In the context of this study, a GPS module namely U-Blox Neo-6M was used to provide and store the location of the system before entering the waters. Then, the calibration of this module is easier because the comparison is only with the location standard given in Google maps that use Landsat 8 satellites.

Bluetooth communication testing

The second phase, development of Bluetooth communication carried out the process of reading data files in the microSD card which parted into two main parts. The first part is about selecting the right Bluetooth module to work in the Arduino Uno platform. Between three Arduino-compatible Bluetooth module; HC-05, HC-06 and HM-10, current consumption, Bluetooth version and sleep mode function are the elements of their differentiation. Then, the chosen module is tested for its performance on the functions required by the system.

Case Study for Multi-Level Menu Construction

A case study was made on the similarity of the case with the construction of the interface menu in this study system. It has involved a case in building a fast-food automated ordering system. Each fast-food menu has a defined price value of each of them. Thus, directly the method has eliminated the use of switch-case techniques in the programming languages involved in the early stages.

Experiment Design and Procedure

The design of the system in this paper is begin with the design of the electronic components. Referring to the Figure 3 below is the connection of all the components with the Arduino that makes one complete system. Firstly, when the system is powered on, the state is waiting for the user input to choose what process to execute either it is reading or recording process. In the meantime, of either one process is executed, the Real Time Clock (RTC) that use DS3231 model is working on in the background which during the recording of the parameter, the time is stamped on the file data. To remind the Bluetooth communication earlier, it is involved during the reading process, and this is where the system is already outside the water environment and there is a connected computer to receive the file data.

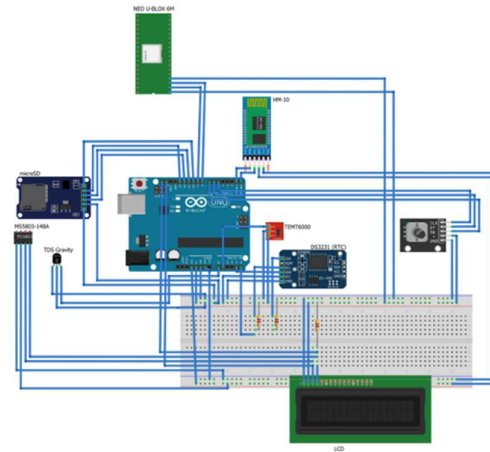


FIGURE 3. System Overview

As for the second design, it is about the mechanical design originated from a drawing on the OnShape platform. The three main materials used in Figure 4 (a) are Polyethylene terephthalate glycol (PETG) for all design columns, Acrylic Cylindrical Tube for the housing wall, and Silicone O-Ring as a liquid or gas ingress barrier. As such, PETG is a thermoplastic polyester that provides chemical resistance, durability, and its excellent capabilities for manufacturing. To further focus on the use of the material in this study, it has been compared with Acrylonitrile Butadiene Styrene (ABS) because of its properties which are also very similar to each other. Thus, the comparisons made are based on durability, temperature resistance, Ultraviolet (UV) radiation resistance, price, and availability, and hygroscopic. Starting with durability, PETG has overtaken ABS due to the stronger PETG adhesion condition compared to ABS which has strong and poor coating adhesion. Therefore, PETG is capable of withstanding underwater as far as high depths and high pressures, as the target is 50 m. As for temperature resistance, ABS can withstand as high as 100 °C while PETG is lower at 80 °C. However, with such a small margin, PETG is more suitable and widely used in electronic applications which coincides with the joint study design of heat - emitting electronic components.

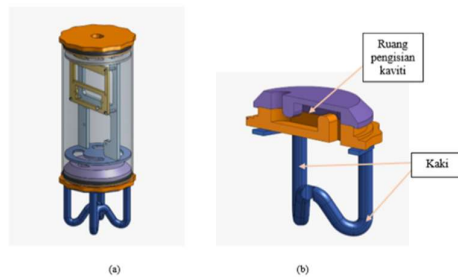


FIGURE 4. System's Mechanical Design
(a) OnShape 3D Design, (b) Bottom view of OnShape 3D Design

Further, PETG is in better condition under UV radiation due to the minimal radiation effect on it compared to ABS. Although the system will be in waters, it should be noted that UV radiation still also enters waters as far as 1000 meter. In addition, the cost of ABS is lower than PETG in addition to the availability of both in the market due to high demand rate. A good comparison for PETG despite having its higher hygroscopic deficiencies thus making it easier to absorb air humidity for example, water. It has automatically eliminated the excess of PETG as a material that will paste or set up system components. However, that statement has been limited by creating a system housing body wall from a cylindrical acrylic material. Two things that need to be discussed are the selection of the wall material and the shape of the cylinder. As defined, acrylic is a transparent plastic material with outstanding strength, stiffness, and exceptional optical clarity. The strength and stiffness required is to overcome the hygroscopic deficiencies of PETG that have been mentioned. scientifically and technically, acrylic will not cause curvature, bulging or loss of clarity with prolonged exposure to moisture or total immersion, as was also used in World War II as a seabed periscope. Thus, it has been proven that there is absolutely no entry of water or air through the acrylic wall with His permission. Furthermore, as is generally known that most marine life is cylindrical in shape if viewed roughly. No less so for submarines and other diving equipment that also have a cylindrical shape in general. The same has also been exemplified and practiced into the design of this study system because high seawater depth has implied hydratic-static pressure on the object and the seawater pressure encountered becomes constant from all directions even from the bottom. Thus, the clear purpose of the design of the cylinder shape is to distribute the water load uniformly to enclose the situation of deep-sea water as stated.

In the meantime, the O-Ring is known as a circular cross section designed to be installed in a groove and compressed during installation between two or more parts thus sealing between the two faces. cylinder. The O-Ring used in this context is made of silicone material due to its high resistance to high temperatures, high resistance to hot air and UV radiation, elastic, finer surface as a sealer than rubber material, as well as good resistance to corrosion. Referring to Figure 4 (b), it is the bottom and legs of the system housing. Since the salinity sensor probe rope is involved in this part where the probe needle needs to touch the water area to get a reading, then a water ingress barrier is required which is referred to as a cavity. The cavity used is from epoxy resin material due to its waterproof nature to chemicals, high sealing, its resistance to low temperature environment, as well as good electrical reliability. In addition, for tidiness and safety factors, the sensor probe strap is pinned to the foot of the figure.

Experiment Analysis

The calibration of each sensor has produced the expected data. which is used to provide correction of the measured data as well as perform uncertainty calculations on the sensor. Therefore, the sensors work accurately and free from any faults hence is enable for a good process control. The sensors that have been clarified are as follows:

1. MS5803
2. TDS SKU: SEN0244
3. TEMENT6000
4. Blox Neo 6M

The level of depth under water is in line with the increase in pressure. Referring to the method of the calibration, relationship between the increasing pressure readings by the MS5803 sensor and the number of books placed on the balloon containing the sensor, has shown a linear feature. Generally, the weight of an object is a force caused by gravity and it can be replaced in the pressure equation. Thus, like the algorithm below, the pressure (P) caused by the weight (W) of an object is also the weight divided by the area (A) over which the weight is applied.

$$P = W/A \quad (1)$$

According to the National Oceanic and Atmospheric Administration (NOAA), at sea level, each square inch of surface will be subjected to a force of 14.6 pounds while the pressure will increase around one atmosphere (atm) for every 10

meters of water depth. Therefore, scientifically, at a depth of 50 meters of dive system of this study, the pressure reading by the sensor starting at sea surface will increase by 5 atm (5066.25 mbar). In addition, for the MS5803 sensor, the pressure reading limit that can be taken is 1400 mbar compared to the pressure sensor used previously which is only 1100 mbar. Basically, the sensor is not only capable of reading pressure parameters but also depth and temperature. However, the calibration of the depth function of the sensor could not be carried out due to the unfavorable pandemic conditions. Even so, an initial inference can be made for such depths that the higher the water depth, the higher the sea level reading read by the sensor. Thus, it has been concluded that these sensors can operate well under the ocean as far as the targeted dive.

The temperature function by MS5803 has been utilized. There is difference in temperature readings given by the sensor as well as from the physical sensor measuring room temperature. With reference to the purpose or existence of this data logger system under water, the temperature measured should be the water temperature. However, due to the lack of cavity material that needs to be placed on the sensor, the calibration of this data is based on room temperature only. The cavity material mentioned is due to the condition of the sensor, which is not waterproof, therefore the sensor board needs to be covered with epoxy or nail polish. Furthermore, the temperature difference

between the two sensors as in Figure is approximately 1.66 °C.

The salinity of seawater that can be measured by TDS SKU: SEN0244 which has been calibrated. Starting with the absence of salt (Figure 5), the value of TDS was observed which is approximately 0 ppm (parts per million). The readings taken were in line with the increase in salt content so that at 45 ml of salt, the TDS value was 1236 ppm. Similarly, the TDS value at 50 ml remained at 1236 ppm. Both conditions are because the sensor capability is a maximum of 1200 ppm only as in the data sheet. Thus, it can be concluded that no matter how much the salinity content of the water, the TDS value is static at approximately 1200 ppm.

The average salinity of seawater as stated by NOAA, it is around 35 parts per thousand or parts per thousand (ppt) which is 3.5% by weight of seawater derived from dissolved salt. Meanwhile, for the target waters of this study system which is a tropical ocean in the Indian Ocean has a total area of 68,556 million km² and the surface salinity of the waters ranged between 32 to 37 ppt. As a rule, it is necessary to know that the water surface of an ocean has stretched as deep as 100 meters below. Theoretically, for the calibrated 1200 ppm saltwater salinity limit, it shows a reading of 1.2 ppt sea salinity which is 3.5% of the median average salinity of the Indian Ocean. Therefore, it can be concluded that as far as a depth as high as 100 meters, this study system is capable of reading water salinity as high as 3.5% only.

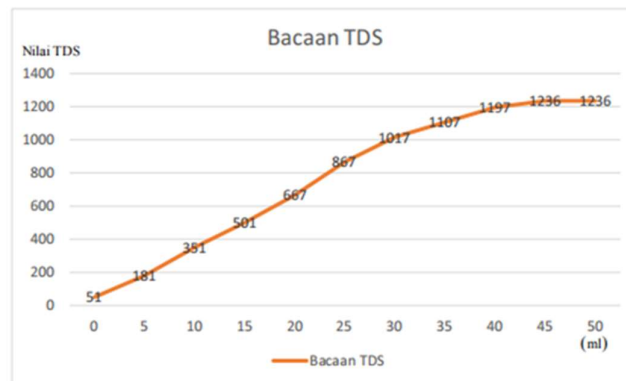


FIGURE 5. Salinity Calibration Data
TDS SKU: SEN 0244

The ambient light focused on this data logger system is that generated by sunlight and does not include artificial light from a strobe or user video light underwater. Thus, the value level of the parameter is measured by TEMT6000. Looking at

Figure 6, the ambient value given by the sensor is in line with the LUX application sensor. Only when the distance between the light source and the two sensors is 22 cm, the ambient value by the application sensor is 120 lux while for the system

sensor is lower which is 100 lux. Thus, an initial conclusion can be made that the higher the distance between the light source and the sensor, the lower

the value of ambient light intensity will be measured.

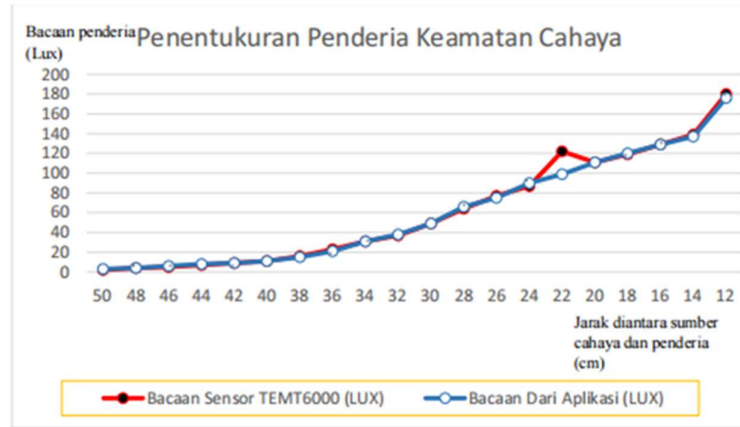


FIGURE 6. Ambient Light Calibration Data TEMT 6000

Determining the location of the system before entering the water is by using U-Blox Neo 6M. Therefore, it does not need to work when in the water, so the calibration carried out is like the figure below where the latitude and longitude values of the selected location are proportional to the location on Google Map.

RESULTS AND DISCUSSION

Constructed Bluetooth Communication

Among the Bluetooth components as mentioned in the study methods chapter, the HM-10 was selected to function in this study system. This is because of its specifications that meet the required characteristics such as sleep mode function, low current consumption, and low energy consumption. The sleep mode function is required when the user chooses to record data instead of reading data on the microSD card. Therefore, if the user chooses to read the data on the microSD, the sleep mode will be disabled and then, the reading of the data occurs by communicating with the computer via Bluetooth communication. As illustrated in Figure 7, the data read is in the form of .txt which can also be included in Microsoft Excel as .csv. The read data is then automatically stored in the computer via the PuTTY terminal.

3D Printed Mechanical Design

Figure 8 shows the 3D printed of the whole system enclosure to go for at most 50 meter in the water. The assembly of the electronic components in Figure 3 with Figure 8 has not able to be accomplished. This is due to the complex situation of current pandemic of Covid-19. The remaining observation to be made is the performance of the expected system to stand in the high pressure for at most 5066.25 mbar in the 50 meter in the sea water.



FIGURE 8. 3D printed system enclosure

20210111_160033 - Notepad

File Edit Format View Help

Putty log 2021.01.11 16:00:33

y 04.01.2021 -- 11:24:48	26.9 °C	6 ppm	10 lux
Monday 04.01.2021 -- 11:24:49	26.9 °C	6 ppm	11 lux
Monday 04.01.2021 -- 11:24:50	26.9 °C	6 ppm	8 lux
Monday 04.01.2021 -- 11:24:51	26.9 °C	6 ppm	10 lux
Monday 04.01.2021 -- 11:24:52	26.9 °C	6 ppm	10 lux
Monday 04.01.2021 -- 11:24:54	26.9 °C	6 ppm	11 lux
Monday 04.01.2021 -- 11:24:55	26.9 °C	6 ppm	8 lux
Monday 04.01.2021 -- 11:24:56	26.9 °C	6 ppm	12 lux
Monday 04.01.2021 -- 11:24:57	26.9 °C	6 ppm	11 lux
Monday 04.01.2021 -- 11:24:58	26.9 °C	6 ppm	8 lux
Monday 04.01.2021 -- 11:24:59	26.9 °C	6 ppm	10 lux
Monday 04.01.2021 -- 11:25:00	26.9 °C	6 ppm	11 lux
Monday 04.01.2021 -- 11:25:01	26.9 °C	6 ppm	11 lux
Monday 04.01.2021 -- 11:25:02	26.9 °C	6 ppm	10 lux
Monday 04.01.2021 -- 11:25:03	26.9 °C	4 ppm	11 lux
Monday 04.01.2021 -- 11:25:04	26.9 °C	4 ppm	11 lux
Monday 04.01.2021 -- 11:25:05	26.9 °C	4 ppm	10 lux
Monday 04.01.2021 -- 11:25:06	26.9 °C	4 ppm	10 lux
Monday 04.01.2021 -- 12:01:27	26.9 °C	0 ppm	16 lux
Monday 04.01.2021 -- 12:01:28	26.6 °C	0 ppm	15 lux
Monday 04.01.2021 -- 12:01:29	26.9 °C	0 ppm	8 lux
Monday 04.01.2021 -- 12:01:30	26.9 °C	0 ppm	8 lux
Monday 04.01.2021 -- 12:01:31	26.6 °C	0 ppm	17 lux
Monday 04.01.2021 -- 12:01:32	26.9 °C	0 ppm	8 lux
Monday 04.01.2021 -- 12:01:34	26.9 °C	0 ppm	16 lux
Monday 04.01.2021 -- 12:01:35	26.9 °C	0 ppm	16 lux
Monday 04.01.2021 -- 12:01:36	26.9 °C	0 ppm	8 lux
Monday 04.01.2021 -- 12:01:37	26.9 °C	0 ppm	16 lux
Monday 04.01.2021 -- 12:01:38	26.9 °C	0 ppm	16 lux
Monday 04.01.2021 -- 12:01:39	26.9 °C	0 ppm	8 lux
Monday 04.01.2021 -- 12:01:40	26.9 °C	0 ppm	16 lux
Monday 04.01.2021 -- 12:01:41	26.9 °C	0 ppm	8 lux
Monday 04.01.2021 -- 12:01:42	26.9 °C	0 ppm	8 lux
Monday 04.01.2021 -- 12:01:43	27.0 °C	0 ppm	16 lux
Monday 04.01.2021 -- 12:01:44	26.9 °C	0 ppm	8 lux

FIGURE 7. Stored .txt file in microSD card

Figure 9 gives a clear picture of the overall flow chart of the system. Starting with the user interface, there are two main options that will be selected via a rotary encoder button that then leads to the process of recording or reading data. When the recording process is selected, the RTC or real - time clock starts while the Bluetooth module enters sleep mode. After that, all the sensors involved start reading the parameters in the waters, the readings are recorded and stored in a file that has been set on the microSD card that has been opened. Each entry made in the selected time interval on the file, the file will be closed and then repeat the process of opening the file until the time has been reached then the process ends.

Further, when the process of reading the data selected by the user, a Bluetooth module is developed and waits for connection with a computer. After the connection, the Bluetooth module reads the data file in the microSD card that has been opened and then displays the reading on the computer through a terminal called PuTTY. Then, the completed reading display is then automatically saved into a computer file in .txt format.

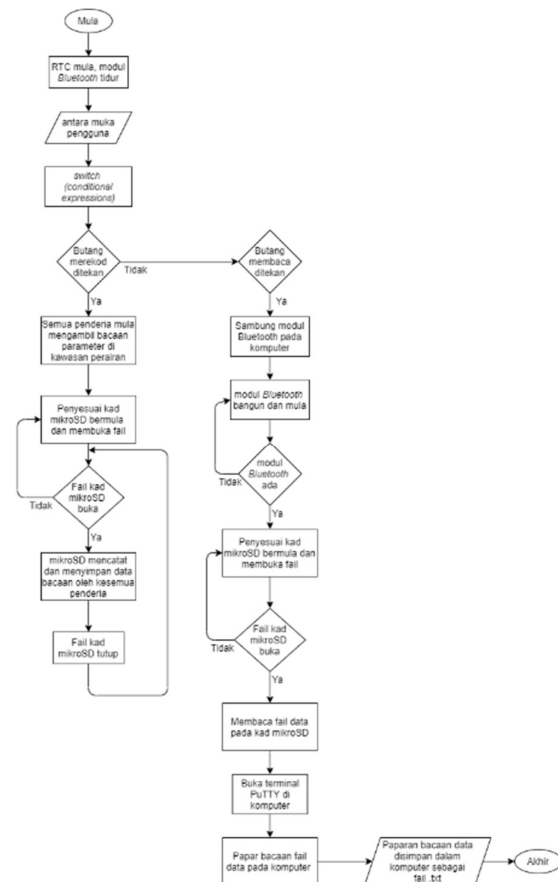


FIGURE 9. System Programming

CONCLUSION

There are elements that give ideas for further improvement for example on the components' limitations of the system with the user interface. Hence, the thing to be emphasized in this context is based on two main things, namely from the point of view of physical and system software.

As for its physical point of view, further comment could not be well identified due to the test not being conducted but based on the initial hypothesis, it is suggested that. Whereas, in terms of software, it refers to the physical capabilities mentioned by which the system needs to interact with the user about the data collected at anytime and anywhere. The main areas of the proposed improvement to this underwater data logging system are real - time monitoring during data logging as well as the alternative use of salinity sensors.

ACKNOWLEDGEMENT

The authors would like to thank Universiti Kebangsaan Malaysia for their financial support under the grant GUP-2017-094.

REFERENCES

- Abdullah, M. H., S. A. Che Ghani, Zaulkafilai, Z. & Tajuddin, S. N. 2017. Development open-source microcontroller-based temperature data logger. *Materials Science and Engineering*
- Alabdullah, A. J., Farhat, B. I. & Chtourou, S. 2019. Air Quality Arduino Based Monitoring System. *Saudi Arabia: 2nd International Conference on Computer Applications & Information Security (ICCAIS)*
- AMFG. 2019. A Guide to 3D Printing with Titanium
- Breddermann, K., Drescher, P., Polzin, C., Seitz & H., Paschen, M. 2016. Printed pressure housings for underwater applications. *Ocean Engineering*. Volume 113. Pages 57-63
- Brittani Callan. 2019. Open-Source Underwater Instrument design aids Northwestern's professor exploration of underwater world
- Champion, B. T., Jamshidi, M. & Joordens, M. A. 2016. 3D printed underwater housing. *Rio Grande: World Automation Congress (WAC)*,
- Hironori Kondo. 2021. PETG vs ABS: The Differences – Simply Explained
- Jan Schulz. 2008. Conversion Between Conductivity and PSS-78 Salinity NOAA
- Katie Lange. 2019. Hitting Bottom Submariner Explored Deepest Part of Ocean
- Kiran Patil, Mr., Sachin Patil, Mr., Sanjay Patil, Mr., Vikas Patil, Mr. 2018. Monitoring of Turbidity, PH & Temperature of Water Based on GSM. *International Journal for Research in Emerging Science and Technology*. Volume 2
- Lee, H. L., Tanggang F., Hamid, M. R., Benson, Y. & Razali, M. R. 2016. Modelling the Influence of River Flow and Salt Water Intrusion in the Terengganu Estuary, Malaysia. *Malaysia: Soft Soil Engineering International Conference 2015*
- Mahzan, N.N., Omar, A. M., Rimon, L., Mohammad Noor, S. Z. & Rosselan, M. Z. 2017. Design and Development of an Arduino Based Data Logger for Photovoltaic Monitoring System
- Memoon Sajid, Jahan Zeb Gul, Kim, S. W., Kim, H. B., Na, K. H. & Choi, K. H. 2018. Development of 3D-Printed Embedded Temperature Sensor for Both Terrestrial and Aquatic Environmental Monitoring Robots. *3D Printing and Additive Manufacturing*. Vol. 5, No. 2
- Meryl Kremer. 2019. What's in the Water 7 Common Characteristics that Water Quality Instruments Measure
- NOAA. 2020. Why is the ocean salty?
- Rakusilmu. 2018. Pengertian Data Logger Beserta Kegunaan, dan Cara Penggunaan
- Sathiabama, T., Thirugana, Abu Bakar Jaafar, Takeshi Yasunaga, Tsutomu Nakaoka, Yasuyuki Ikegami, Suriyanti Su. 2021. Estimation of Ocean Thermal Energy Conversion Resources in the East of Malaysia
- Sofiane Guessasma, Sofiane Belhabib, Hedi Nouri. 2019. Printability and Tensile Performance of 3D Printed Polyethylene Terephthalate Glycol Using Fused Deposition Modelling
- Suffian, Md., I., Nurhaliza, R., Noor Hazwani & M. A. 2017. Empirical Ocean Colour Algorithms for Estimating Sea Surface Salinity in Coastal Water of Terengganu. *Pertanika J. Sci. & Technol*
- Suryono, S., Widowati, W., Putro, S. P. & Sunarno, S. 2018. A Capacitive Model of Water Salinity Wireless Sensor System Based on WIFI-Microcontroller. *Bandung: 6th International Conference on Information and Communication Technology (ICoICT)*
- Thuras, A. L. . 1918. An instrument for recording sea-water salinity. *Journal of the*

Washington Academy of Sciences. Vol. 8,
No. 21. pp. 676-687. Washington:

Washington Academy of Sciences

Design Optimization of Fuzzy-PID Controller for Autonomous Hovercraft Path Tracking

(Rekabentuk Optimasi Pengawal Fuzzy-PID untuk Penjejakan Laluan Hoverkraf Berautonomi)

Nur Amaliea Izzatie Azmi, Asma Abu-Samah, Aqilah Baseri Huddin

Department of Electrical, Electronic and Systems Engineering, Faculty of Engineering and Built Environment, Universiti
Kebangsaan Malaysia, Malaysia

*Corresponding author: amalieaazmi@gmail.com

ABSTRACT

Hovercraft is a very active and agile vehicle where it needs an optimum and stable control. Autonomous hovercraft control based on Advanced Process Control is not widely introduced. In this paper, a design of fuzzy-PID control will be introduced. Fuzzy-PID control combines PID controller and fuzzy controller which has two inputs and three outputs. The fuzzy controller will tune the PID controller parameters when the system response shows error and error rate. The autonomous hovercraft model is described and implemented using the Euler Lagrange approach. Fuzzy-PID based controller and conventional PID controller are compared by simulation. The path tracking of autonomous hovercraft was tested using MATLAB Simulink software. Path tracking is important for achieving a global stabilization and exponential convergence of a tracking error with desired trajectory. In this paper, simulation results show the trajectory position of autonomous hovercraft in both surge and sway position and also path tracking in a circle. The simulation results show that fuzzy-PID controller has a better performance compared to the classical PID controller. This concludes that the proposed controller shows the effectiveness and good resilience where it has advantages of rapid respond, high stability and tracking accuracy and also good in anti-interference. The fuzzy-PID controller is proven to be an appropriate choice for path tracking control of an autonomous hovercraft.

Keywords: Path tracking; Hovercraft; Trajectory tracking; Fuzzy PID Control; Simulation in Simulink

ABSTRAK

Hoverkraf merupakan kenderaan yang sangat aktif dan tangkas dimana ia memerlukan kawalan yang optimum dan stabil. Kawalan hoverkraf berautonomi berasaskan kawalan proses termaju tidak banyak diperkenalkan. Di dalam kertas kajian ini, rekabentuk kawalan fuzzy-PID untuk penjejakan laluan sebuah hoverkraf berautonomi akan diperkenalkan. Penjejakan laluan adalah penting untuk memperoleh kestabilan global dan penumpuan eksponensial posisi ralat penjejakan dengan landar ruang diingini. Pengawal fuzzy-PID adalah gabungan pengawal PID dan pengawal fuzzy yang mempunyai dua masukan dan tiga keluaran. Pengawal fuzzy akan menala parameter pengawal PID apabila respons sistem menunjukkan ralat dan kadar ralat. Model hoverkraf berautonomi berdasarkan pendekatan Euler Lagrange diperkenalkan dan digunakan. Kawalan berdasarkan fuzzy-PID dan konvensional PID dibandingkan melalui simulasi. Penjejakan laluan hoverkraf berautonomi ini diuji menggunakan perisian MATLAB/Simulink. Di dalam kertas ini, simulasi menunjukkan hasil posisi landar ruang hoverkraf dalam keadaan pusuan dan huyung serta penjejakan laluan dalam bentuk bulatan. Hasil simulasi menunjukkan pengawal fuzzy-PID memberikan prestasi yang lebih baik berbanding pengawal konvensional PID dimana dapat membuktikan model kawalan sasaran ini memberikan keberkesanan dan ketahanan yang baik. Ia mempunyai kelebihan tindak balas dngan pantas, kestabilan yang tinggi, ketepatan pengesanan dan menghapuskan gangguan dengan baik. Jadi, pengawal fuzzy-PID ternyata sesuai untuk penjejakan laluan untuk hoverkraf berautonomi.

Kata Kunci: Penjejakan laluan; Hoverkraf; Penjejakan landar ruang; Pengawal Fuzzy-PID; Simulasi di Simulink

INTRODUCTION

Hovercraft is a hybrid vehicle that can operate in various kinds of surface such as land, water, mud, and many more. Nowadays, hovercraft has become a vehicle with numerous functions. According to (Liu et al. 2016) and (Fu et al. 2018), hovercraft is used for water pollution monitoring, coast guard, and military operations. With the rapidly evolving technology, hovercrafts become more complex with the inclusion of electronics components, sensors, drivers, controller design. The example of 3D model of an autonomous hovercraft is as shown in Figure 1. However, the most crucial criteria in developing and designing an autonomous robot especially hovercraft is the control. This is because the ability and optimization of an autonomous robot depends on its controller. The most important concern of this hovercraft control is its stability and tracking control.



FIGURE 1. 3D model of an autonomous hovercraft

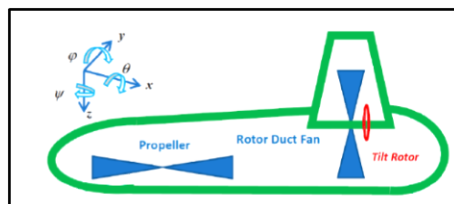


FIGURE 2. Configuration model of hovercraft

According to (Tran, Son, et al. 2020) and (Hussein 2013), there are three types of rotors in a hovercraft as shown in Figure 2. The first is an inclined servo motor, a rotor duct fan mounted on the y-axis and a propeller mounted on the z-axis of the vehicle. From (Lu et al. 2019) and (Fu, Wang, et al. 2017), path control is important and practical issue in autonomous robots and divided into two categories which are trajectory tracking and path tracking control. In trajectory tracking control, a graph based on a time relationship is used to achieve the desired trajectory of an autonomous hovercraft. Meanwhile, path tracking control, the desired trajectory of a hovercraft is based on the geometrical parameters that are easily achieved.

Trajectory tracking control is important for hovercraft to arrive at a certain location at a certain time while path tracking control is needed for hovercraft to trace or track the desired trail given by geometrical parameters at a certain speed.

PID control is a conventional control that is often used especially on autonomous robot controls. According to (Guney & Demir 2017), tracking control and stability can be achieved by using PID control. Typically, PID-based autonomous robots use the steering drive angle error as input and the steering angle of the robot as the output. Although PID control can achieve stability and control tracking, the accuracy of the system is still poor. Therefore, fuzzy logic control is introduced to achieve optimal control as fuzzy control capability can control objects with complex mathematical models and nonlinear. However, fuzzy control also has some shortcomings where it is challenging to eliminate steady-state error low steady control accuracy and not smooth enough. Therefore, the basic fuzzy control will be combined with the conventional PID control to overcome each other's shortcomings and ultimately provides more optimal control that meets the specified requirements.

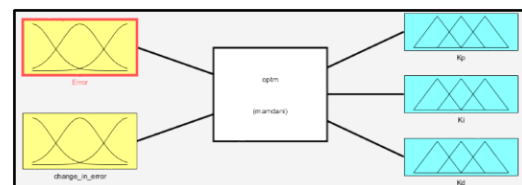


FIGURE 3. Fuzzy control structure

In this paper, a fuzzy-PID control design for hovercraft path tracking will be proposed. According to (Tiep et al. 2018), the fuzzy-PID control that is based on fuzzy controller and PID controller will have two inputs and three outputs as illustrated in Figure 3. According to (Chen et al. 2018) and (Phu & Choi 2019), the fuzzy controller will tune the PID controller parameters, K_d , K_i and K_p when error and error rate exists. The kinematic and dynamic equations of the autonomous hovercraft is described using the Euler Lagrange approach. Expected results will show how the proposed controller can facilitate tuning for PID control, improve the path tracking control and compare PID and fuzzy-PID control optimization. The results expect the fuzzy-PID controller to have better performance than the conventional PID controller as it has advantages of fast response, high stability and tracking accuracy which makes the fuzzy-PID control suitable for route tracking control of a hovercraft.

METHODOLOGY

Experiment Design and Procedure

The research process is illustrated as the flowchart shown in Figure 4. The process of conducting the problem statement, literature review, identifying the hovercraft equations is made earlier before proceeding with the simulation process.

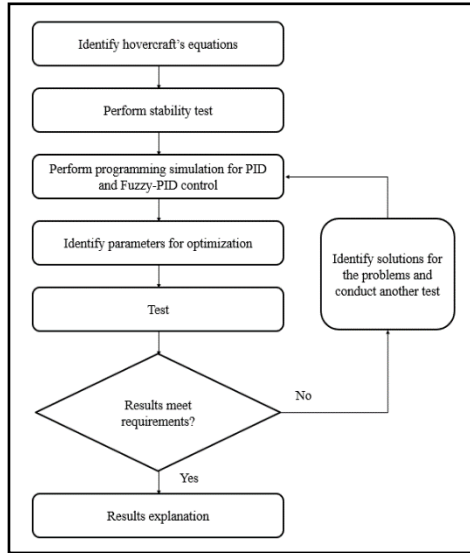


FIGURE 4. Project flowchart

The block diagram for the overall autonomous hovercraft tracking control is as shown in Figure 5, where there is reference tracking, PID and fuzzy-PID controllers, and a hovercraft model. The path tracking reference provides the desired route for the hovercraft to track. Paths can consist of straight lines, circles, and ellipses.

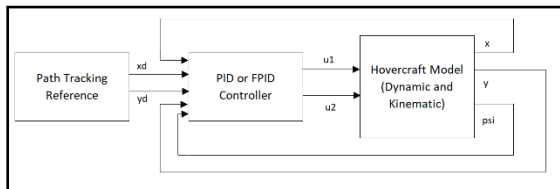


FIGURE 5. Block diagram

This path tracking reference produces parameters x_d and y_d which are the desired surge and sway positions respectively. This reference position will be the input to the PID or fuzzy-PID controller to be processed. The process carried out in calculating the desired value of velocity and

angular velocity which in turn becomes the input to the hovercraft model. Hovercraft models constructed from dynamic and kinematic equations as well as interference are introduced. In this block, the velocity values and the reference angle velocity will be used to produce the hovercraft's oscillation, sway and angle positions and these values form the basis for the hovercraft to move. The hovercraft's actual surge, sway and angle positions will be fed back to the control block to reduce errors.

Hovercraft Model and Parameters

The small -scale autonomous hovercraft in this study paper was published using the Euler Lagrange method according to (Fu, Gao, et al. 2017), and (Tran, Lam, et al. 2020). Based on Figure 6, the equation of motion of hovercraft can be expressed as Equation 1 to Equation 3 which is also the hovercraft's kinematic equations.

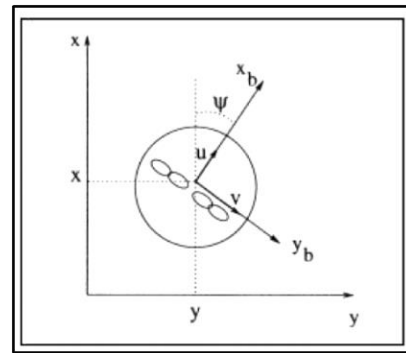


FIGURE 6. Hovercraft model

$$\dot{x} = u \cos \psi - v \sin \psi \quad (1)$$

$$\dot{y} = v \cos \psi + u \sin \psi \quad (2)$$

$$\dot{\psi} = r \quad (3)$$

Where u is the surge velocities, v is the sway velocities and r is the yaw angle velocities. The dynamical model of the hovercraft can be simplified using Equation 4 until Equation 6.

$$\dot{u} = vr + \frac{\tau_u}{m} \quad (4)$$

$$\dot{v} = -ur \quad (5)$$

$$\dot{r} = \tau_r \quad (6)$$

Where m is the mass, τ_u is the torque in surge and τ_r is the torque in sway. For this hovercraft, the parameters to be used for the equation are as shown in Table 1.

TABLE 1 Hovercraft's Parameters

Parameters	Symbol	Value
Mass	M	2.1kg
Angle	$\Psi(t)$	30°
Moment of Inertia	I	0.000257kgm ²

Control System Design

For the tracking model, the input to this system is a real-time moving point where the hovercraft can follow the track by following this point. This tracking target is set to a circle with a size specified to a radius of value one. The approach used to construct the circle model for this path tracking is the circle parametric equation whose basis is as in Equation 5

$$x = r \cos t \quad (7)$$

$$y = r \sin t \quad (8)$$

Based on Figure 7, there are two gains on the tracking model. By changing their values, the shape of the tracking will change such as ellipses and circles can be set. In a tracking target, the hovercraft will keep a distance with a moving point to be set at 0.01 inches on the system.

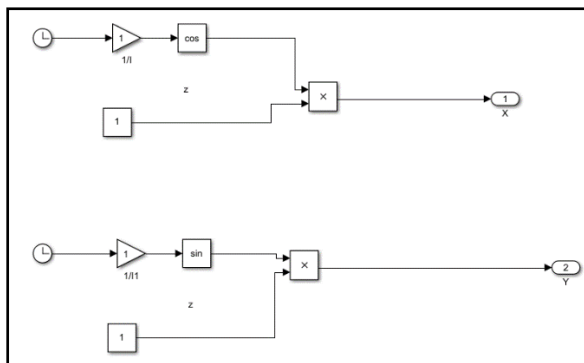


FIGURE 7. Simulink model of path tracking

For fuzzy control, Mamdani fuzzy type will be used where there are two inputs namely error (e) and change in error (ce). This fuzzy controller will tune the parameters on the PID controller namely Kp, Ki and Kd. The self-tuning of the PID controller will find fuzzy relationships with all three components of the PID controller. For the fuzzy-PID control, to determine the error variable and the error change, five fuzzy membership function inputs were used namely negative big (NB), negative small (NS), zero (Z), positive small (PS) and positive big (PB). The output for this

controller is selected from four values, namely very big (VB), large (B), medium (M) and small (S).

During the operation of the control system, if it continuously detects errors and error rates, tuning the PID parameters in real-time by following the rules of the fuzzy controller, will make the system achieve good dynamic and azimuth performance. By using a PID controller, the velocity and angular velocity of the hovercraft can be controlled. There are some fuzzy rules for determining error variables and error changes and these can be scheduled as per Table .2. In this paper, the membership function format used is if the error is negative big (NB), and the error rate is also negative big (NB), so Kp is very big (VB), Ki is small (S) and Kd is also small (S).

Simulations for the PID controller and the fuzzy-PID controller were performed separately due to the different controller models. According to (Somwanshi et al. 2019), the basics for both controllers are more or less the same. For the PID controller, the hovercraft's position and angle deviation which is the feedback from the hovercraft model becomes the input of this controller. The output of the PID controller will control the velocity and angular velocity of the hovercraft. Whereas, for fuzzy-PID based control systems, a fuzzy controller is added in front of the PID controller. The inputs to this fuzzy controller are position, azimuth error and error rate while the output of this controller results from of the parameter values Kp, Ki and also Kd on real -time tuning. Once the parameters are tuned, the PID controller will begin to control the velocity and angular velocity of the hovercraft.

The hovercraft model is constructed based on the published hovercraft dynamic and kinematic equations. The kinematics equations are as Equation 1 until Equation 3 whereas the dynamic equations are as Equation 4 until Equation 6.

All these equations are combined in the form of blocks to obtain a simulation model in MATLAB Simulink software. Interference such as inertia and friction based on (Cabecinhas et al. 2018) are also included to make the hovercraft model more realistic. The position and angle deviation of the hovercraft will be fed back to the input of the PID or fuzzy-PID controller and the output of this controller will control the velocity and angular velocity of the hovercraft. The hovercraft model built on MATLAB Simulink is as shown in Figure 8

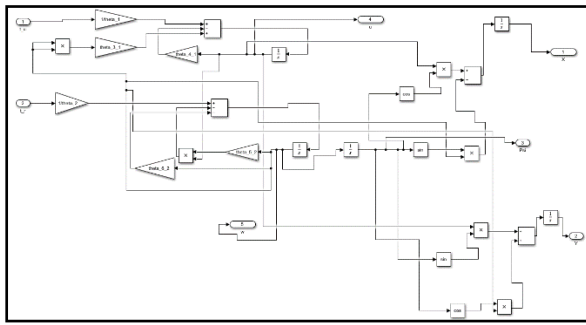


FIGURE 8. Simulink model of an autonomous hovercraft

For the tracking error curve, according to (Xu et al. 2014) Equation 6 which is the speed diversion is used.

$$e = \sqrt{(\dot{x} - \dot{x}')^2 + (\dot{y} - \dot{y}')^2} - d \quad (9)$$

Where \dot{x}' and \dot{y}' are the coordinates of the moving point in the tracking. The diversion i.e. the hovercraft azimuth error is as in Equation 7

$$\dot{\theta} = \tan^{-1} \frac{\dot{y} - \dot{y}'}{\dot{x} - \dot{x}'} \quad (10)$$

TABLE 2. Fuzzy Rule Table for Kp/Ki/Kd gain

e/ce	NB	NM	Z	PS	PB
NB	VB/S/S	VB/M/S	S/M/VB	S/M/B	M/S/S
NS	VB/B/S	B/B/S	S/B/B	S/B/B	B/S/S
Z	B/B/S	M/B/M	S/VB/B	S/VB/M	VB/VB/S
PS	M/B/M	S/B/B	S/B/B	M/B/S	VB/B/S
PB	S/S/M	S/S/VB	S/M/VB	B/M/S	VB/S/S

RESULTS AND DISCUSSION

Controllability Test

Controllability tests should be performed to test whether the system equations can be controlled or not. If the output is $unco = 0$, the system equation can be controlled. The results of the controllability test are shown in Figure 9.

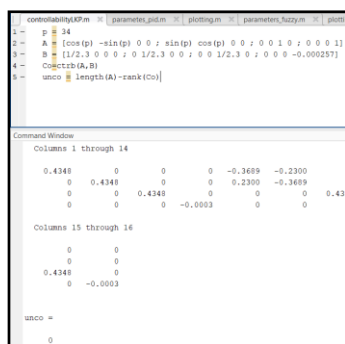


FIGURE 9. Controllability test result

After being tested, the equation of this hovercraft system proved to be controllable because it managed to obtain the result of $unco = 0$

Trajectory Tracking of Surge Position

The position of the surge is the longitudinal axis. Waves that interfere with the hovercraft either from

the front or back force the hovercraft to leap momentarily forward or backward. The position of this surge can be tested and observed with position and time curves. The reference position is shown for easy comparison with the actual position of the hovercraft. The surge position tracking results for both PID and fuzzy-PID controllers are shown in Figure 10 and Figure 11.

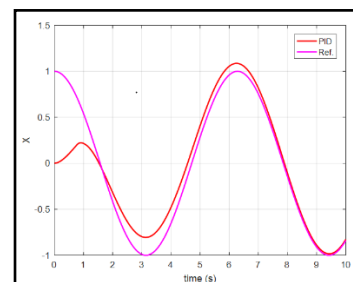


FIGURE 10. Trajectory tracking of surge position using PID controller

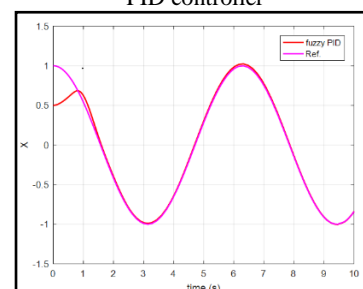


FIGURE 11. Trajectory tracking of surge position using FPID controller

Figure 10 shows the results of the hovercraft surge position when PID control is applied while Figure 11 shows the results of the hovercraft surge position when fuzzy-PID control is applied. A hovercraft with a PID controller takes 8 seconds to approach the full reference position while a hovercraft with a fuzzy-PID controller takes 1.5 seconds. This means, the response time taken by a hovercraft with a fuzzy-PID controller to achieve reference position accuracy is lower compared to a PID controller. The overshoot percentage on PID controllers is also higher compared to fuzzy-PID controllers. This gives the error between the actual hovercraft surge position and the reference surge position for a hovercraft is larger with a PID controller than a hovercraft with a fuzzy-PID controller.

Trajectory Tracking for Sway Position

The disturbance produces a motion that staggers the hovercraft and causes the hovercraft to tend to move to the left and right sides. The position of the sway is the transverse axis. This sway position can be tested and observed with position and time curves. The reference position is shown for easy comparison with the actual position of the hovercraft. The sway position tracking results for both the PID and fuzzy-PID controllers are shown in Figure 12 and Figure 13.

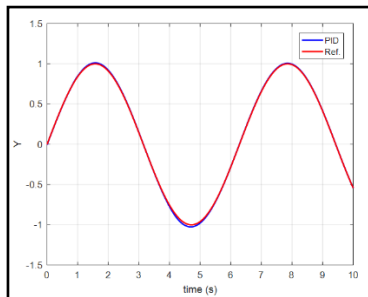


FIGURE 12. Trajectory tracking of sway position using PID controller

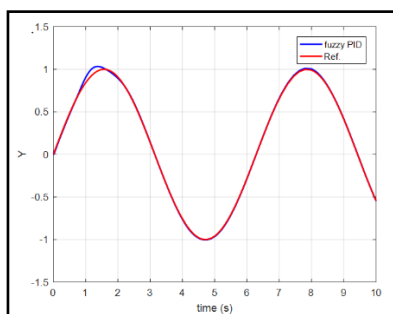


FIGURE 13. Trajectory tracking of sway position using FPID controller

Figure 12 shows the results of the hovercraft in sway position when PID control is applied while Figure 13 shows the results of the hovercraft surge position when fuzzy-PID control is applied. A hovercraft with a PID controller takes 5 seconds to approach the full reference position while a hovercraft with a fuzzy-PID controller takes 2 seconds. This means, the response time taken by a hovercraft with a fuzzy-PID controller to achieve reference position accuracy is lower compared to a PID controller. The overshoot percentage for the sway position for both controllers was lower compared to the surge position. The error between the actual sway position of the hovercraft and the reference sway position of the two controllers is low and only the response times of these two systems show a significant difference

Path Tracking

For path tracking control, the desired trajectory is based on easily accessible geometric parameters. In the simulation of this study, a circle of radius 1 was defined as trajectory tracking. The starting state of the hovercraft is set to the coordination of (0,0) with a directional angle of 0°. The hovercraft tracking performance for both controllers was observed and the simulation results are as shown in Figure 14 and Figure 15.

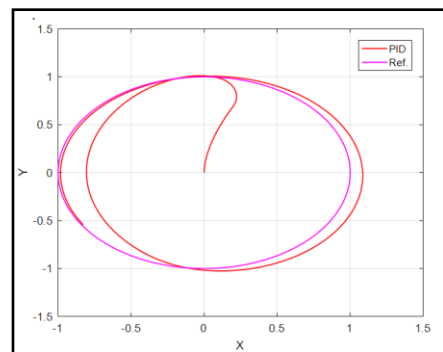


FIGURE 14. Path tracking using PID controller

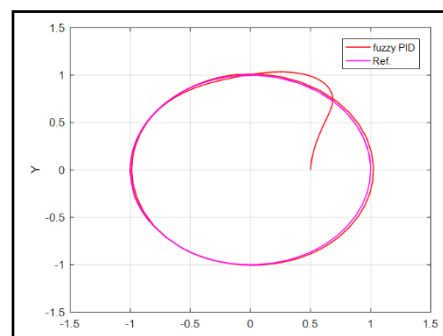


FIGURE 15. Path tracking using FPID controller

The purple-lined reference path tracking is shown to facilitate comparison with the red-lined hovercraft's actual route tracking. Based on the simulation results, the controller system can track the full direction faster after adding fuzzy control function to the system. In addition to tracking directions faster, controller systems using fuzzy-PID also show lower tracking errors than PID controllers. The high response time to track the route gives a poor performance on the hovercraft. The hovercraft route tracking simulation using the target control model can also show this control tracks the desired route satisfactorily because the actual tracking almost matches the reference tracking.

Tracking Error Curve

For this tracking error curve, the horizontal axis is set for the time in seconds and the vertical axis is set for the error value. The tracking error curves of the two controller systems starting from the starting state have been combined in one figure shown in Figure 16.

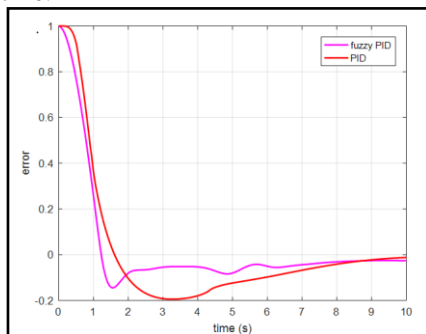


FIGURE 16. Tracking error curve

Based on the results, the controller system can track the path completely and give a minimum error within 9 seconds after adding fuzzy control function on the system while on the system using PID controller only, the system takes 10 seconds to track the direction completely. In addition to tracking the direction faster, the controller system using fuzzy-PID also shows low overshoot, and steady-state error and high tracking accuracy.

DISCUSSION

By applying a fuzzy controller to tune the PID parameters, the hovercraft system can be improved. System overshoot on path tracking is lower compared to PID controllers. As expected, the target design methodology gives good performance on autonomous hovercrafts to track the desired route well. The actual path almost matches the

reference route. The path tracking error value achieved by the fuzzy-PID controller is smaller than that of the PID controller. Thus, the simulation results show that the autonomous hovercraft with the targeted control model can track the path and trajectory quicker and effectively with low tracking error and high accuracy than conventional PID control. The results indicate that the fuzzy-PID control-based autonomous hovercraft has many advantages in velocity control, system stability and anti-interference performance in route tracking and space.

CONCLUSION

The Design Optimization of fuzzy-PID Controller for Path Tracking of an Autonomous Hovercraft was proposed in this paper. Euler Lagrange approach is used to describe the dynamic and kinematic model of the autonomous hovercraft with external disturbances and common parameters of hovercraft. The proposed control model is fuzzy-PID which is a combination of PID controller and fuzzy controller that aims to improve the performance of classical PID controller for path tracking.

Simulations are conducted using MATLAB Simulink to test the proposed controller's effectiveness to drive the autonomous hovercraft along the desired path. The simulation also compares the performances of PID controller and fuzzy-PID controller. The results show that fuzzy-PID controller is suitable to be implemented in the autonomous hovercraft as it gives a better performance as compared to the classical PID controller. The proposed controller gives satisfactory results on the path tracking as the hovercraft can track the target trajectory more efficiently and faster with small tracking error and good accuracy. The results also conclude that fuzzy-PID controller is suitable to be implemented to an autonomous hovercraft surely has advantages in controlling velocities, improves stability and gives good performance in path tracking.

ACKNOWLEDGEMENT

The authors would like to thank Universiti Kebangsaan Malaysia and Elvira Systems for their support.

REFERENCES

- Cabecinhas, D., Batista, P., Oliveira, P. & Silvestre, C. 2018. Hovercraft Control With Dynamic Parameters Identification. *IEEE Transactions on Control Systems Technology* 26(3): 785–796. doi:10.1109/TCST.2017.2692733
- Chen, B., Liu, X. & Lin, C. 2018. Observer and Adaptive Fuzzy Control Design for

- Nonlinear Strict-Feedback Systems With Unknown Virtual Control Coefficients. *IEEE Transactions on Fuzzy Systems* 26(3): 1732–1743. doi:10.1109/TFUZZ.2017.2750619
- Fu, M., Gao, S. & Wang, C. 2017. Safety-Guaranteed Trajectory Tracking Control for the Underactuated Hovercraft with State and Input Constraints. *Mathematical Problems in Engineering* 2017. doi:10.1155/2017/9452920
- Fu, M., Gao, S., Wang, C. & Li, M. 2018. Human-Centered Automatic Tracking System for Underactuated Hovercraft Based on Adaptive Chattering-Free Full-Order Terminal Sliding Mode Control. *IEEE Access* 6(c): 37883–37892. doi:10.1109/ACCESS.2018.2854752
- Fu, M., Wang, T., Xu, Y. & Gao, S. 2017. Path-following control of an underactuated hovercraft with dynamic uncertainties under Serret-Frenet frame. *Chinese Control Conference, CCC* 3635–3640. doi:10.23919/ChiCC.2017.8027923
- Guney, E. & Demir, M. 2017. A comparative velocity control study of permanent magnet tubular linear DC motor by using PID and fuzzy-PID controllers. *2017 International Conference on Control, Automation and Diagnosis, ICCAD 2017 (Lm)*: 390–395. doi:10.1109/CADIAG.2017.8075690
- Hussein, W. M. 2013. Stabilization and Design of a Hovercraft Intelligent Fuzzy Controller. *International Journal of Engineering Research and Technology* 2(12): 2843–2857.
- Liu, L., Wang, D. & Peng, Z. 2016. ESO-based line-of-sight guidance law for straight line path following with exact sideslip compensation. *Proceedings of the World Congress on Intelligent Control and Automation (WCICA)* 2016-Sept: 677–681. doi:10.1109/WCICA.2016.7578426
- Lu, D., Xie, W., Cabecinhas, D., Cunha, R. & Silvestre, C. 2019. Path Following Controller Design for an Underactuated Hovercraft with External Disturbances. *International Conference on Control, Automation and Systems* 2019-Octob: 76–81. doi:10.23919/ICCAS47443.2019.8971493
- Phu, D. X. & Choi, S. B. 2019. A New adaptive fuzzy PID controller based on riccati-like equation with application to vibration control of vehicle seat suspension. *Applied Sciences (Switzerland)* 9(21): 1–16. doi:10.3390/app9214540
- Somwanshi, D., Bunde, M., Kumar, G. & Parashar, G. 2019. Comparison of fuzzy-PID and PID controller for speed control of DC motor using LabVIEW. *Procedia Computer Science* 152: 252–260. doi:10.1016/j.procs.2019.05.019
- Tiep, D. K., Lee, K., Im, D. Y., Kwak, B. & Ryoo, Y. J. 2018. Design of fuzzy-PID controller for path tracking of mobile robot with differential drive. *International Journal of Fuzzy Logic and Intelligent Systems* 18(3): 220–228. doi:10.5391/IJFIS.2018.18.3.220
- Tran, H. K., Lam, P. D., Trang, T. T., Nguyen, X. T. & Nguyen, H. N. 2020. Fuzzy gain scheduling control apply to an RC Hovercraft. *International Journal of Electrical and Computer Engineering* 10(3): 2434–2440. doi:10.11591/ijece.v10i3.pp2434-2440
- Tran, H. K., Son, H. H., Duc, P. Van, Trang, T. T. & Nguyen, H. N. 2020. Improved genetic algorithm tuning controller design for autonomous hovercraft. *Processes* 8(1). doi:10.3390/pr8010066
- Xu, Q., Kan, J., Chen, S. & Yan, S. 2014. Fuzzy PID Based Trajectory Tracking Control of Mobile Robot and its Simulation in Simulink. *International Journal of Control and Automation* 7(8): 233–244. doi:10.14257/ijca.2014.7.8.20

Index of Authors

Nur Aqilah Baseri Huddin, 82

Asma Abu-Samah, 82

Badariah Bais, 57

Charis Teoh Yi En, 1

Chia Tieng Tieng, 13

Gan Kok Beng, 1

Harhiviin a/l Ganesan, 20

Huda Abdullah, 28

Iskandar Yahya, 72

Izzuan Ismail, 40

Kalaivani Chellapan, 20

Kaliswaran a/l Ganesan, 28

Mohammad Shahidul Islam, 63

Mohammad Tariqul Islam, 63

Muhammad Khairul Naim Saaey, 47

Nik Khaliq Zailani Nik Iskandar, 57

Noorfazila Kamal, 28

Norbahiah Misran, 63

Nor Azwan Mohamed Kamari, 40

Nur Amaliea Izzatie Azmi, 82

Nurrol Athirah Mohamad, 63

Nurul Izzati Saleh, 72

Puvaneswaran a/l Chelvanathan, 57

Radin Za'im Radin Umar, 47

Sawal Hamid Md Ali, 13

Yushaizad Yusof, 47